Ion-nanostructure interaction – Comparing simulation and experiment towards surface structuring using nanoparticles

Dissertation

zur Erlangung des akademischen Grades
doctor rerum naturalium (Dr. rer. nat.)

vorgelegt dem Rat der Physikalisch-Astronomischen Fakultät der
Friedrich-Schiller-Universität Jena

von
Henry Holland-Moritz
geboren am 30.03.1985 in Suhl

1. Gutachter: Prof. Dr. Carsten Ronning, Friedrich-Schiller-Universität Jena

2. Gutachter: Prof. Dr. Stefan Mayr, Universität Leipzig

3. Gutachter: Prof. Dr. Wolfhard Möller, Helmholtz-Zentrum Dresden-Rossendorf

Tag der Abgabe: 21.07.2016

Tag der Disputation: 18.10.2016

Experimentelle und theoretische Untersuchung der Ionen-Nanostruktur-Wechselwirkung

Miniaturisierung ist ein Schlagwort im Zusammenhang mit der fortschreitenden technologischen Entwicklung. Nanotechnologie ist dabei heutzutage eine dominierende Disziplin, um Geräte und Bauelemente immer kleiner und effizienter zu machen. Nanostrukturen zeichnen sich durch ein hohes Oberflächen-zu-Volumen-Verhältnis aus, welches zu teils neuartigen Eigenschaften im Gegensatz zu Volumenmaterialien führt. Nanostrukturen können durch verschiedenste chemische und physikalische Verfahren in großer Zahl und mit definierter Geometrie hergestellt werden. Derartige Verfahren arbeiten jedoch meist nahe oder im thermodynamischen Gleichgewicht, was die Möglichkeiten der Dotierung während des Strukturwachstums begrenzt. Ionenimplantation ist ein hyperthermales Verfahren, welches breite industrielle Anwendung bei der Dotierung von Halbleiterbauelementen findet. Ein Effekt, welcher bei der Bestrahlung von Objekten mit Ionen auftritt, ist das Zerstäuben, im Englischen und Folgenden auch Sputtern genannt. Dieser Effekt sorgt für eine Erosion des bestrahlten Objekts. Aus theoretischen Arbeiten ist bekannt, dass das erhöhte Oberflächen-zu-Volumen-Verhältnis zu einem verstärkten Sputtern bei Nanostrukturen im Vergleich zu Volumenmaterial führt. Experimentelle Befunde sind in der Literatur bisher jedoch kaum zu finden. Diese Arbeit untersucht die Wechselwirkung von Ionen mit Nanostrukturen und insbesondere deren Sputterverhalten sowohl theoretisch mit Hilfe von Monte-Carlo (MC)- und Molekulardynmaischen (MD)-Simulationen, als auch experimentell. Als Modellsystem dienen hierbei Gold-Nanopartikel.

Die Sputterausbeute wird für Ar^+- und Ga^+-Bestrahlung von Gold-Nanopartikeln als Funktion des Strukturdurchmessers, der Ionenenergie, der Geometrie und des Stoßparameters mit Hilfe des MC-Simulationsprogramms *iradina* simuliert und untersucht. Weiterhin wird die Winkelabhängigkeit der gesputterten Atome in Abhängigkeit vom Strukturdurchmesser für zufällige Ioneneinschlagspunkte auf den Partikeln untersucht. Die Winkelverteilung der gesputterten Atome, sowie die Größenabhängigkeit der Sputterausbeute wird zusätzlich mittels MD-Simulationen unter Zuhilfenahme des Programms *parcas* für sphärische Nanopartikel untersucht. Aus den MD-Resultaten werden zusätzlich die Temperaturen innerhalb der Partikel nach einzelnen Ioneneinschlägen als Funktion des Partikeldurchmessers diskutiert.

Die Simulationsergebnisse werden mit Hilfe von Experimenten an auf einem Siliziumsubstrat hexagonal angeordneten Gold-Nanopartikeln überprüft. Dazu werden die Proben mit Ar^+- und Ga^+-Ionen im Energiebereich von 10 bis 350 keV bestrahlt und hochauflösende Rasterelektronenmikroskopie (REM)-Aufnahmen vor und nach der Bestrahlung verglichen. Die experimentell ermittelte Sputterausbeute zeigt einen qualitativ ähnlichen Verlauf wie die Simulierte, liegt quantitativ jedoch über den Simulationsergebnis-

sen. Dieses Ergebnis wird durch *In-situ*-Experimente bestätigt, welche mittels Focused Ion Beam (FIB)-System und REM-Untersuchungen an einzelnen, mit $1-30\,\mathrm{keV}$ Ga$^+$-Ionen bestrahlten, Gold-Nanopartikeln durchgefÃijhrt wurden. Die Interaktion der bestrahlten Gold-Nanopartikeln mit dem darunterliegenden Substrat wird mittels Atomkraftmikroskopie (atomic force microscopy, AFM), Rastertransmissionsmikroskopie (STEM) und Rutherford-Rückstreu-Spektroskopie (RBS) untersucht. Die Gold-Nanopartikel sinken während der Ionenbestrahlung in das Siliziumsubstrat ein und bilden Goldsilizit, welches die Sputterausbeute von Gold signifikant reduziert. Des weiteren bilden sich bei Hochfluenzbestrahlung im Bereich von $1\cdot10^{16}\,{}^{\mathrm{atoms}}/_{\mathrm{ion}}$ Krater an den Partikelpositionen. Die Interaktion zwischen mehreren, regelmäßig angeordneten $25\,\mathrm{keV}$ Ga$^+$-bestrahlten Gold-Nanopartikeln in Bezug auf Redeposition von gesputterten Atomen wird mittels eines speziell zu diesem Zweck entwickelten MC-Programms untersucht und mit *In-Situ*-Experimenten mittels FIB und hochauflösender REM an Gold-Nanopartikelgruppen verglichen. Die Menge an redeponiertem Material hängt von der Größenverteilung der Partikel ab und ist vernachlässigbar für Partikelgrößen im Bereich der Ionenreichweite. Für Nanopartikeldurchmesser von 1 nm kann Redeposition jedoch zu Wachstum führen. Für signifikante Redeposition auf einem Nanopartikel müssen benachbarte Partikel entsprechend groß sein. Für Partikel mit einem Durchmesser größer der Ionenreichweite wird etwa 10 bis 20 % des gesputterten Materials kompensiert.

Nanostrukturen werden meist als funktionelle Bestandteile eines Gerätes betrachtet und untersucht. Eine weitere denkbare Anwendung von Nanostrukturen ist, sie als Bestrahlungsmasken zur Strukturierung von Substraten mittels Ionenstrahlen zu nutzen. Die zuvor gewonnenen Erkenntnisse werden deshalb zur Strukturierung von Lithiumniobat ($LiNbO_3$) mittels Ion Beam Enhanced Etching (IBEE)-Technik unter Zuhilfenahme von selbstorganisiert gewachsenen Nanostrukturmasken genutzt. Als Masken werden sowohl Gold-Nanopartikel verschiedener Durchmesser als auch Zinkoxid (ZnO)-Nanostrukturen genutzt. Die Maskenstruktur konnte für alle Maskentypen erfolgreich ins $LiNbO_3$-Substrat übertragen werden. Durch einen zweiten IBEE-Schritt können die Höhen der $LiNbO_3$-Strukturen erhöht werden, wobei die $LiNbO_3$-Strukturen hierbei selbst als Bestrahlungsmaske dienten.

Contents

1 Introduction

The steady acceleration of the technological progress is a remarkable feature of mankind. Since the industrial revolution in the 19th century, technology developed faster than ever before. Examplarily this is found in the evolution of the steam engine towards modern motors and engines, which was a huge leap from a revolutionary idea to a modern efficient and powerful combustion engine. Making applications smaller and more efficient is an important goal of scientists and engineers in almost all fields of technology. Besides mechanical machines and technology, the development of electronic and information technology went through a tremendous evolution since the beginning of the 20th century. Miniaturization also played a key role in this field of research, as the computing power increased with the number of transistors built into an integrated circuit. Gordon Moore predicted with his famous law in 1965 that every two years the number of transistors per chip approximately doubles [1]. Today, integrated circuits are still fabricated "top-down" by several masking, etching and irradiation steps using silicon (Si). However, to overcome the upcoming limitations of electronic integrated circuits, new fabrication and physical work principles are required, which is a key challenge for researchers. A further key challenge, which mankind and technology have to face, is the limitation of natural resources and a dawning ecological crisis, such that finding new ways to make technology more efficient is urgent. Nanoscience and nanotechnology give answers both to the challenges of miniaturization and the strive for efficiency.

Nanoscience developed as a new field of research within the past decade, as it is of interest in most scientific disciplines like biology [2, 3], chemistry [4, 5], medicine [6, 7] and physics [8–10]. Its often multidisciplinary nature helps to overcome the limitations of conventional technology [11–14]. Nanostructures are low dimensional systems, which offer new and diverse mechanical [15, 16], optical [17] and electrical [18, 19] properties, which differ compared to their bulk counterparts due to effects occuring on the nanoscale. The combination of small size and a tremendous amount of shapes and material compositions leads to new properties that may help to overcome the obstacles of conventional bulk technology. Based on these new properties, nanostructures can be utilized as central functional elements in a variety of devices, like field effect transistors (FET) [20], or nanowire lasers [21]. Furthermore, metalic nanoparticles for example offer a wide range of possibilities for plasmonic applications [22]. Moreover, optical and electronical properties of materials can be tailored by introducing quantum dots [23]. Another advantage of nanostructures is that they can not only be produced "top down" by lithography and reactive ion etching techniques [24, 25], but moreover by techniques that build the structures from "bottom up" in large numbers, such as chemical vapor deposition (CVD) [26] or various physical vapor deposition (PVD) [27] techniques.

In order to obtain materials with the required electrical or optical properties for certain applications or devices, they need to be structurally or morphologicaly modified or doped. Typical growth techniques work close to or at the thermal equilibrium, which can cause severe problems such as segregation of the dopant within the matrix [28] or at the surface [29]. The most established method in order to overcome these restrictions of thermal equilibrium is ion beam implantation, since it is a hyperthermal technique. This technique is nowadayas a standard method in semiconductor industry to tune the properties of materials beyond solubility limits of the dopant. In principle, any element can be forcefully incorporated in any target material using ion beam implantation. Furthermore, the doping concentration can be controlled by the ion fluence, whereas the dopant distribution in the target is determined by the ion energy. However, ion beam doping also has a drawback: if energetic ions traverse through a target, they interact with both its electronic system and its atoms and thus cause damage in the lattice. Therefore, a subsequent annealing step is usually required in order to remove damage such as point defects and defect clusters [30, 31], although several point defects might already anneal during the irradiation process [32].

An important effect which occurs upon ion beam irradiation is sputtering. Sputtering describes the emission of target atoms over the surface as a consequence of energy deposition by an impinging ion. Since sputtering is a surface sensitive effect, it is enhanced in ion irradiated nanostructures due to their large surface-to-volume ratio compared to bulk geometry [33, 34]. There are several techniques that make use of ion sputtering, such as secondary ion mass spectrometry (SIMS) to analyze the elemental composition of a surface or focused ion beam (FIB) milling for shaping the surface of samples and for preparing transmission electron microscopy (TEM) lamellas [35–37]. However, sputtering might also occur as an unwanted side effect in many cases, since it increases surface roughness of targets and leads to size decrease of irradiated structures. This sputtering induced size decrease is enhanced in nanostructures such that at high ion fluences it even leads to an increase of the doping concentration inside the structures [38] and can change size dependent optical properties of nanostructures [39]. Thus, the exact knowledge of the sputtering process on nanometer sized objects is essential for the fabrication of future nanoscaled devices.

The interaction of ions and nanostructures in terms of sputtering is mainly discussed theoretically in the literature [33, 40], however experimental investigations are rare [34]. Therefore, sputtering is investigated extensively within this thesis with matching conditions with the literature by simulations as well as experiments using gold (Au) nanoparticles as a versatile model system. Gold nanoparticles can easily be fabricated by various techniques in a wide range of shapes and sizes [41–43].

Computer simulations have been a powerful tool to investigate physical processes since computers have evolved rapidly at the beginning of the 20th century. Especially simulations based on Monte Carlo (MC) methods were popular back then and are heavily in use today. The most popular MC program for simulating ion-solid interactions is "Stopping and Range of Ions in Matter" (*SRIM*) [44]. The target is represented in *SRIM* as a layered structure, which is accurate for simulating ion ranges and sputter yields for bulk geometries. However, the sputter yields and dopant concentrations are underestimated if the *SRIM* results are carelessly applied to nanostructures. The recently developed codes "Ion Range and Damage in Nanostructures" (*iradina*) [45] and *TRI3DYN* [46] take into account the specifics of the nanogeometry and show significantly different results compared to *SRIM* in terms of sputter yields [47]. A different method, which fits the requirements of nanostructures, is the molecular dynamics simulation (MD) method. This method solves Newton's equations of motion for every single atom within an object during a physical process (such as ion implantation) over time. With knowledge of the exact interaction potentials, the evolution of the physical system with time can be modeled accurately. The main limiting factor of MD simulations, however, is the required computing power. In the framework of this thesis, the sputter yield of ion irradiated nanostructures is studied theoretically by MC and MD simulations as well as by a variety of experiments towards new insights into sputtering of nanostructures.

Following this introduction, this thesis gives a general overview over the fundamentals of ion-solid interaction in chapter 2. That chapter also outlines sputtering models of ion irradiated nanoparticles as well as the theory of MC and MD simulations. Chapter 3 briefly describes the investigated material systems and experimental techniques presented in this thesis. Furthermore, the MC code *iradina* and the MD code *parcas* [48, 49], which are used for simulations within this thesis, are described in this chapter. The following chapters present the simulation and experimental results of ion irradiation of nanostructures.

The ion-nanostructure interaction is discussed in chapter 4 based on simulation results by *iradina* and *parcas*. Spherical nanoparticles and cylindrical nanowires of various sizes are (virtually) irradiated with argon (Ar^+) and gallium (Ga^+) ions of different energies. The respective sputter yields are presented and discussed as a function of nanostructure size, ion energy and target geometry. Furthermore, the impact parameter is varied and a simple model based on Gaussian damage distributions is presented for describing the impact parameter dependence of the sputter yield for both geometries. In addition, the angular distributions of the sputtered atoms are extracted from the MC and MD simulation of ion irradiated spherical Au nanoparticles and are discussed as a function of the nanoparticle diameter. The temperature after the ion impact as a function of nanoparticle size and time is discussed by analyzing MD simulations of the 25 keV Ga^+ irradiation of spherical Au nanoparticles.

The sputter yield of ion irradiated Au nanoparticles is experimentally investigated in chapter 5 in order to test the simulation results presented in chapter 4. Hexagonally arranged Au nanoparticle arrays, produced by the Max-Planck Institue of Intelligent Systems in Stuttgart and the Institute of Physical Chemistry at the University of Heidelberg [50], are irradiated with Ar^+ and Ga^+ ions of energies ranging from 10 to 350 keV and are investigated statistically using high resolution scanning electron microscopy (SEM). Furthermore, single Au nanoparticles are irradiated with 1 to 30 keV Ga^+ ions in an *in situ* experiment using a dual beam FIB system to investigate the energy and size dependence of the sputter yield. The *in situ* experiment was performed in collaboration with Julia Graupner in the scope of her "Seminarfacharbeit". An additional *in situ* experiment was perfomred with 30 keV Ga^+ irradiation on a nanoparticle array to gain insights into the sputtering behavior of simultaniously irradiated nanoparticles with different sizes. Ion beam irradiation leads to an interaction between particles and substrate, which is investigated by atomic force microscopy (AFM) and scanning transmission electron microscopy (STEM) on Si substrates with Au nanoparticles on top. Additionally, Rutherford backscattering spectrometry (RBS) was performed on Ar^+ irradiated thin Au films on Si to investigate the influence of particle-substrate interactions on the sputter yields of Au. Nanoparticles are usually ordered in arrays after growth and in applications and are thus not irradiated isolated from other nanoparticles in the experiment. The interaction of neighboring ion irradiated nanoparticles is studied and presented in chaper 6. A dynamic MC simulation code was developed in the scope of this thesis for this specific purpose. A square shaped Au nanoparticle array is irradiated with 25 keV Ga^+ ions in the simulation. The diameter distribution of the nanoparticles follows the Gaussian size distribution extracted from the samples investigated experimentally in chapter 5. The sputter yields are calculated by *iradina* simulations or by the sputtering model presented by Järvi *et al.* [51]. Additionally, Järvi's model is scaled to fit the experimental sputter yields for 25 keV Ga^+ irradiation presented in chapter 5 as a third sputtering model. The angular distributions of sputtered atoms presented in chapter 5 are used. The evolution of nanoparticles within the array is investigated statistically by performing 120 simulations of a 4×4 grid with random nanoparticle sizes using Gaussian size distribution with mean diameters of 25 and 50 nm. The amount of redeposited material is compared to experimental results from chapter 5 and simulations with redeposition switched off. A 5×5 grid with a central nanoparticle of a certain diameter and two groups of equally sized neighbors with diameters of 20 and 50 nm, respectively, is simulated to investigate the influence of the size of the neighbors on the amount of redeposited material on the central particle. Subsequently, the *in situ* experiment with a nanoparticle array described previously was modeled by the code in order to investigate the role of redeposition on sputtering rates in the experiment. Consequently, simulation and experiment are directly compared to each other qualitatively and quantitatively.

So far, nanostructures were regarded as possible functional elements in devices, which can be modified and tuned by ion beams. Another application of nanostructures is presented by using them as irradiation mask in order to structure lithium niobate ($LiNbO_3$) by ion beams. Lithium niobate is an outstanding material with distinguished properties, like optical non-linearity, a large diffraction index and optical transparency over a large wavelength range, for various optical applications [52]. In contrast to conventional "top-down" mask preparation techniques, e.g. electron beam lithography, nanostructure masks can be grown "bottom-up" directly on the substrate and can be subsequently irradiated "top-down". The findings of ion-nanostructure interactions from chapters 4 to 6 are applied in order to realize a novel "top-up" approach of ion beam enhanced etching (IBEE) [53] instead of the conventional "top-down" approach. Nanostructures such as Au nanoparticles and ZnO nanowires, which are grown by self organization mechanisms, are used as irradiation masks to structure $LiNbO_3$ on the nanoscale. Simulations are performed with *iradina* to find the optimal parameters for Ar^+ and krypton (Kr^+) ion irradiation of x and z cut $LiNbO_3$ substrates with Au nanoparticle and ZnO nanowire masks on top. The samples are etched by a hydrofluoric acid (HF) solution after irradiation and the produced $LiNbO_3$ nanostructures are investigated by SEM. The height of these nanostructures is investigated as a function of substrate type, mask type, mask geometry and ion species. Subsequently, a second IBEE step is performed to increase the height of the nanostructures produced by 50 nm Au nanoparticles by using the $LiNbO_3$ nanostructures itself as irradiation masks. Furthermore, the height of the produced structures is investigated as a function of an introduced annealing step between irradiation and etching step. Additionally, the surface roughness of $LiNbO_3$ after IBEE is investigated as a function of this annealing time by using AFM. The work presented in this chapter was performed in collaboration with Sven Bauer in the scope of his master's thesis [54].

Chapter 8 gives a summary and conclusions of the main findings of this thesis. Additionally, an outlook is given towards finding deeper insights into the interaction between ion beams and nanostructures in order to optimize future nanostructure based applications and their preparation by ion beams.

2 | Fundamentals

2.1 Ion-solid interactions

If an energetic ion hits the surface of a solid, various processes take place depending on the projectile mass M_1, its nuclear charge Z_1, its kinetic ion energy E_0, the masses M_{2i} of the target atoms and their respective nuclear charge Z_{2i}. The index i describes the atom species for targets with more than one element in compound materials. The energy and mass ratio of projectile and target, the energy loss and the stopping of the projectile can be described by two mechanisms: electronic and nuclear stopping. The electronic stopping is caused by inelastic interaction of a highly energetic charged particle with the electronic system of the target. It is described by the theory derived by Bethe [55]. The nuclear stopping mechanism describes elastic collisions between the projectile and the atoms. The total energy loss, or stopping power, can be described by

$$S = -\frac{\mathrm{d}E}{\mathrm{d}x} = S_n + S_e,$$

where S is the total stopping power, S_n the stopping power caused by nuclear energy loss and S_e the energy loss caused by electronic stopping. Electronic stopping dominates for ion energies above MeV, as shown in figure 2.1a, where electronic and nuclear stopping powers are plotted for argon (Ar^+) and gallium (Ga^+) ion irradiation of gold (Au) as a function of ion energy. However, electronic stopping plays only a minor role at low ion energies, where nuclear stopping is dominating. Figure 2.1a shows that the energy losses caused by both mechanisms are equal at an ion energy of 1 MeV. As the ion energies used in the experiments within this thesis are well below 1 MeV, it is valid to neglect the contribution of electronic stopping for most of the discussions within this thesis. For details about electronic stopping the reader is referred to references [56–58]. The reason for the different interactions are different repulsive potentials $V(Z_1, Z_2, r)$ used for the description of the processes of the two-body interaction:

$$V(Z_1, Z_2, r) = \frac{1}{4\pi\varepsilon_0}\varphi(Z_1, Z_2, r)\frac{Z_1 Z_2}{r},$$

where ε_0 is the vacuum permitivity. The difference in interaction is mainly given by a screening function $\varphi(r, Z_1, Z_2)$, which models the interaction of the ion with the electronic system, depending on the distance between the interacting particles. A widely used universal screening function is the Ziegler-Biersack-Littmark function $\varphi_{ZBL}(Z_1, Z_2, r)$

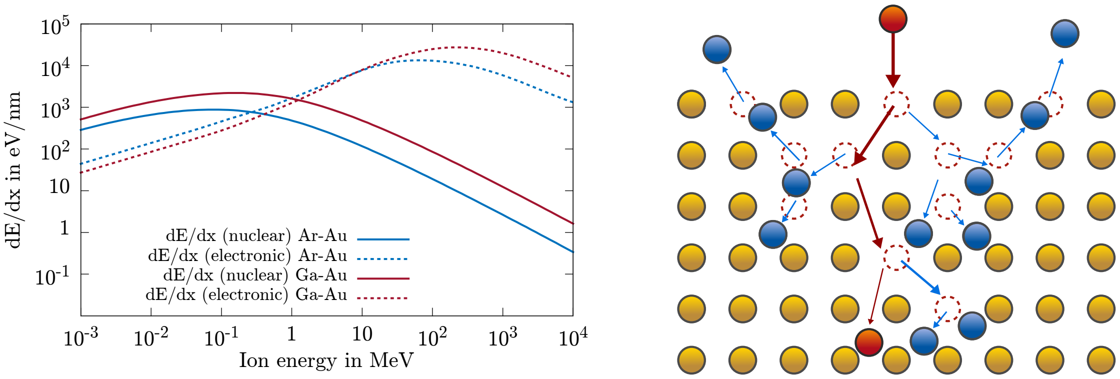

(a) **(b)**

Figure 2.1: (a) Nuclear and electronic energy loss dE/dx for Ar^+ (blue) and Ga^+ (red) ions in Au in double logarithmic scale. The dashed curves depict the electronic energy loss for the respective ion species. The data was simulated using *SRIM* [44]. (b) Schematic image of the damage cascade resulting from an ion traversing a crystal lattice. The red arrows indicate the ion path, while the blue arrows show the paths of recoil atoms.

[56], which is an empirically found function based on a function developed by Lindhard, Scharff and Schiøtt [59].

While the ion traverses the target, it collides with target atoms. This is schematically shown in figure 2.1b. An ion, depicted in red, travels with a certain energy and hits target atoms. With each collision, the ion loses energy and changes its direction by the scattering angle Θ, while also target atoms change their positions, if at least the displacement energy E_{displ} is transferred from the ion to the target atoms. The displacement energy is the minimum energy needed to knock an atom off its lattice position. The energy transfer from the ion to a target atom can be described by the kinematic factor K. This factor is the ratio of the ion energy after the collision versus the energy before:

$$K = \frac{E}{E_0}.$$

Since nuclear stopping can be described by elastic interactions of projectile and target, energy and momentum are conserved. Therefore, the kinematic factor is given by

$$K = \left(\frac{\sqrt{1 - \left({}^{M_1}\!/_{M_2} \sin\Theta\right)^2} + {}^{M_1}\!/_{M_2} \cos\Theta}{1 + {}^{M_1}\!/_{M_2}} \right)^2, \tag{2.1}$$

where Θ is the scattering angle of M_1 [57]. Note, that K only depends on the mass ratio of projectile and target and the scattering angle. The displaced atom itself then interacts with other target atoms and, in turn, can displace them from their lattice positions, and so on. A so-called collision cascade forms. The ion moves through the target until it has transferred all its energy to target atoms and then remains at a certain depth in the target. The length of the ion path projected to the incident direction is called ion range. Sigmund [58] classifies three types of cascades:

i Single-knock-on regime: Here, the ion mass M_1 is much smaller than the target atom mass M_2, or the ion energy is small. In this case, the target atoms do not receive a sufficient amount of energy to leave their lattice position and do not contribute to the cascade. Thus, only ion-atom interactions take place.

ii Linear cascade regime: In this regime, projectile and target mass are comparable, $M_1 \approx M_2$, and the ion energy is in the medium range. The ion can displace a number of atoms which can generate a cascade. In this regime, the binary collision approximation (BCA) is valid. The BCA assumes that all interactions inside the cascade occur only between two particles at a time (see also section 2.3). As this approximation greatly simplifies calculations, the BCA is a widely used assumption in simulation codes [56, 60].

iii Spike regime: Here, the ion mass is much larger than the target atom mass and/or the ion energy is high. In this case, high amounts of energy are transferred to the target atoms in a small volume. Therefore, the density of displaced atoms, which still interact with each other, is high and the BCA is not valid.

As a result of the collision cascade, the target lattice is damaged. This damage can take the form of vacancies or interstitial atoms. In particular, the impinged ion can occupy lattice sites or interstitial places. By this, materials are doped using ion beams [61, 62]. As a measure for the damage in the lattice the number of displaced atoms per ion, N_{displ}, can be used. A drastic form of damage is target atoms leaving the target, which is also depicted in figure 2.1b. This erosion of the target is called "sputtering" and forms the main topic investigated in this thesis. Therefore, sputtering is discussed separately in section 2.2 in detail.

A useful assumption for the interparticle interaction in the single-knock-on and linear cascade regime is the already mentioned BCA. For practical reasons, e.g. to achieve a certain doping concentration or a certain amount of lattice damage, a target is irradiated with a certain number of ions. The physical quantity for this is the ion fluence ϕ in units of $^{\mathrm{ions}}/_{\mathrm{cm}^2}$. To make the inflicted damage in a crystal lattice comparable for different parameters, such as ion energy and ion species, the normalized fluence

$$n_{dpa} = \frac{N_{displ} \cdot \phi}{N_0}, \tag{2.2}$$

can be used, where N_0 is the atomic density of the target material [53]. The unit of n_{dpa} is displacement per atom (dpa), which describes, on average, how many times each atom in the target was dislocated. A n_{dpa} of 1 dpa would theoretically represent an amorphous target after irradiation. Besides the primary interaction of ion and target atom and the inter-atomic interaction, thermal effects also influence the damage production. Note, that elevated temperatures can be locally caused by the ion beam. Such elevated temperatures can lead to dynamic annealing [32]. Therefore, amorphization of a target can also occur well above $n_{dpa} > 1$. On the other hand, dense collision cascades lead to amorphasization for $n_{dpa} < 1$ [53].

If the ion impinges into a crystalline target in direction of a low index axis, the energy loss of the ion is minimized [34, 57]. Thus, the ion range in the material is increased [63]. This effect is called "channeling". In this case, the damage in the target lattice is reduced.

2.2 Sputtering

Sputtering of planar surfaces Atoms, which have gained a certain amount of energy by collisions and have momentum in direction of the surface, can leave the target through the surface. To characterize the amount of sputtered material, the sputter yield Y is given as

$$Y = \frac{\text{number of emitted atoms}}{\text{number of impinged ions}}.$$

The theory developed by Sigmund [64] describes the sputtering process for monoatomic bulk material in agreement with experimental results [65–67]. The energy, which has to be overcome by the recoils, is the surface binding energy (SBE) U_0. It is defined as the energy, which needs to be transferred to an atom to remove it from the surface [68]. In this sense, it can also be called a sublimation energy of surface atoms. Sputtered atoms usually originate from surface-near atomic layers of the target, which got energy transferred from the inner cascade caused by the impinged ion of energy E_0 [30]. Considering the linear cascade regime and binary collisions, Sigmund defines a linear formula for the sputter yield Y [64],

$$Y = \Lambda F_D, \tag{2.3}$$

where F_D is the deposited energy per unit depth by the ion and Λ is a material factor. The deposited energy density inside the target can be expressed as

$$F_D = \alpha({}^{M_1}/{}_{M_2}, E_0, \Theta) \cdot N_0 \cdot S_n(E_0), \tag{2.4}$$

where $S_n(E_0)$ is the nuclear stopping power at an ion energy E_0, Θ is the angle of incidence with respect to the surface normal and N_0 the atomic density of the target material. Since Y has to be proportional to the number of collisions, it has also to be proportional to the nuclear stopping power. The factor α is a correction factor, which takes the angle of incidence Θ into account. It is $\alpha \propto \cos^{-f}\Theta$, with an exponent f of

$1 \leq f < 2$.
The material parameter Λ in equation 2.3 can, according to references [69, 70], be expressed as

$$\Lambda \cong \frac{4.2}{N_0 \cdot U_0} \frac{1}{\mathrm{nm}^2}. \tag{2.5}$$

It contains only material parameters and is proportional to the number of recoil atoms, which can leave the target by taking the atomic density and surface binding energy into account. The surface binding energy U_0 has typical values of 2 to 4 eV [71]. Equation 2.3 can be written using equations 2.4 and 2.5 as

$$Y \cong 4.2\alpha \frac{S_n(E_0)}{U_0} \frac{1}{\mathrm{nm}^2} = 4.2\alpha \left(\frac{\mathrm{d}E}{\mathrm{d}x} \right)_n \frac{1}{U_0} \frac{1}{\mathrm{nm}^2}. \tag{2.6}$$

Since Y depends on the nuclear stopping power, Y varies with the screening function in the interaction potential between ion and atoms, $V(Z_1, Z_2, r)$. The dependencies of the sputter yield for planar surfaces can be summed up as

$$Y = Y((^{M_1}/_{M_2}, E_0, \cos^{-f}\Theta, N_0, U_0, V(Z_1, Z_2, r)).$$

Considering compound materials or alloys, the sputtering of all components of the target material has to be conseived. Different sputter yields for different species in a compound are expected, since the sputter yield strongly depends on mass ratios, binding energies, etc. Therefore, sputtering can be preferential: the elemental composition of sputtered atoms differs from the elemetal composition of the irradiated region in the sample [70]. Let us assume two elements in the compound, A and B. Let the compounds $i, i \in \{A, B\}$, further have a partial sputter yield Y_i. The sputter yield of compound i is proportional to the concentration of atoms of species i, N_i, in the surface. Then the ratio of sputter yields can be described by

$$\frac{Y_A}{Y_B} = c \frac{N_A}{N_B},$$

where c is a proportional factor, which takes the SBE and the mass of the respective compound element into account. Malherbe *et al.* [72] derived from Sigmund's linear cascade sputtering [73] that

$$c = \left(\frac{M_B}{M_A} \right)^{2m} \left(\frac{U_B}{U_A} \right)^{1-2m}, \tag{2.7}$$

where m is a numerical factor for describing the differential cross section of the ion-solid interaction. The exponent m equals 0.5 for ion energies between 10 and 100 keV, it is

$0 \leq m \leq 0.5$ for ion energies smaller than 10 keV, while it is $m = 1$ for high ion energies larger than 100 keV [72]. Therefore, lighter elements are sputtered preferentially.

Sputtering of nanostructures Sigmund's theory of sputtering is an universal theory, which can be applied and adapted for a wide variety of problems concerning the ion irradiation of bulk structures. This theory needs to be modified for specific geometries when scaling sizes and geometries down to the nanoscale. Sputtering is a surface sensitive effect. If the surface of a geometry in relation to the volume is increased, sputtering is enhanced, especially when the ion range matches the particle size. It is impossible to give a universal theory of sputtering on the nanoscale due to the large variety of possible geometries. However, Järvi *et al.* [51] adapted Sigmund's theory of linear sputtering to a spherical nanogeometry, which is of major interest for this work and should be outlined briefly here. Analog to Sigmund, it is assumed that the sputtering yield is proportional to the energy deposited by the ion. An arbitrary surface ∂T is assumed, where the ion impinges at a point $r_0 = (x_0, y_0)$, as schematically drawn for a spherical particle in figure 2.2a. In analogy to equation 2.3, the intergral of the damage distribution over the particle surface gives the sputter yield for an ion impact at r_0 as

$$Y(r_0) = \Lambda \int_{\partial T} \mathrm{d}^2 r F(r, r_0), \tag{2.8}$$

where Λ is a material constant and $F(r, r_0)$ is the damage distribution, which is assumed to be a standard Gaussian with its maximum in a distance a below the impact point r_0. The damage distribution parameters can be extracted from computer simulations (see section 2.3 and 2.4). The total sputter yield is then the average of equation 2.8 over the total surface:

$$Y = \frac{\int \mathrm{d}^2 r_0 Y_0(r_0)}{\int \mathrm{d}^2 r_0} = \frac{\int \mathrm{d}^2 r_0 \Lambda \int_{\partial T} \mathrm{d}^2 r F(r, r_0)}{\int \mathrm{d}^2 r_0}. \tag{2.9}$$

The parameter Λ is adjusted in a way that the simulated sputter yield of planar surfaces is correct for planar surfaces. For a spherical particle with its center at the origin, equation 2.8 gives

$$\begin{aligned} Y_0(R, \Theta_0) = & \frac{2\pi \Lambda E_0}{(2\pi)^{3/2} \alpha \beta^2} R^2 \int_0^\pi \mathrm{d}\Theta \sin\Theta I_0 \left(\frac{R^2}{\beta^2} \sin\Theta \sin\Theta_0 \right) \\ & \times \exp\left(-\frac{R^2}{2\alpha} \left[\cos\Theta - cos\Theta_0 + \frac{a}{R} \right]^2 - \frac{R^2}{2\beta^2} \left[\sin\Theta + sin\Theta_0 \right]^2 \right), \end{aligned} \tag{2.10}$$

where α and β are the parameters of the Gaussiann damage distribution, R the sphere radius, Θ_0 the polar angle of r_0, and I_0 a modified Bessel function [74]. The average

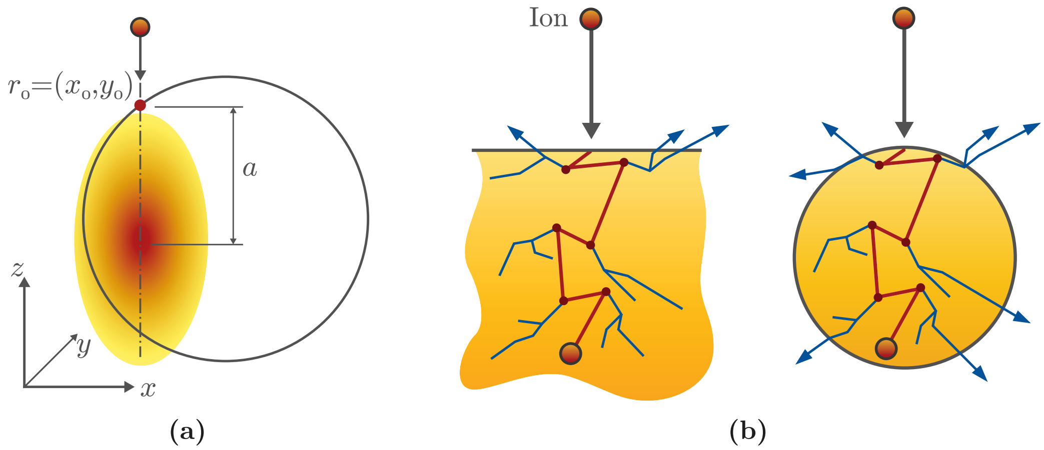

Figure 2.2: (a) Schematic image for the derivation of Järvi's sputtering model. The ion impinges on the particle's surface at r_0. The color gradient shows the damage distribution over the particle, which is assumed to be Gaussian. The maximum energy is deposited in the dark red region in a distance a below the impact point. Adapted from [51]. (b) Schematic comparison of the ion-solid interaction in bulk (left) and nanostructure (right) for the same damage cascade. Atoms are more likely to leave the nanostructure due to their larger surface-to-volume ratio compared to bulk.

sputter yield for impacts over the whole surface follows from equation 2.9 as

$$Y_{sphere}(R) = 2\int_0^{\frac{\pi}{2}} \mathrm{d}\Theta_0 \cos\Theta_0 \sin\Theta_0 Y_0(\Theta_0). \tag{2.11}$$

These integrals have no analytic solution for even the simple case of a spherical geometry and need to be evaluated numerically. The sputter yields of spherical geometries have, similar to bulk, an ion energy dependence due to the damage distribution as can be seen in equations 2.10 and 2.11. Additionally, the sputter yield is size dependent. The integral measures the damage distributon over the surface of the particle as visible in equation 2.10. If a particle becomes smaller, the damage distribution will have an increasing intersection area with the surface and thus a larger sputter yield. Schematically, the difference of sputtering in bulk and nanogeometry is shown in figure 2.2b. The situation is sketched for a bulk target on the left. The majority of collisions and damage can be found inside the material and only a few collisions can eject atoms through the surface. The situation changes for a nanostructure, which is drawn on the right hand side of figure 2.2b with the same cascade as for the bulk situation. The cascade has now more intersections with the surface, which results in an increased sputter yield. The sputter yield is plotted as a function of the particle diameter for Au nanoparticles irradiated with 25 keV Ga^+ ions in figure 2.3a, calculated by solving the integral from equation 2.11 numerically. Additionally, the simulated bulk sputter yield with the same irradiation parameters is shown [51]. The sputter yield for nanoparticles shows a characteristic trend and is larger than the bulk yield for all diameters larger than 3.6 nm. The reason for the trend is

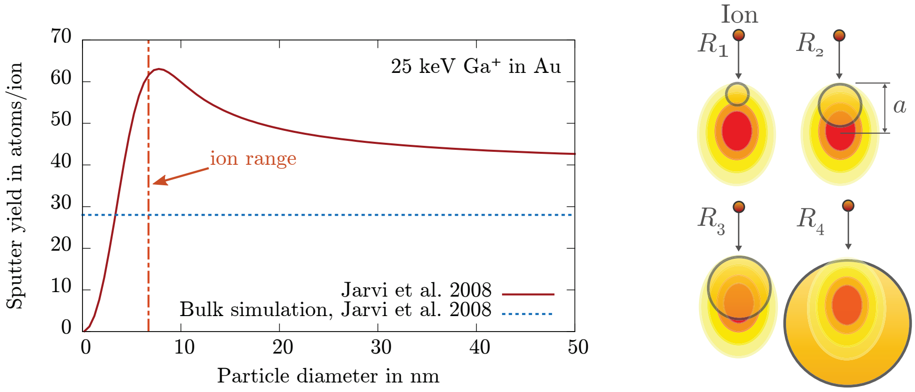

(a) (b)

Figure 2.3: (a) Sputter yield as a function of particle diameter. The red curve shows the results for the evaluation of equation 2.11 for 25 keV Ga$^+$ irradiation Au nanoparticles. The dashed orange line marks the ion range of the Ga$^+$ ions in Au (simulated with *SRIM* [44]). The horizontal dashed blue line shows the MD simualtion results for bulk geometry under equal irradiation conditions [51]. (b) Schematic image of the damage distribution in nanoparticles of different sizes. It is $R_1 < R_2 < R_3 < R_4$. The projected ion range is indicated with a.

schematically shown in figure 2.3b. Here, the damage cascade is drawn for an ion with a certain energy. For very small particles, like the one marked with R_1 in the image, only a small fraction of the damage cascade is located inside the particle. The maximum of the damage is still below the nanoparticle, which results in a small sputter yield. If the particle radius increases, a larger fraction of the cascade is inside the particle and the sputter yield increases, which is shown in figure 2.3b for the particle indicated with R_2. This case corresponds to the size region of nanoparticles below the maximum sputter yield ($\sim 7.5\,\text{nm}$). If the particle reaches a diameter which fits the ion range, the sputter yield reaches its maximum. This is the case for the particle marked with R_3 in figure 2.3b. Here, most of the ion's energy is deposited inside the particle and the damage cascade is spread over the whole particle. Therefore, it is most likely that many atoms leave the particle. If the particle radius increases further, the biggest amount of the damage cascade is then inside the particle, like shown in figure 2.3b with the particle marked with R_4. However, the intersection area of damage cascade and particle surface decreases with further size increase and; thus, the respective sputter yield decreases.

The sputter yield of nanoparticles does not converge towards the bulk value, even for very large particle sizes. The reason for this difference can be found in equation 2.4 and 2.10, where the dependence of the sputter yield on the angle of incidence is taken into account. The sputter yield is larger for larg angles of incidence with respect to the surface normal. Let's assume an arbitrary ion beam direction. The angle of incidence is the same for all impacts on a planar surface. Assuming a spherical target geometry, all angles between 0° and 90° have to be taken into account, which results in a larger sputter yield for the sphere. Nietiadi *et al.* [75] have shown that the sputter yield depends on the local curvature of a nanostructure. A sphere is practically curved for all sizes. Therefore, the sputter yield is increased in any case compared to bulk, although the curvature and with it the sputter yield decreases with increasing sphere size [75, 76].

2.3 Monte Carlo simulations

Monte Carlo (MC) methods are a useful tool to solve the equations modeling physical systems and their behavior under certain conditions using numerical methods based on random numbers. The basis for success of this method is the law of large numbers. The random numbers are generated by pseudorandom number generators [77, 78]. Consider a system with a large number of particles, e.g. a solid crystal. Even in small volumes of a few nm^3, a solid contains, depending on its density, some thousands of atoms. If the equations of motion for an ion impact on a crystal need to be solved, it would take a huge amount of calculations to model this interaction. Monte Carlo simulations, however, evaluate this problem statistically. The basic principle is to perform a random experiment many times to predict the result as the average of all obtained results.

A variety of codes based on the MC method has been developed to simulate ion-solid-interactions, like "Stopping and Range of Ions in Matter" *SRIM* [44] or "Ion Range And Damage In Nanostructures" *iradina* [45] (for details, see section 3.4). The basic principle of all these codes is almost the same. The experiment is represented by the ion parameters E_0, M_1, Z_1 and the ion position, as well as the material parameters M_{2i}, Z_{2i} and ϱ, where ϱ is the density of the material. Also, the interaction potential needs to be implemented. Usually, an universal potential like the ZBL potential is used [56]. The target structure is randomized, which means that the atoms have random positions and thus the target is assumed to be amorphous. The ion impact is then simulated n times. For each individual impact, the mean free path of the ion and recoils is determined randomly by the density of the material. The electronic energy loss is calculated along this mean free path, which is subtracted from the kinetic energy of the object. Depending on the density ϱ, a collision between ion and target atom happens randomly. If a collision takes place, the collision parameters are also chosen randomly from a given probability distribution. All collisions are treated by the BCA. Therefore, the motion of the ion and recoils through the target is considered as successive binary collisions. This assumption is no longer valid for small energies in the range of some eV, depending on the projectile and target masses [56, 60]. With each collision, the ion loses energy and, if a sufficient amount of energy is transferred, a recoil is generated, which also interacts with target atoms such as the ion, and so on. The scattering and energy loss is calculated deterministically using the randomly generated inputs. The result then is a statistic over all n impacts.

The interaction of many particles, like atoms in a solid with ions, can be evaluated in a reasonable amount of time with a sufficient accuracy using MC simulations by randomizing the parameters of the interactions. Mostly, they are used to calculate damage cascades, ion ranges, damage, scattering and energy loss. The limitations of MC simulation method is, however, that materials are treated at virtually 0 K, no thermal effects are taken into account. In addition, the BCA is a limitation, since the interactions described before are usually more complex than only binary collisions and can not treat many-body effects. Since only the average positions of target atoms are taken into account and particle movement is not treated dynamically, MC simulations can only treat equilibrium conditions [79]. Another drawback is that MC codes can not handle angle-dependent potentials [80].

It can be distinguished between static (SMC), dynamic (DMC) and kinetic (KMC) MC methods. Static MC methods, like *iradina* or *SRIM*, are only calculating statistics for a certain computed random experiment. The initial conditions are the same for each simulated ion impact. In DMC methods, e.g. the codes *TRIDYN* [81] and *TRI3DYN* [46], the condition of simulation $i+1$ depends on the result of simulation i or is the input for the next simulation. Kinetic MC methods can simulate the evolution of physical systems over time. Kinetic MC methods are a variation of DMC methods.

2.4 Molecular dynamic simulations

Molecular dynamic (MD) simulations model the evolution of physical objects in time, based on numerically solving Newton's equations of motion using a specific interaction model and potential. This simulation type overcomes the limitations of the BCA by taking many-body interactions into account. The method was first presented by Alder and Wainwright [79, 82].

The basic algorithm is schematically drawn in figure 2.4 for five particles. Let's consider a set of N atoms at positions $\mathbf{r}_i, i \in \{1, \ldots, N\}$ with a potential energy of the system $V(\{\mathbf{r}_i\})$. Following Newtonian mechanics, the system is modeled by pairs of coupled differential equations:

$$\begin{aligned}\frac{\mathrm{d}\mathbf{r}_i}{\mathrm{d}t} &= \mathbf{v}_i\\ \frac{\mathrm{d}\mathbf{v}_i}{\mathrm{d}t} &= \mathbf{a}_i = \frac{\mathbf{F}_i}{m_i} = -\nabla V_i\end{aligned}$$

The potential V_i is the potential energy, which particle i is receiving at position $\mathbf{r}_i$. This potential is a superposition of potentials of the other particles and results in a superposition of forces on particle i,

$$\mathbf{F}_i(\mathbf{r}_i) = \sum_{\substack{j=1\\ j\neq i}}^{N} \mathbf{F}(|\mathbf{r}_i - \mathbf{r}_j|)\hat{\mathbf{r}}_{ij}.$$

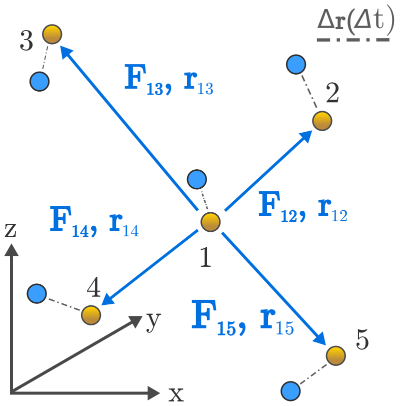

Figure 2.4: Schematic image of the calculation of many body interactions in MD simulations from the point of view of particle 1. The particles drawn in yellow represent the initial positions of the particles. The blue points show the positions after the calculation for a certain time step Δt using an arbitrary interaction potential. The particles are displaced by a distance $\Delta \mathbf{r}$ (dashed lines). The blue arrows show the distance vectors $\mathbf{r}_{ij}$ between particle i and j. Adapted from [83]

Here, $\hat{\mathbf{r}}_{ij}$ is the unit vector in direction of $\mathbf{r}_i - \mathbf{r}_j$. External forces are not taken into account.

Initial conditions $\mathbf{r}_i(t_0)$ and $\mathbf{v}_i(t_0)$ are set for representing the start of the simulation. Then the forces $\mathbf{F}_i(\mathbf{r}_i)$ are calculated for all particles. With these forces, the equations of motion are solved over a certain time step Δt to get the acceleration $\mathbf{a}_i$ and velocities $\mathbf{v}_i$ for each particle. The displacement $\Delta \mathbf{r}_i$ of particle i is then calculated via

$$\Delta \mathbf{r}_i \approx \frac{1}{2}\mathbf{a}\Delta t^2 + \mathbf{v}\Delta t.$$

The new positions $\mathbf{r}'_i$, shown as blue points in figure 2.4, for every particle i are then $\mathbf{r}'_i = \mathbf{r}_i + \Delta \mathbf{r}_i$. This procedure is repeated, until the maximum simulation time is achieved. This results in N^2 interactions, which need to be calculated for N atoms. This can lead to a serious amount of computing time for large systems, even for modern high performance computer clusters. Therefore, two simplifications could be made to reduce computing time. First, periodic boundary conditions (PBC) can be used for simulating large targets. Secondly, a cut-off radius r_{cut} can be defined, which defines the maximum distance from a particle, after which the potential is to assumed to be zero. Since most atomic interaction potentials decrease fast for $r \rightarrow \infty$ [84, 85], it is sufficient to calculate only the interactions between nearest neighbors.

But even considering the simplifications using PBC or nearest neighbor approximation, the calculations are time consuming for large physical systems. For a sufficient statistical accuracy, even for structures on the nanoscale, days of computing time are required [86]. Another difficulty using MD methods is finding accurate inter-atomic potentials for various element combinations. One method to find interaction potentials of metals is the embedded atom method (EAM) [87]. This method describes the total energy of a system of atoms as the sum of electrostatic interactions between neighbors and an embedding function, which correlates the electronic density with the local atomic position.

3 | Experimental and simulation methods

3.1 Material systems

Nanostructures and -particles Nanostructures have 0, 1 or 2 dimensions on the nanoscopic scale, so that the sizes of these structures are in the range of nanometers in one or more dimensions. Compared to bulk structures, the nano geometry may show various new properties caused by their large surface-to-volume ratio or quantum confinement. These mesoscopic properties are mainly determined by geometry, material composition and size of the structure [62]. Nanostructures can be fabricated from a wide range of materials and material systems ranging from metals [88], semiconductors [89, 90] to insulators [91], which makes them attractive for all sorts of applications in optical [92, 93], electrical [94] and optoelectronical devices [95, 96].

Gold nanoparticles Metallic Au NPs are interesting for optical [97, 98] and plasmonic applications [99, 100] and are a usefull model system to study the behavior of materials on the nanoscale theoretically [101, 102] as well as experimentally [103–105]. In particular, they are also used to model the ion-solid interactions in nanostructures [34, 40, 51, 106]. Such NPs can be easily synthezied by various techniques in many shapes and sizes [41–43, 107–109]. It is possible to achieve single crystalline Au nanoparticles with a highly circular cross section by using the method described by Ulrich *et al.* [50], which is described in detail in section 3.2.2. An example for a nanoparticle array fabricated by this method is shown in figure 3.3a.

Semiconductor nanowires can be modified with a wide range of ion species and energies in order to tune their electrical and optical properties [32, 62]. The material system zinc oxide (ZnO) crystallize in Wurtzite structure and is used as irradiation mask structure in this work. The stopping power of ZnO is sufficient to slow down ions, which are possible candidates for the irradation of substrate material for structuring such. ZnO nanowires are synthesized by the vapor-liquid-solid (VLS) mechanism, recipes can be found in reference [110].

Lithium niobate is a synthetic, insulating material, which does not exist naturally. It reveals transparency for wavelengths from 320 nm to 5.6 μm [111]. It shows electrooptical,

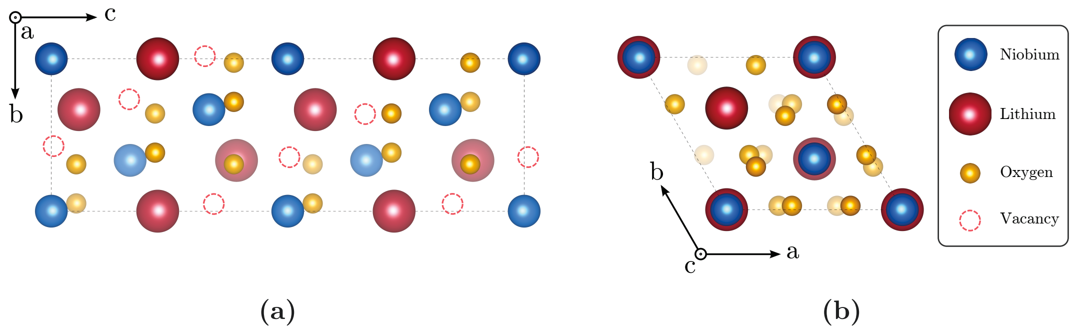

(a) **(b)**

Figure 3.1: Schematic images of the $LiNbO_3$ lattice in (a) a and (b) c direction, which correspond to x and z cut direction in $LiNbO_3$, respectively. More vacancies are "visible" in a than in c direction, depicted as dashed red circles in (a).

piezoelectrial, piezooptical, pyroelectrical and non-linear optical properties [52, 112]. The $LiNbO_3$ crystal is congruent with a ratio of Lithium (Li) to Niobium (Nb) of 0.946 [111] when fabricated by the Czochralski method [112].
Lithium niobate crystallizes in a hexagonal structure with a three-fold symmetry about the c axis. Usually two types of $LiNbO_3$ samples are available: x and z cut $LiNbO_3$. The x and z cut of $LiNbO_3$ correspond to the a and c directions of the lattice (compare figure 3.1). The difference between x and z direction of the crystal lattice is most interesting for this work. Both directions are shown in figure 3.1. The crystal consists of oxygen (O) octahedrons, which are aligned along the z direction. The centers of the octahedrons are filled alternating with Li or Nb atoms, or with vacancies. These vacancies are visibly along the a axis in figure 3.1a, but not along the c direction, shown in figure 3.1b.

3.2 Processing

3.2.1 Ion beam modification

Ion implantion is a technique to tune and modify the properties of materials. Ions are accelerated by an electric field up to a certain energy and impinge on the target. The Ar^+ irradiation experiments shown in this work were performed at the *ROMEO* implanter at the Institute of Solid State Physics Jena (IFK). With this implanter, theoretically all elements of the periodic system can be implanted into any target material. The ions are created in the ion source. If the source material is provided as a gas, atoms are ionized by energetic electrons or discharges. In case of a solid source material, ions are generated by sputtering or evaporation. After ionization, the ions are accelerated by a voltage of 30 keV towards a mass and charge filtering sector magnet. Subsequently, the ions are further accelerated by a static electric field up to an energy of 380 keV towards the sample. The ion beam can be sweeped by an alternating voltage to cover a target area of several cm^2 by ions. The possible ion beam current ranges from some nA to a few mA.

Focused ion beam system A focused ion beam (FIB) system is a device for imaging and modifying surfaces using ion beams. The system used for this work was a FEI Dual Beam Helios Nanolab 600i. Ion energies in the range from 1 to 30 keV with Ga$^+$ ions were used. The FIB works similar to a scanning electron microscope (SEM, compare section 3.3) for imaging applications, but instead of electrons, ions are used. Emitted secondary electrons are detected for imaging. The ions also sputter surface atoms off the sample due to the larger mass of Ga$^+$ ions compared to electrons. Furthermore, Ga$^+$ will be implanted into the surface. In any case, the ion beam will modify the surface in a destructive way. Due to fine focusing of the ion beam, the surface can be modified with a resolution of a few nm. For detailed information on the principles and possible applications of FIB systems, the reader is referred to references [113–116].

3.2.2 Fabrication and patterning of nanoparticles

A method to prepare regularly ordered Au nanoparticle arrays using self-organization mechanisms was developed by Ullrich *et al.* [50]. The strategy for producing these samples using a "bottom-up" technique is schmeatically outlined in figure 3.2. First of all, Au nanoparticles need to by synthesized. The seeds of Au particles are formed by reducing chloroauric acid ($HAuCl_4$) with oleylamine ($C_{18}H_{35}NH_2$) in a toluene solution [43]. These seeds grow as long as the Au precursor and oleylamine are provided. The desired size can therefore be controlled by the supply of these two components. The Au nanoparticles start to agglomerate when reaching a certain size, which can easily be seperated by ultrasonication. The oleyamine ligand forms a shell around the Au nanoparticles, which

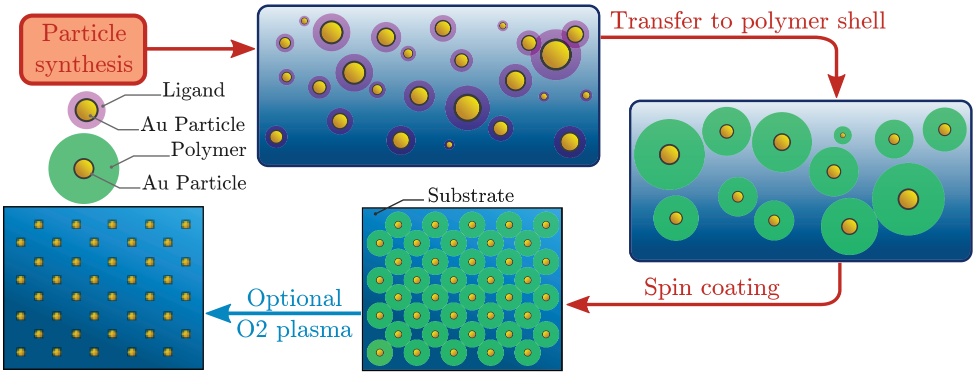

Figure 3.2: Schematic illustration of fabrication steps of ordered arrays of Au nanoparticles on a substrate. After synthesizing the particles in a solution, the ligands on the particle's surfaces are exchanged by a polysterene layer. The solution is then spin-coated onto a substrate, where the particles form a regular pattern. The samples can then be treated by a oxygen plasma to remove the polysterene. Adapted from [50].

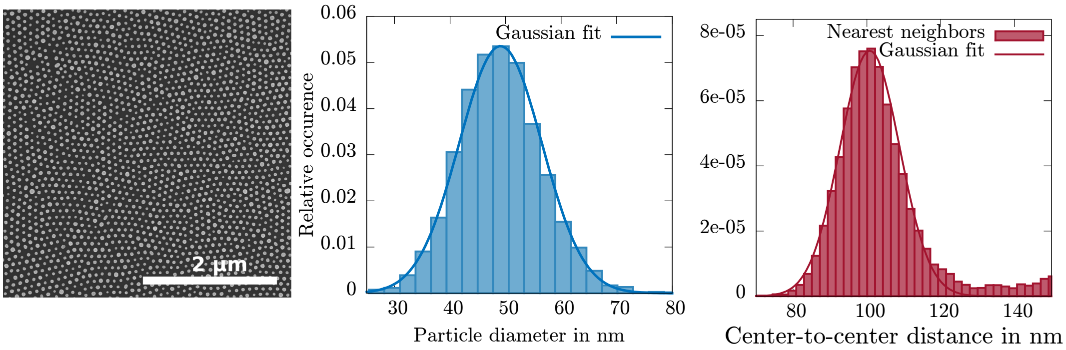

(a) **(b)** **(c)**

Figure 3.3: (a) Typical SEM image of hexagonal arranged Au nanoparticles on a Si substrate. (b) Size distribution of the Au nanoparticles shown in the SEM image in (a). (c) Center-to-center distance distribution of the Au nanoparticles shown in (a) for the nearest neighbors.

prevents the formation of large Au nanoparticle clusters. When the Au nanoparticles reach the desired size, the oleyamine ligand is exchanged by a structured polymer. In this step, the samples are washed with a thiol-terminated polysterene solution several times with a new solution each time. After the washing steps, the polymer coated Au nanoparticles are again dissolved in toluene [50]. The length of the polymer defines the final interparticle distances of the nanoparticles later on and prevents the nanoparticles from agglomerating in the toluene solution. This solution finally is spin coated on the desired substrate. In an optional step, the polymer is etched away using an oxygen plasma after spin coating.

All Au nanoparticle samples used in this work were fabricated by the group of Claudia Pacholski at the MPI for Intelligent Systems in Stuttgart. A typical SEM image of a sample is shown in figure 3.3a, where hexagonal arranged spherical Au nanoparticles on a Si substrate are visible in top view. The hexagonal arrangement is due to the fact, that the hexagonal order is the closest packing of spheres on a surface. The irregularities in the arrangement have their origin in the Gaussian size distribution of the Au nanoparticles, shown in figure 3.3b. The polymer has a specific length to define the interparticle distance. But due to different diameters of the Au nanoparticles, the packing density is locally in- or decreased, and thus stacking faults in the array occur. The average diameter of the particles was $\sim 50\,\mathrm{nm}$ on all samples with a standard deviation of ~ 7 to $8\,\mathrm{nm}$. The minimum and maximum particle diameters on the samples were approximately 20 and 80 nm, respectively. Figure 3.3c shows the distribution of the interparticle distances of the Au nanoparticles for nearest neighbors. Here, the center-to-center distance of the particles is plotted and a Gaussian distribution describes the behavior with a mean center-to-center distance of around 100 nm and a standard deviation of around 15 nm for nearest-neighbors.

3.2.3 Ion beam enhanced etching

Process Ion beam enhanced etching (IBEE) is a process to structure materials using ion beams and subsequent wet chemical etching. It has been developed for structuring materials, which are almost chemically inert [117]. The process is schematically drawn in figure 3.4. The first step is to place a mask on e.g. a $LiNbO_3$ substrate, which can be usually done by various lithography methods, like photo or electron beam lithography [117–119] (figure 3.4a). This mask will cover areas of the substrate, which should not be damaged by ions. The mask has to be thick enough in order to stop the ions to achieve only damage of the material in the uncovered areas. Typical mask materials are Si [119] or a layer system of SiO_2 and Chromium (Cr) [120, 121]. After masking, the substrate is irradiated with energetic ions, as shown figure 3.4b. The uncovered areas are damaged by the ions, as indicated with red areas on the $LiNbO_3$ in figure 3.4b. This is due to energy loss of the ions by the processes described in section 2.1.

The irradiation damage decreases the chemical resistance towards aqueous hydrofluoric acid (HF) [53]. In a third step, shown in figure 3.4c, the damaged areas are wet chemically etched by aqueous HF solution. As reported by Schrempel *et al.* [53], crystaline $LiNbO_3$ shows an etching rate of 0.1 nm/min for a 40 % aqueous HF solution at a temperature of 40 °C, which is negligible for any application. If the number of displacements in a damaged area exceeds a certain critical value n_{dpa}^{crit}, the etching rate increases rapidly. The critical value for the number of displacements depends on the mass M_i of the used ion species and can be determined by

$$n_{dpa}^{crit} \approx \frac{1}{1.19 + 0.13 M_i} \tag{3.1}$$

for $LiNbO_3$ [122]. The mass M_i should be given in atomic mass units u. The number of displacements corresponds to a measured defect concentration of $n_{da} = 0.60$ and $n_{da} = 0.25$ for x and z cut $LiNbO_3$ [122]. The etching rate saturates with increasing

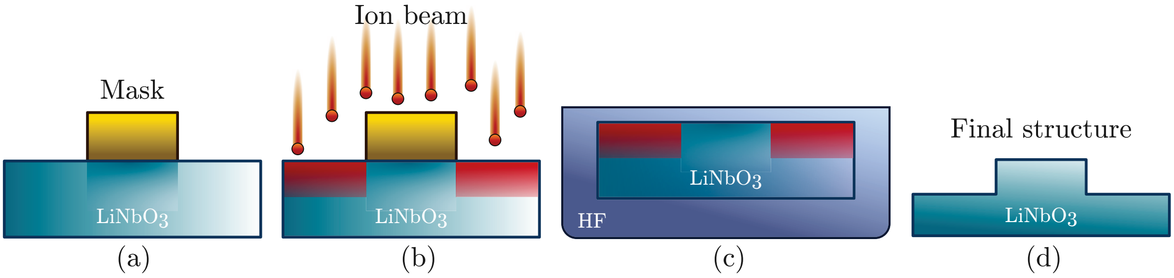

Figure 3.4: Schematic drawing of the steps of the IBEE process. (a) Masking the areas of the $LiNbO_3$ which should not be irradiated. (b) Irradiation of the sample with ions. Uncovered areas will be damaged by the ions. These areas are marked in red. (c) Etching of the uncovered areas in a HF solution. (d) Final structure after etching. Adapted from [122]

.

n_{dpa} at 0.4 dpa [53], which corresponds to a measured defect concentration of $n_{da} = 1$ [122]. The etching rate is also temperature dependent and increases with increasing temperature [123]. According to Reinisch *et al.* [123], the reason for the enhanced etching of damaged $LiNbO_3$ in HF is that hydrogen ions (H^+) from the aqueous solution saturate free bonds of O at the surface, which leads to a desorption of the O. Thus, the metallic atoms can be removed by HF or HF_2^-, leaving a free O bond at the new surface, from which the described reaction is repeated. The etching in the experiments presented in this thesis was done in a HF solution with a concentration of 3.7 % at a temperature of 55 °C for 15 min. After etching, the final structure is obtained (figure 3.4d). A uniform and constant damage over depth in the $LiNbO_3$ is required to achieve reasonable results for the desired structures. Therefore, it is necessary to irradiate the sample with ions of different energies and fluencies.

3.3 Analysis

Scanning electron microscopy is a method for imaging the morphology of samples using electrons. The electrons are emitted by a cathode and accelerated by an electric field towards the sample. The voltage for accelerating the electrons is in the range of some kV. A system of electrical and magnetic lenses focuses the electron beam on the sample to sizes of about 1 nm. Due to the scattering of the impinging electrons at atoms near the surface, primary and secondary electrons are emitted in backward direction, which can be detected as a function of the focused electron beam. The system used in this thesis was a FEI Dual Beam Helios Nanolab 600i. This system has a resolution of 1 to 2 nm. See references [124, 125] for further information.

Transmission electron microscopy Transmission electron microscopy (TEM) and Scanning transmission electron microscopy (STEM) are direct imaging techniques using electrons in transmission. The sample has to be thin, in the range of some nm, because the electrons have to penetrate the sample. Such thin lamellas can be prepared by a FIB system. Electron energies for these techniques are some hundred keV. When traversing the sample, some of the electrons are scattered at sample atoms, leading to a contrast in the image. One can directly image these transmitted electrons or can image a diffraction pattern in TEM. The main difference between STEM and TEM is that STEM uses an electron beam, which is scanned over the sample for image acquisition, while in TEM the electron beam is not scanned. The diffraction pattern in TEM mode allows to image the crystal structure of the sample using Bragg's law. The resolution of the STEM and TEM is on the atomic scale, below 1 Å. A JEOL JEM-3010 system was used in this work. Detailed information on STEM and TEM can be found in references [126, 127].

Energy dispersive x-ray spectrometry Atoms emit characteristic radiation when they are excited by external radiation. Energy dispersive x-ray spectrometry (EDX) uses an electron beam to achieve an excitation of the sample atoms. Characteristic x-ray radiation is emitted when they relax into the ground state. The elemental composition of the sample can be analyzed by detecting the x-rays. The relative amount of elements in the sample can be determined by analyzing the ratio of the respective signals to the total signal. The sample surface can be analyzed spatially resolved by the focused electron beam in a SEM. The EDX detector used for this work was an EDAX Genesis system in a JOEL JSM-6490 SEM system. An in-depth review of the EDX method can be found in references [128, 129].

Atomic force microscopy Atomic force microscopy (AFM) uses a cantilever with a tip with a radius of a few nm to probe the sample surface in order to measure the topology of the surface with up to atomic resolution. The cantilever is scanned over the sample surface and two measurement modes are possible: contact and tapping mode. In contact mode, the tip is in direct contact with the sample surface and the deflection of the cantilever is measured. In tapping mode, the tip is positioned slightly above the surface so that short-ranged interatomic forces like van-der-Waals forces, ionic, magnetic or electrostatic interactions lead to a deflection of the cantilever. While scanning the tip over the surface, the change in force is measured. This force change is proportional to the change in height of the sample surface. The force change also depends on the charge distribution in the sample surface, but does not depend on the electrical conductivity of the sample. Therefore, also insulating samples can be investigated. The used AFM used in this work was a Digital Instruments Multimode Scanning Probe Microscope. For more information on AFM, see references [130, 131].

Rutherford backscattering spectrometry A method for probing and analyzing the defect concentration and damage in a crystal using ion beams is Rutherford backscattering spectrometry (RBS). The sample is irradiated with low mass ions, e.g. H^+ or helium (He^+), with a relatively high ion energy in the range of a few MeV. The ions are scattered at the target atoms. The mass of the target atoms can be determined by measuring the kinetic energy of the backscattered ions under a certain angle by using the kinematic factor shown in equation 2.1 in section 2.1. The damage and defect concentration in the sample can be measured by comparing the so-called "random" and "aligned" spectra. An aligned spectrum is measured by irradiating a pristine sample in a certain lattice direction. The ion beam channels (see section 2.1) and the yield of backscattered ions decreases to a minimum. A random spectrum is measured by tilting the sample surface normal by 7° towards the beam direction. The sample will appear amorphous to the ions and the backscattering yield will be maximized. If an irradiated sample is measured in channeling direction, the amount of damage can be calculated by comparing this

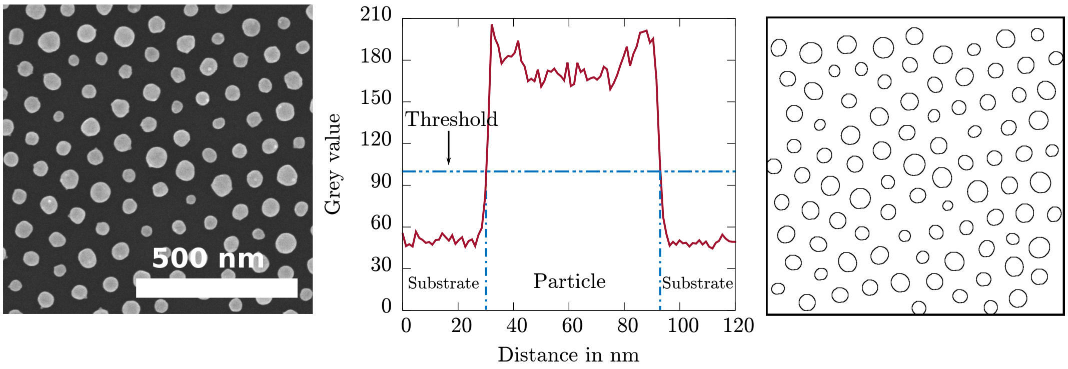

(a) (b) (c)

Figure 3.5: (a) SEM image of an array of Au nanoparticles on a Si substrate. (b) Grey value over the diameter of an arbitrary Au nanoparticle. The horizontal blue line marks the threshold value to distinguish between particle and substrate. The vertical blue lines show the edges of the particle. (c) Fitted ellipses on the edges of the Au nanoparticles after processing the SEM image shown in (a).

spectrum to a random and aligned spectrum. The code "Dechanneling of Ions in Crystals And Defect Analysis" (DICADA) [132] can be used to calculate the damage in the sample by comparing both random measurements and aligned measurements of irradiated and pristine samples. If the mass density of the sample is known, DICADA can calculate the damage in the material over the depth. The reader is referred to references [57, 133] for detailed informations on RBS.

Image analysis The analysis of SEM images was performed using the program *imageJ* [134]. It uses the evaluation of grey values to distinguish between "bright" Au nanoparticles and the "dark" Si substrate. The principle of this analysis is shown in figure 3.5. Figure 3.5a shows a typical SEM image of a Au nanoparticle array on a Si substrate. Figure 3.5b shows the grey values of an arbitrary Au nanoparticle over its diameter. A threshold for the grey value is defined to separate the particle from the substrate. The blue horizontal line is assigning this threshold in figure 3.5b. All settings for contrast and brightness in the SEM software were set to equal values for all measurements to achieve comparable experimental conditions and SEM images. However, the contrast differed between individual experiments. Therefore, the threshold is individually chosen for each experimental condition. From this threshold, the particle analyzing script of *imageJ* calculates the rim of each particle in the SEM image. An ellipse is fitted to the particles subsequently. The fitted ellipses for the particles in the SEM image in figure 3.5a are shown in figure 3.5c. Particles, which are positioned on the edge of the image, as well as particles, which undergo a certain circularity threshold, are excluded and not evaluated. For detailed information on the used parameters for the evaluation of the experiments see the respective sections in chapter 5.

Calculating sputter yields of nanoparticle arrays The algorithm described in the previous paragraph was applied to a nanoparticle array. If a Au nanoparticle exceeds a certain circularity, an ellipse is fitted. The particles were imaged in top view before and after irradiation and were assumed spherical because the SEM images provided informations only for lateral dimensions. From the areas of the fitted ellipse, A_0 and A, the sputter yield is calculated by

$$Y = \frac{\varrho_{at} \cdot \Delta V}{\phi \cdot A_0} = \frac{4\varrho_{at}}{3\sqrt{\pi}\phi \cdot A_0} \cdot \left(A_0^{3/2} - A^{3/2}\right), \tag{3.2}$$

where ΔV the volume change of the particle due to the irradiation, A_0 and A are the measured cross section areas of the nanoparticles before and after the irradiation, respectively, ϱ_{at} is the atomic density of the nanoparticle material and ϕ the ion fluence. The sputter yield was calculated as the average sputter yield over all measured particles of a sample.

Calculating sputter yields of single nanoparticles The shape of single nanoparticles imaged by high resolution SEM under an angle of 52 ° to the surface normal was approximated by a spheroid with rotational symmetry with respect to it's short semiaxis, which corresponds to an oblate spheroid. *imageJ* gives the parameters of the fitted ellipse, the axes lengths a and b for the short and long semiaxis, respectively, and the angle between the long semiaxis b and the x axis, α. An example SEM image with overlayed spheroid is shown in figure 3.6. The angle α is in the range below 5° in most cases. Due to rarely occurring image drift during image acquisition, the nanoparticles seem stretched in y direction in some cases. In these cases, α is larger than 45°. The angle α is then used as an indicator to make sure that the right axis is used for calculation of the volume. The volume of the spheroid is calculated by

$$V_{spheroid} = \frac{4}{3}\pi a b^2.$$

Thus, the sputter yield is calculated, analog to equation 3.2, by comparing the volumes of the spheroid before and after irradiation. For experiments using ion fluence series, where the volume is measured at each irradiation step, the sputter yield can be determined by

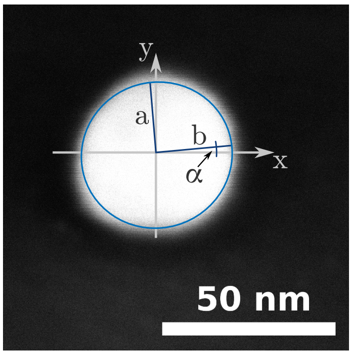

Figure 3.6: SEM image of a Au nanoparticle with a point of view of 52° to the surface normal of the sample. Additionally, an overlayed schematic of a fitted ellipse by *imageJ* is shown. Parameters a and b are the long and short semiaxis, respectively. The parameter α is the angle between the long semiaxis b and the x axis. The nanoparticle's shape is approximated by an spheroid with rotational symmetrie with respect to the short semiaxis.

measuring the slope of the experimentally obtained correlation of nanoparticle volume and ion fluence, $V(\phi)$. The sputter yield is then calculated by

$$Y = -m\frac{\varrho_{at}}{A}, \text{ with } m = \frac{\Delta V}{\Delta \phi}. \tag{3.3}$$

Here, A is the irradiated area and ΔV the volume decrease of the observed nanoparticle over a fluence intervall $\Delta\phi$.

3.4 Simulations

3.4.1 Established codes

SRIM The MC code *SRIM* [44, 56] is one of the most popular programs for simulating ion-solid interactions. It considers a planar target geometry, which can consist of layers of various materials. A number of ions N is impinging on one impact point. The calculations are according to the algorithm sketched in section 2.3 and the equations shown in [56]. As a result, *SRIM* gives stopping powers and ion range tables of various ion species in different target materials, ion and recoil distributions in the target, damage profiles and sputtering yields.

iradina The MC code *iradina* [45] is capable of simulating ion-solid interactions similar to *SRIM*. It is based on *corteo* [135], which makes use of pre-calculated energy loss tables in order to decrease computing times. The main difference to codes like *SRIM* is that *iradina* takes the 3 dimensional geometry of nanostructures into account. The principle is shown in figure 3.7. The desired structure, e.g. a sphere in figure 3.7a, is devided into equally sized slices, shown in figure 3.7b. These slices are further divided into equally sized cells, as shown in figure 3.7c. These cells are then filled with a certain material or with vacuum. The representation of the structure in the code is therefore a voxel model. As a result, the surface of most geometries will be represented with planar surfaces and

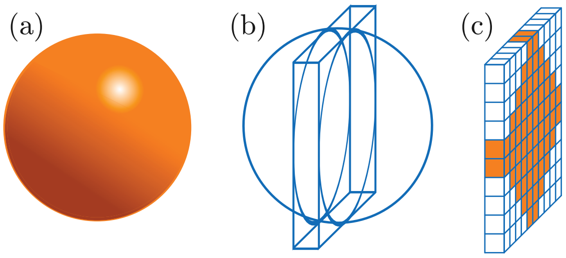

Figure 3.7: Schematic illustration of the representation of a 3 dimensional target structure in *iradina*. The geometry, which should be simulated (a) is devided in equally thick slices (b). Each of these slices is devided into equally sized cells (c). These cells are filled with material (colored) or with vacuum (white).

edges, which can cause small errors in the calculation of sputter yields, depending on the chosen cell size in respect to the size of the of the object [47]. For special geometries, like spheres and cylinders, the surface can also be represented analytically [136]. These special geometries were used for the calculations presented in chapters 4 and 5. Due to the more complex structures, the simulation results shown in chapter 7 were obtained using voxel models.

parcas The MD simulations presented in this work were performed using the code *parcas*. It was developed by Kai Nordlund, based on the algorithms presented in references [48] and [49]. The adaptive time steps and the electronic stopping are calculated by the algorithms presented in reference [80]. The basic principles are outlined in section 2.4. The output is a file, which contains the positions and velocities of all atoms simulated for every time step. From this, the energies and angular distributions of sputtered atoms can be derived.

3.4.2 Redeposition algorithm

A MC algorithm for modelling the ion irradiation of a nanoparticle array and the redeposition of sputtered atoms of one particle on neighboring particles was developed within the scope of this thesis. It enables a detailed study of the interaction of an array of nanoparticles. The simulation emulates the ion irradiation of a number of nanoparticles on a regular array on a flat substrate. However, particle-substrate interactions are not taken into account.

The design of the simulation volume is sketched in figure 3.8a. The simulation volume was divided into $n \times n$ equally sized cells with a squared base. The edge length of the base of a cell was s_{cell}, thus the side length of the simulation volume was $l = n \cdot s_{cell}$. The height h of the simulation volume, and therefore of all cells, was defined by the diameter of the largest simulated nanoparticle, D_{max}. The nanoparticles were placed in the center of the cells in x-y direction and at the bottom in z direction, as shown in the side view of figure 3.8a. Therefore, the lateral cell size determined the interparticle distance. The sizes of nanoparticles were randomly chosen from a given size distribution. The code was later modified in a way that the simulation volume is one cell with a side length l and a height D_{max}. In this cell, the respective particles could be placed by their central coordinates. Thus, it is possible to represent the array of a certain SEM image in the code and directly compare experiment and simulation. For any randomly generated number in the described algorithm, the Mersenne twister algorithm [78] was used for producing pseudorandom numbers. The sputter yield Y is selected by the sputter model in use and depends on the size of the hit nanoparticle. Each sputtering event is considered seperately in the following description.

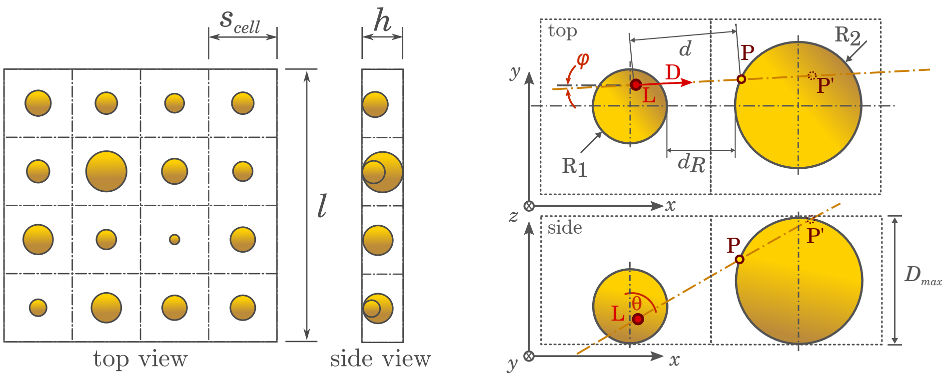

(a) **(b)**

Figure 3.8: (a) Schematic drawing of the simulation volume for the simulation of ion irradiation of a nanoparticle array in top and side view. The volume is a cuboid consisting of $n \times n$ equally sized cells with a squared base. The side length of a cell is the cell size s_{cell}. The total edge length of the volume is $l = n \cdot s_{cell}$. The heigth of the simulation volume, h, is defined by the largest particle diameter simulated. (b) Schematic of the redeposition calculation principle for sputtered atoms from a particle 1 onto a particle 2, which have a rim-to-rim distance of d_R, in top and side view. The atom is leaving particle 1 at the leaving point **L** in direction of vector **D**. **D** is defined by the azimuth and polar alngles φ and Θ. The line defined by D and L intersects with particle 2 at points **P** and **P′**. For the calculations, only the intersection point **P**, which is in closer distance d to particle 1, is taken into account.

The redeposition of a sputtered atoms from a nanoparticle 1 to a nanoparticle 2 is schematically drawn in figure 3.8b. A number N_i of ions is simulated. The number of ions is calculated by the ion fluence times the base area of the simulation volume, $A = l^2$. For each ion, a tuple of two random numbers (x_i, y_i), each between 0 and l, is generated as the impact position in the simulation volume. If a particle is selected to receive an ion, a random leaving position is generated on the particle's surface. The direction (Θ, φ) of the ejected atom, where Θ is the polar and φ is the azimuthal angle, is calcluated by the size dependent angular distribution of sputtered atoms. The angles Θ and φ define the direction vector **D**. The angular distribution was calculated for a number of particles sizes ranging from 1 nm to 100 nm in intervals of 1 nm using *iradina* for freestanding spherical nanoparticles. Details on these calculations are given in section 4.3. The angle φ is selected uniformly between 0 and 2π, beacuse of symmetry in this direction (see figure 4.5b in section 4.3). After finding the direction of the sputtered atoms, the algorithm needs to find out, whether an atom is redeposited or not. A sputtered atom is considered as deposited if the line of direction of the atom intersects with a sphere outlining an other nanoparticle in direction of **D**. If the atom is redeposited, the diameter of particle 2 is recalculated by adding an atomic volume V_a to the particle volume V_p; $V_p' = V_p + V_a$. Then the new diameter of particle 2 is calculated for the new volume V_p'. The volume of particle 1, which was hit by the ion, is recalculated similarly by reducing its volume by $Y \cdot V_a$ for each ion impact.

The main loop of the simulation runs over the number of ions. If an ion hits a particle, the former described method of emission and redeposition of atoms is applied. A loop runs over all particles in the simulation volume. If the line of direction is not intersecting with a particle on the pattern, it will intersect with the border of the simulation volume. In cases of intersection with the planes of $z = 0$ and $z = D_{max}$, the atom is deposited in the substrate or sputtered upwards. No redeposition on other nanoparticles is possible in these two cases, therefore the atom is not followed anymore. In case of an intersection of the line of direction and the $x - z$ or $y - z$ plane, PBC's are applied. In case of applied PBC, the atom will reenter the simulation volume on the opposite border plane. The loop over all nanoparticles is started again. If the line of direction is conducting between the nanoparticles, even with applied PBC, a cut-off condition is necessary. A cut-off distance d_{cut} is defined, after which the atom is no longer pursued. Therefore, the traveled distance d is calculated. If $d > d_{cut}$, the simulated atom is skipped and next sputtered atom is simulated.

The algorithm was implemented in `Python` as a dynamic MC code. The results are shown in chapter 6. A schematic of the algorithm can be found in Appendix A.

4 | Simulation and modeling of sputtering of nanostructures

This chapter presents the results of simulations performed with the MC code *iradina* and the MD code *parcas* to investigate the sputtering behavior of ion irradiated Au nanoparticles. The main results are the sputter yield as a function of ion energy and nanoparticle size as well as angular distributions of the sputtered atoms. Furthermore, the influence of the target geometry on the sputtering behavior was investigated. Additionally, the temperature development inside a nanoparticle after the ion impact was investigated using MD simulations. The MC simulations were done in collaboration with Christian Borschel, Andreas Johannes and Emanuel Schmidt. Parts of this chapter were published in references [32] and [137]. The MD simulations were performed on the Alcyone cluster at the University of Helsinki in collaboration with Kai Nordlund, Flyura Djurebakova and Andrey Ilinov.

4.1 Simulation parameters and details

The MC code *iradina* [45] was used to perform a wide range of simulations to investiagte the sputtering behavior of ion irradiated Au nanoparticles and nanowires. The special nanoparticle and nanowire version of the code was used for these simulations, where the surfaces of the nanostructures are represented as an analytical function [136]. The simulation volumina for the simulated geometries are schematically shown in figure 4.1. The direction of the ion beam is defined as the x axis. The spherical nanoparticle was centered inside a cubic simulation volume (see figure 4.1a). The distance of the nanoparticle's rim to the border of the simulation volume was at least 1 nm in all directions in order to calculate sputter yields correctly. The nanowire was presented as one cell in z direction with PBC's applied in this direction (compare figure 4.1b), whereat the lingth of the cylinder matched the cell size in z direction. The cylinder was centered in $x - y$ direction. Additionally, bulk geometry was modeled by making a cuboid inside a cube with one layer of cells of vacuum on top and PBC's in y and z direction (compare figure 4.1c). The number of simulated ions was 10 000 unless otherwise stated. The ion impact position was randomized over the simulation volume with a beam spread of 1 nm. The SBE of Au was chosen to be 3 eV, which is a standard value in MC simulations and obtained from the *SRIM* material data base [44]. The displacement energy was set to 20 eV and the lattice binding energy to 2 eV. The implemented interaction potential was

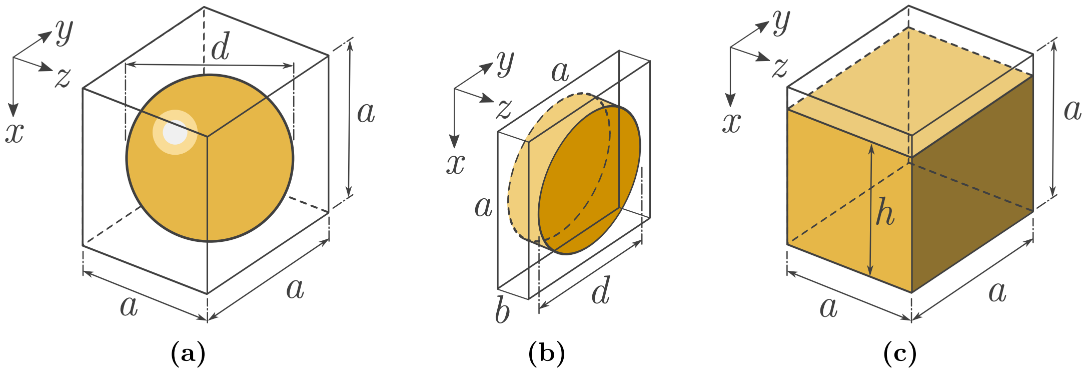

(a) **(b)** **(c)**

Figure 4.1: Schematic illustrations of the simulation volumes used in *iradina*. (a) Cubic volume with a sphere in the center. No PBC's are applied. (b) Cubiod volume with a cylinder, which is centered in $x - y$ direction. The length of the cylinder corresponds to the side length b of the simulation volume. PBC's are applied in z direction. The diameters d of sphere and cylinder in (a) and (b) are 2 nm smaller than the edge length a of the respective volumina. (c) Cubic simulation volume for bulk geometry. The heigth h of the bulk material is 1 nm smaller than the height of the simulation volume a. PBC's are applied in y and z direction.

the universal ZBL potential [56] and the straggling was calculated using Chu's model [138]. The ion energies were varied from 1 to 350 keV and the nanostructure's diameters ranged from 1 to 250 nm.

The MD simulations were performed using the code *parcas* with the same parameters as for the simulations used in reference [34]. A nanoparticle with a certain radius was cut out of a fcc crystal lattice. The interaction between Au atoms was modeled using the EAM potential described by Foiles *et al.* [139]. High energy interactions, like ion–atom interactions, were described by the universal ZBL potential [56] for energies larger than 5 eV. The primary ion energy was set to 25 keV to make the results comparable to simulation results presented in the literature [33, 51] and to experimental results (see chapter 5 and reference [137]). The diameter of the Au nanoparticles ranged from 2 to 40 nm. A number of 100 simulations were performed for each size to achieve reasonable statistical accuracy. Each nanoparticle was randomly rotated by three Euler angles before each simulation to cover a wide range of possible impact situations. The ion impact position was also chosen randomly on the nanoparticle. The simulated time was 200 ps in total with 26 time steps. Adaptive time steps were used to make sure that the time step is small enough for high energies and velocities at the beginning of the simulation [80]. The lattice was relaxed before the actual simulations to a temperature of 300 K using Boltzmann's distribution to make the situation more realistic. There was no temperature control in the actual simulations, which means that the simulation volume was treated as an isolated thermodynamic system. Most of the simulations were performed twice, one time with a free standing nanoparticle, the other time fixing the bottom atomic layer of the nanoparticle to emulate the substrate. The latter method has been chosen, since up to now no sufficiently realistic interaction potentials between Au and Si were developed.

4.2 Sputter yields

Energy dependence Various ion energies are usually used in ion irradiation experiments. Therefore, the sputtering process was simulated by using various ion energies on different target geometries. Figure 4.2a shows the MC determined sputter yield as a function of the ion energy for Ar^+ and Ga^+ ions for spherical nanoparticles and cylindrical nanowires. Additionally, the simulation results for bulk geometry are shown for both ion species. The target material was Au in all cases. The nanostructure's diameters were kept constant at 50 nm.

The first thing to notice is that the sputter yields for nanostructures are higher by a factor of 3 to 6 compared to bulk, depending on the ion species and geometry of the nanostructure. The bulk values reach their maximum at relatively low ion energies of around 15 to 20 keV and then slowly decrease. The damage cascade for bulk is near the surface for ion energies lower than 15 keV, where the sputter yield increase is due to a larger amount of energy transferred from the ion to surface-near atoms. With further increasing ion energy the intersection area of cascade and surface decreases and the ion deposits more energy deeper below the surface. Therefore, the cascade has less intersection with the surface and thus reaches a maximum at low ion energies. In contrast, the nanostructures show a steep increase of the sputter yield with increasing ion energy and a decrease of the sputter yield after a distinct maximum with further increasing ion energy. The sputter yield is larger for larger ion masses, as visible in figure 4.2a. The mass of Ar^+ is ~ 0.57 times the mass of Ga^+, while the maximum sputter yield of Ga^+ irradiation is about two times larger than the maximum of the Ar^+ irradiation. This is a result of the denser collision cascade of heavy ions compared to lighter ones. Another noticeable

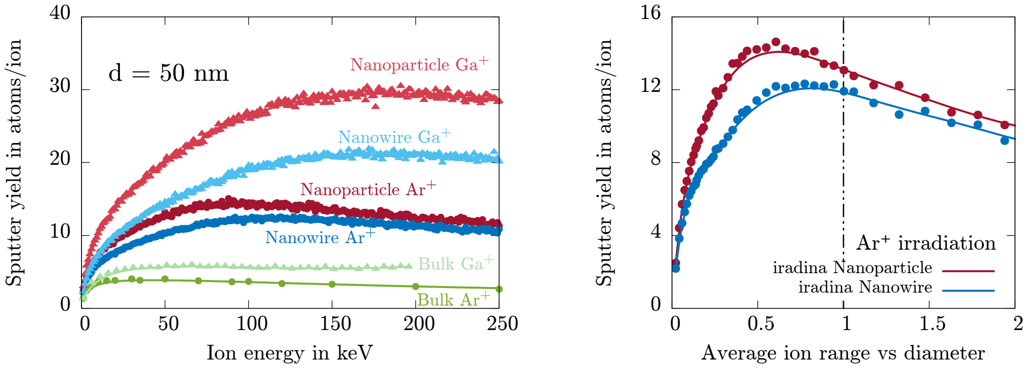

(a) (b)

Figure 4.2: (a) Sputter yield as a function of ion energy for Ar^+ (dots) and Ga^+ ions (triangles) for spherical (red) and cylindrical (blue) Au nanogeometries. The results for bulk geometry are plotted in green. The diameter of the nanostructures was fixed to 50 nm. (b) Sputter yield over the ratio of ion range versus the structure diameter for Ar^+ ion irradiation for both spherical and cylindrical geometry.

fact is that the sputter yield of the spherical nanoparticles are enhanced compared to the cylindrical nanowires. This result is in line with results obtained by Urbassek *et al.* [76]. The reason for this behavior is discussed later in this section in detail.

The maximum of the sputter yield as a function of ion energy is given by the average ion range of an ion in the material. This is shown in figure 4.2b, where the sputter yield is plotted as a function of the ratio of the ion range versus the structure diameter for nanoparticles and nanowires for Ar^{+} ions. The ion range data was taken from *SRIM* range calculations. The maxima of the sputter yields are slightly below the ratio of range versus diameter of 1 (marked with a black dashed line in figure 4.2b), because the damage cascade extends further than the average ion range. Sputtering takes place mainly on the nanostructure's hemisphere facing the ion beam, if the ion energy is smaller than the energy with a range of the nanostructure's size, E_r. If the ion energy exceeds E_r, the ion can traverse the nanostructure and less energy is deposited inside. The sputter yield depends on the intersection of the damage cascade with the structure's surface, as Nietiadi *et al.* [140] showed. In both above described cases of ion energies smaller and larger E_r, the intersection area of damage cascade and nanostructure surface is smaller than in the case if the ion energy is $\sim E_r$.

Size dependence The simulation results obtained by *iradina* for the sputter yield as a function of the nanstructure diameter are shown in figure 4.3a for nanoparticles and nanowires. The simulated ion species was Ga^{+} with an ion energy was set to 25 keV. The sputter yield increases fast with the structure's diameter up to a maximum of 25 and 30 atoms/ion, for cylinder and sphere, respectively. The sputter yield is much higher compared to the bulk situation, which is 5 atoms/ion, for both structures. The trend of the simulated curves by *iradina* is in line with the theoretical results presented in figure 2.3a in section 2.2.

The MD results for the size dependence of the sputter yield are shown in figure 4.3b for spherical nanoparticles. In addition, the results by Järvi *et al.* and the respective model are plotted [51]. The trend of the simulation results are the same as in the results obtained by *iradina*. However, the theoretical obtained sputter yield of the Järvi model is two times larger than the MC results (see figure 4.3a). This is due to the fact that the model by Järvi is based on MD simulations. The maximum of the sputter yield is at the same nanoparticle diameter of ~ 7 nm in both simulations. The sputter yields obtained by the MD simulations are one order of magnitude larger than the MC results by *iradina*. They are even roughly 4 times larger than the MD results obtained by Järvi *et al.* and the respective model. The reason for this may be due to different input parameters and potentials used for both simulations. Unfortunately, reference [51] gives no detailed information on the simulation inputs, which makes it hard to identify the reason for the difference in both simulations. The simulation inputs, potentials and models used in this

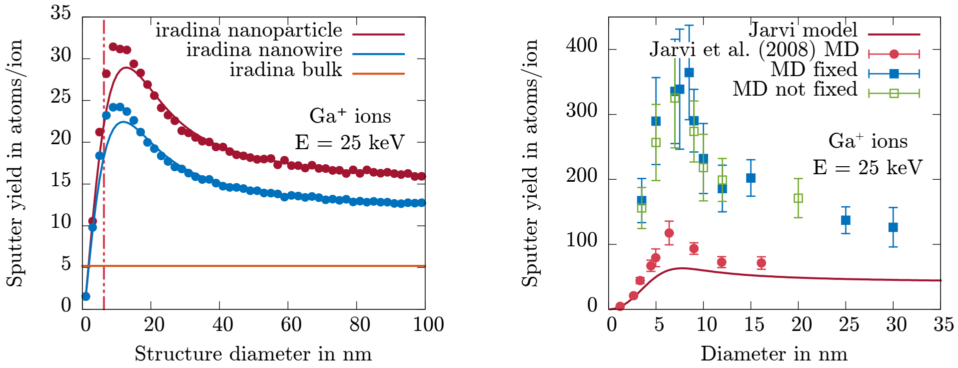

(a) **(b)**

Figure 4.3: (a) Simulated sputter yield as a function of the nanostructure diameter for 25 keV Ga^+ irradiation, simulated using *iradina*. The horizontal orange line shows the results for bulk geometry. The red and blue data points show the results for nanoparticle and nanowire geometry, respectively. The dashed red verticall line shows the ion range of 25 keV Ga^+ ions in Au (6.7 nm). (b) MD simulation results of spherical Au nanoparticles irradiated with 25 keV Ga^+ ions. The results are shown for fixed (blue) and free (green) nanoparticles. The model and MD results by Järvi *et al.* [51] are shown as red line and red points, respectively.

thesis were the same as for the simulations shown in reference [34], except ion species, energy and target geometry. The results for fixed and free nanoparticles are comparable in the range of the statistical errors. The data points for the fixed nanoparticles, however, are systematically shifted towards larger sputter yields. This is caused by reflection of energy and momentum of atoms in the particle on the fixed atoms, since they can not move. Therefore, they seem to have an infinite mass. The difference of both simulated situations is decreasing with increasing nanoparticle size.

Both simulation methods, MC and MD, produce sputter yields as a function of the nanoparticle size which are comparable qualitatively. The difference in the amount of sputtered atoms at a certain ion energy is a result of the simple assumptions of the BCA and the more detailed calculations in MD codes in contrast. Especially the inclusion of thermally driven effects like evaporation and cluster sputtering in MD lead to a much higher sputter yield (compare reference [34] and section 4.4).

Impact point dependence The previous results showed that the sputter yield depends on the intersection area of damage cascade and particle surface. This area changes with the impact parameter b of ion and nanostructure. The impact point of the ion was varied from the center to the rim in *iradina* and only defined impacts without beam spread were simulated. The number of impact points was 25 with b ranging from 0 (center) to R (nanoparticle/wire radius). The simulated number of ions for for each impact point was 10 000.

The *iradina* results are shown in figure 4.4. Figure 4.4a shows the sputter yield as a function of the impact point of 25 keV Ga^+ ions for different nanostructure sizes of nanoparticles (solid lines) and nanowires (dashed lines). The results for different sizes can be explained by the ratio of particle size to ion range. If the ion range exceeds the size of the nanoparticles and nanowires for small diameters, then this causes sputtering mainly in forward direction (in beam direction). This can be seen for the 10 nm structures in figure 4.4a. Here, the sputter yield is almost constant over the impact parameter, but decreases for large impact parameters b, where the ion traverses the particle by depositing negligible energy. The trend of the sputter yield over the impact parameter changes with increasing structure diameter. According to Nietiade *et al.* [140], the sputtering changes from forward to lateral sputtering. If the nanostructures are larger than the ion range, forward sputtering is supressed, because fewer atoms have enough energy to traverse the particle towards the rim and overcome the SBE in case of impact

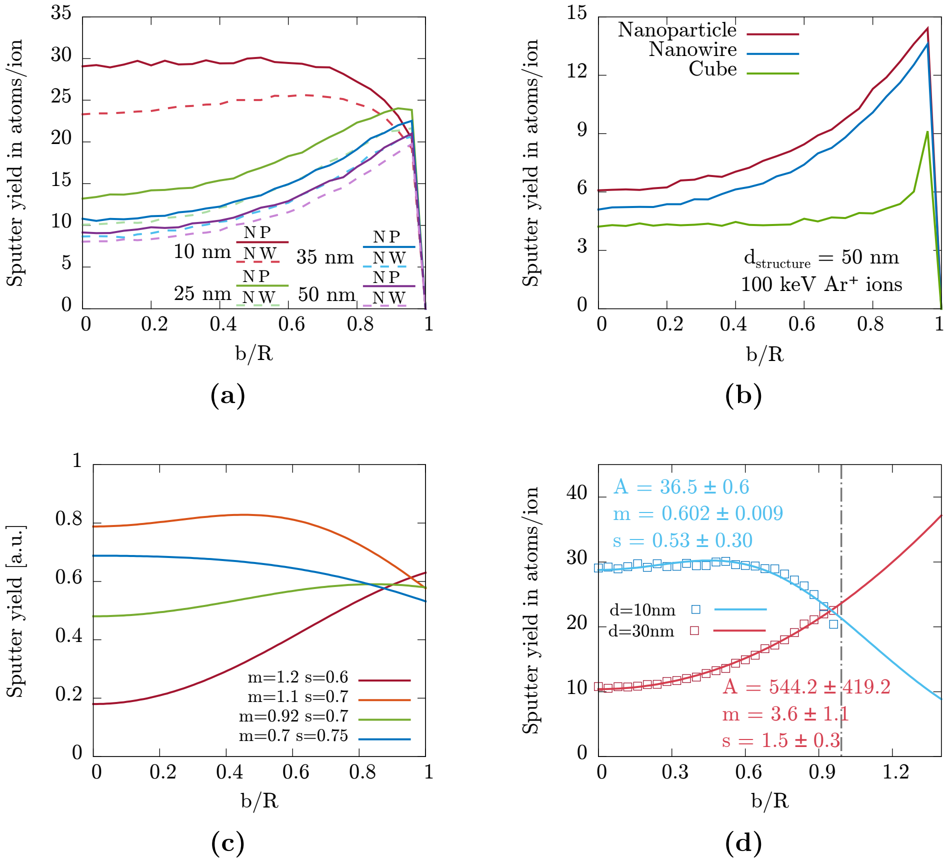

(a) **(b)** **(c)** **(d)**

Figure 4.4: (a) Simulation results of the sputter yield as a function of the impact parameter for different nanostructure sizes for spherical nanoparticles (solid lines) and cylindrical nanowires (dashed lines). (b) Sputter yield as a function of the impact parameter for a sphere (red), cylinder (blue) and cube (green) with structure sizes of 50 nm for 100 keV Ar^+ irradiation. (c) Gaussian model for modeling the sputter yield as a function of the impact parameter. The curves show different combinations of mean value and standard deviation to reproduce the qualitative trend of the sputter yields. (d) Sputter yield as a function of the impact parameter. The data points are the simulation results shown in (a) for nanoparticle diameters of 10 and 35 nm. The solid lines show Gaussian fits of the Gaussian sputtering model. The parameters of the fits are shown in the figure. The dashed vertical line indicates the rim of the particles.

parameters $b \sim 0.5\,R$ from the center. Here, R is the structure's radius. The sputter yield is increasing for peripheral impacts and reaches a maximum at $\sim 0.9\,R$. The reason is a maximum intersection area of the damage cascade with the surface for peripheral impacts. Because spheres are curved in two directions, while cylinders are curved in only one direction, the intersection area of collision cascade and surface is larger in the case of spheres. This leads to a larger yield in case of spherical nanoparticles compared to the cylindrical nanowires. The curvature has also an intrinsic effect on the sputter yield, since the yield strongly depends on the angle of incidence (see section2.2). This is discussed in detail in references [75, 76]. *iradina* simulations have also been performed for a cubic geometry as a function of the impact parameter, shown figure 4.4b for 100 keV Ar^+ ions, to underline the influence of a curved geometry on the sputter yield. The radii of nanoparticle and nanowire, as well as the edge length of the cube were 50 nm. The results for nanowire and nanoparticle geometry are similar to the previously shown simulations. The cubic geometry, however, shows a different result. The sputter yield of the cube is almost constant, unless the ion impacts near the rim at a distance of 24 nm from the center ($b \approx 1$). This is a result of the absence of any curvature in the cube. The results discussed above and shown in figure 4.4 are in line with the simulations obtained by Nietiadi *et al.* [140] and Urbassek *et al.* [76].

The MD simulation results were also analyzed regarding the sputter yield dependence of the impact point as a function of the nanoparticle diameter (not shown here). Large variations of the data points of the sputter yields for most particle diameters were observed. Additionaly, the statistical errors were large for most impact parameters and in some cases most data had to be interpreted as almost constant, no clear trend could have been observed. The reason was an insufficient number of simulations for a wide range of impact parameters for a proper statistic. Some particle sizes had cumulative impacts on the center and the rim with just a few impacts in between, even for 100 simulated impacts. Therefore, the results from the *iradina* simulations could not be verified by the MD simulations, yet.

A simple analytic model for describing the trend of the sputter yield as a function of the impact parameter should be outlined briefly here. Let's reconsider equation 2.8 from section 2.2. An ion hits a nanoparticle with radius R. The damage distribution $F(r, r_0)$ was assumed to be a Gaussian distribution in all three dimensions with $\mu = (\mu_x, \mu_y, \mu_z)$ and $\sigma = (\sigma_x, \sigma_y, \sigma_z)$. The sputter yield is proportional to the intersection area between nanoparticle surface and damage cascade. As demonstrated in this section, the sputter yield strongly depends on the ratio of ion range versus nanoparticle diameter and therefore on how the damage cascade fills the nanoparticle volume. The sputtered atoms will then have also a Gaussian distribution as a function of the impact parameter b, $G(b, \mu^*(\mu(r_0), R), \sigma^*(\mu(r_0), R, \sigma))$, where $\mu^*(\mu(r_0), R)$ is the mean value and $\sigma^*(\mu(r_0), R, \sigma)$ is the standard deviation of the distribution. Note, that the new distribution depends on the parameters of the original damage distribution, the nanoparticle size and the impact parameter. The function is symmetric in direction of b, because impacts with b and $-b$ are equivalent. The Gaussian functions

$$g(b, \mu^*, \sigma^*) = G(b, \mu^*, \sigma^*) + G(b, -\mu^*, \sigma^*) \tag{4.1}$$

are plotted in figure 4.4c for different parameters, which corresponds to the sputter yield as a function of the impact parameter. The parameters were chosen in a way that the curves reproduce the trend of the sputter yields for different nanoparticle sizes shown in figure 4.4a. Large mean values and small standard deviations lead to a trend similar to the one sputtering of large nanoparticles in figure 4.4a, while small mean values and large standard deviations reproduce the trend of the sputter yield as a function of the impact parameter for small nanoparticles. A function $g(x, A, m, s) = A \cdot (G(x, m, s) + G(x, -m, s))$, where $G(x, m, s)$ and $G(x, -m, s)$ are Gaussians similiar to equation 4.1 and A is a parameter similar to Λ in equation 2.8, is fitted to the simulated data shown in figure 4.4a. The simulation results and fits for nanoparticle diameters of 10 and 35 nm are shown in figure 4.4d. The model fits the data perfectly. The sputtering behavior for ion impacts from center to rim can therefore be explained by the Gaussian distribution of the intersection area of a Gaussian damage distribution with the nanostructure's surface.

4.3 Angular distribution of sputtered atoms

The angular distributions of sputtered atoms were extracted from both MC and MD simulations for random impacts of 25 keV Ga^+ ions into spherical Au nanoparticles. A schematic of an ion impact on a spherical nanoparticle is shown in figure 4.5a, where the azimuthal angle φ and polar angle Θ are depicted. A representative angular distribution of sputtered atoms obtained by *iradina* is shown in figure 4.5b. The number of sputtered atoms is plotted as a function of azimuthal and polar angle. A polar angle of $\Theta = 0$ points in antiparallel direction of the ion beam, while the ion travels in direction of $\Theta = \pi$. The azimuthal angle defines the direction in the plane perpendicular to the ion beam direction. The distribution shows a symmetry in azimuthal direction, as the sputtered atoms prefer a certain direction perpendicular to the ion beam in polar direction ($\Theta \approx \pi/2$). The symmetry in azimuthal direction was observed in *iradina* as well as in MD simulations. Therefore, only the distributions in polar direction are discussed in the following.

The polar angles were averaged over all azimuthal angles. Figure 4.5c shows the the normalized sputter yield as a function of the polar angle obtained by *iradina* for different nanoparticle diameters and bulk, while figure 4.5d shows the results from the MD simulations only for nanoparticles. The data are normalized to the maximum of the respective distribution in order to make the results by different simulation methods comparable, as the qualitative characteristics are of interest for the further discussions in this thesis.

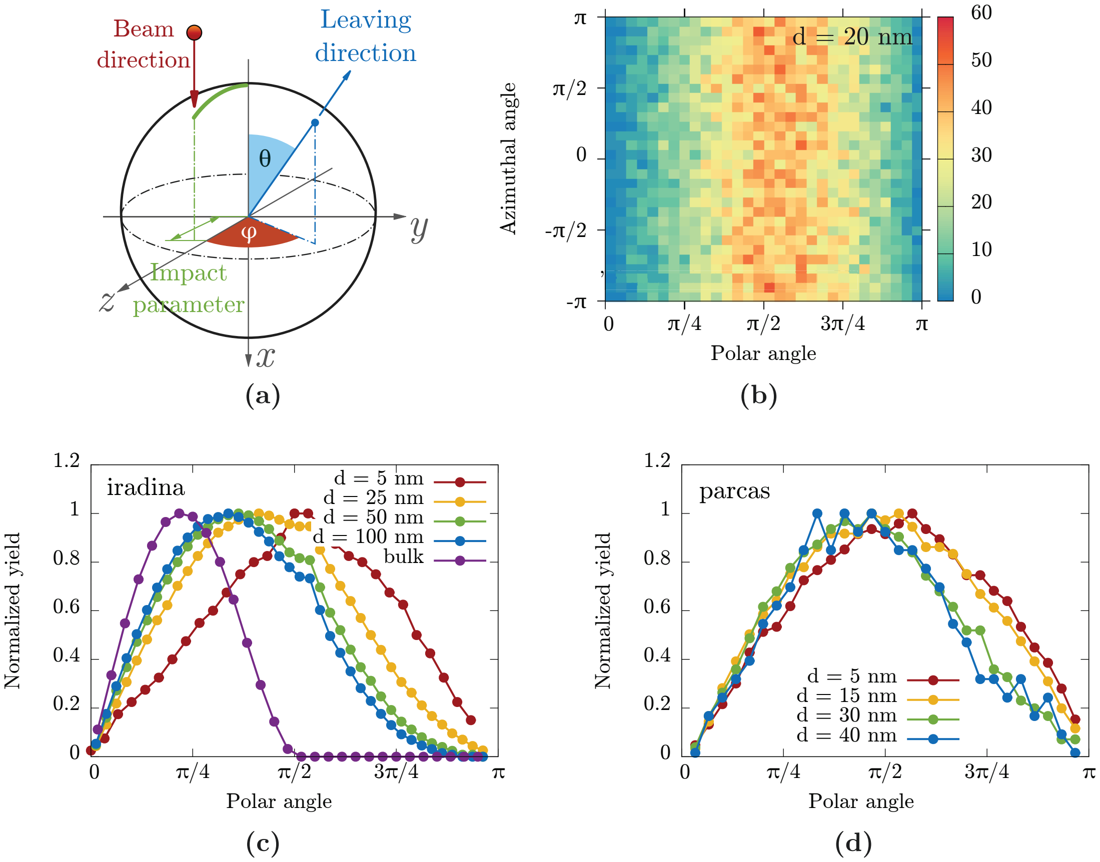

Figure 4.5: (a) Schematic drawing of the ion impact on a spherical nanoparticle. The azimuthal angle φ is drawn in red, while the polar angle Θ is drawn in blue. (b) With *iradina* simulated angular distribution of sputtered atoms after 10 000 random 25 keV Ga^+ ion impacts on a spherical nanoparticle with a diameter of 20 nm. The distribution is symmetric in azimuthal direction. (c) – (d) Average polar angle distributions of sputtered atoms from an ion irradiated spherical nanoparticles obtained by (c) *iradina* and (d) *parcas* for different nanoparticle diameters. The polar angles were averaged over all azimuthal angles. The *iradina* simulated angular distribution of sputtered atoms for the bulk situation for normal incidence is shown in (c).

The directions of the sputtered atoms from the nanoparticle with a diameter of 5 nm are distributed almost over all polar angles, as shown in figure 4.5c and 4.5d. However, only very few atoms are sputtered in backward direction (opposite beam direction) as a result of the transferred momentum in forward direction. This is the case for all diameters as well as for the sputtered atoms from bulk. The maximum of the distributions of the 5 nm sized nanoparticles is almost at a polar angle of $^{\pi}/_{2}$ for both MC and MD simulations. The maximum of the distributions is shifting towards smaller polar angles with increasing nanoparticle diameter. The simulated bulk distribution shows a maximum at a polar angle of $\sim {}^{\pi}/_{4}$. The width of the bulk distribution is smaller because sputtered atoms can only be emitted in the upper half-space. The widths of the distributions of the nanoparticles decreases slightly with increasing nanoparticle diameter for the MC simulation (figure 4.5c). This effect is more pronounced in the results obtained by MD simulations (figure 4.5d), although the size difference in case of MD simulations is not as big as in the case of the MC simulations. The reason for the shift of the distribution maxima and the decrease in width is the decreasing curvature with increasing nanoparticle size, where the nanoparticle situation approaches gradually the bulk situation. Therefore, the boundary value of the distribution maxima of the nanoparticle distributions would be the bulk value, as depicted in figure 4.5c. Another observation can be made at polar angles between $^{\pi}/_{2}$ and $^{3\pi}/_{4}$ in the MC results, as an asymmetry is apparent for nanoparticles with diameters larger than 25 nm in figure 4.5c. The amount of material inside the nanoparticles increases with increasing diameter. Therefore, the probability of the emission of atoms in beam direction decreases, even at peripheral ion impacts, due to the low ion range of 25 keV Ga^+ in Au (6.7 nm). This asymmetry is not visible in the MD angular distribution due to the relatively small number of simulations. Addiationally, the angular distributions obtained by *iradina* show a shoulder between $^{\pi}/_{2}$ and $^{3\pi}/_{4}$. This is most likely a simulation artifact, because it was also observed in simulation results using other projectile, target and energy combinations.

The polar angle distributions of the sputtered atoms from *iradina* and *parcas* are comparable in width and maxima positions. The *iradina* simulations are smoother due to a better statistic (10 000 simulated ions in *iradina* versus 100 simulated ion impacts in *parcas* for the simulations shown in figure 4.5). However, both simulations deliver almost the same results. Because calculations with *iradina* were faster, simulations were performed for nanoparticle sizes ranging from 1 to 100 nm in steps of 1 nm to use the angular distributions of the sputtered as input parameters for the MC redeposition algorithm presented in chapter 6.

4.4 Temperature after ion impact

MD simulations offer the possibility to investigate the temperature development inside nanoparticles after an ion impact. Therefore, the data of MD simulations were analyzed with respect to the temperature. The kinetic energies of each atom was calculated from the velocity vector, while the temperature then was calculated using $T = {}^{E}/_{k_B}$. The analyzed nanoparticles were freestanding and not fixed.

Figure 4.6a shows the evolution of the mean temperature of three different nanoparticle sizes over time. The data for each shown particle size is the average over all 100 performed simulations. Two different data sets are shown for each particle size in figure 4.6a: (1) The mean temperature of all atoms of the particle, which includes the atoms inside the nanoparticle as well as sputtered atoms, which is indicated as "all" and (2) the mean temperatures of the remaining atoms inside the nanoparticles, indicated as "inside". The initial temperature in all cases was 300 K at a time $t = 0$ ps before the ion impact. The

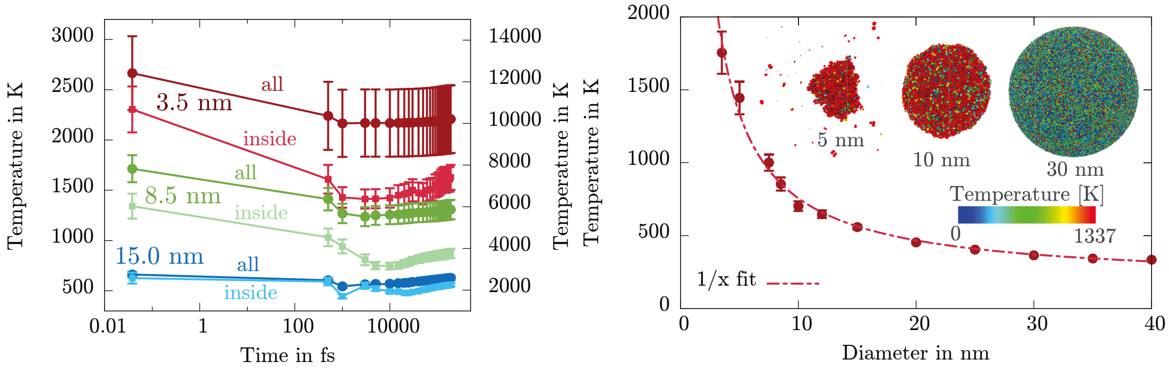

(a) (b)

Figure 4.6: (a) Temperature as a function of time for spherical Au nanoparticles with different diameters irradiated with 25 keV Ga$^+$ ions. The diameters are indicated with the respective colors in the figure. The initial temperature of all nanoparticles was ~ 300 K. Two kinds of temperatures are plotted: The lines indicated with "all" (darker colors) represent the average temperature of all atoms, which also contain the sputtered atoms, while lines indicated with "inside" (light colors) represent the average temperature of the atoms remaining inside the nanoparticle. The right y axis shows the scale for the average temperatures for "all" atoms of the 3.5 nm nanoparticles. (b) Simulated temperature after 200 ps as a function of the nanoparticle diameter. The data shows the temperature at the end of the simulated time period of 200 ps. The dashed red line shows the fit of the data points with a function $f(x) = {}^{a}\!/_{x} + b$. The image insets show representative images of three nanoparticles with different diameters after irradiation after 200 ps. The atoms in the nanoparticles shown in red have a temperature equal or larger than the melting temperature of Au of 1337 K.

temperature increases significantly in all shown cases after the first time interval of 0.04 fs and decreases with progressing time due to sputtering and evaporation. Nevertheless, the temperature of small particles remains on a significantly elevated level. In some cases the mean temperature of the atoms seems to increase after 10 ps, especially the data sets which represent the atoms inside the nanoparticle. A possible explanation might be the minimization of the surface energy. An object tends to minimize it's surface energy, if it's heated up to or above the melting point, by forming a spherical surface. A molten nanoparticle, which is deformed after the ion impact, is trying to regain a spherical shape and releasing energy. This energy is transferred completely to the atoms inside the nanoparticle, since radiation loss was not implemented. This effect is more pronounced for small nanoparticles, because the deformation by the ion impacts is more dramatic (see inset of figure 4.6b). Additionally, the number of atoms, which gain the released energy, is smaller for small nanoparticles. Another effect, which contributes to the slight heating of the nanoparticles after > 10 ps, might be the fact that hot, sputtered atoms are redeposited on the nanoparticle. This was already reported in reference [34]. The difference in temperature between the lines indicated with "all" and "inside" shows how much energy the particles lose due to sputtering and evaporation of energetic atoms. Most obvious is the difference between the cases "all" and "inside" the nanoparticle for the nanoparticle with a diameter of 3.5 nm. The mean temperature of all atoms in the simulated system is approximately 10 000 K, while the temperature of the remaining nanoparticle is still ∼ 1 700 K. This can be explained by the ratio of sputtered atoms from a nanoparticle versus the total number of atoms in a nanoparticle. This ratio is larger for small nanoparticles. Therefore, small nanoparticles lose more energy due to sputtering than large nanoparticles. However, the temperature is still twice the melting temperature of Au of 1337 K.

If the temperatures of the nanoparticles with different sizes are compared to each other, the data reveals that the temperature decreases with increasing nanoparticle size. This can be explained by the fact that the energy transferred from the ion to the nanoparticle is distributed over a larger number of atoms in case of a larger nanoparticle, which results in a smaller mean temperature. The temperature of the nanoparticles at the end of the simulation after 200 ps is plotted over the diameter of the nanoparticles in figure 4.6b to underline this fact. The temperature decreases inversely proportional with the diameter, as the fit in figure 4.6b shows. The data is fitted with a function $f(x) = {}^{a}/_{x} + b$ with the parameters $a = 5277.0 \pm 187.6$ and $b = 178.2 \pm 23.1$. Parameter a is a parameter which scales the curve in units K·m. This parameter depends on the ion species and energy and the target material. Parameter b is a measure for the temperature for bulk geometry after the ion impact after 200 ps in K. Parameter b is expected to be room temperature, however the number of data points is too small to make the fit more accurate. The inset of figure 4.6b shows the images of representative nanoparticles with an initial diameter of 5, 10 and 30 nm after 200 ps after the ion impact. The nanoparticles with a diameter of 5 nm are completely molten and deformed. The depicted 5 nm nanoparticle also continues to evaporate hot atoms, visible as satellites around the nanoparticle. The shown nanoparticle with a diameter of 10 nm shows also a large number of hot atoms above the melting point, but the mean temperature is below the melting point, as some colder atoms in green and blue color indicate. The nanoparticle already recovered it's spherical shape. The 30 nm sized particle shows just a few very hot atoms, on average the atoms already relaxed almost to room temperature.

The evolution of the temperature over time of Au nanoparticles after an ion impact is shown in figure 4.7 as images of nanoparticles with diameters of 15 nm (4.7a) and 30 nm (4.7b) at different time steps. Two representative nanoparticles, which, after 200 ps, have a temperature near the average temperature of all simulated nanoparticles of the same size, were chosen for these images. The nanoparticles have equal temperatures before the ion impact. After 502.6 fs it becomes apparent that the ion energy is transferred to atoms near the impact point. A relatively larger volume fraction of the 15 nm sized nanoparticle is affect by the ion induced local heating due to the smaller number of atoms compared to the 30 nm sized nanoparticle. The small particle is heated to an average temperature of 890 K at this time, while the large nanoparticle is only heated to 378 K. The heated atoms are distributed completely over the whole volume after 15 ps in case of the 15 nm

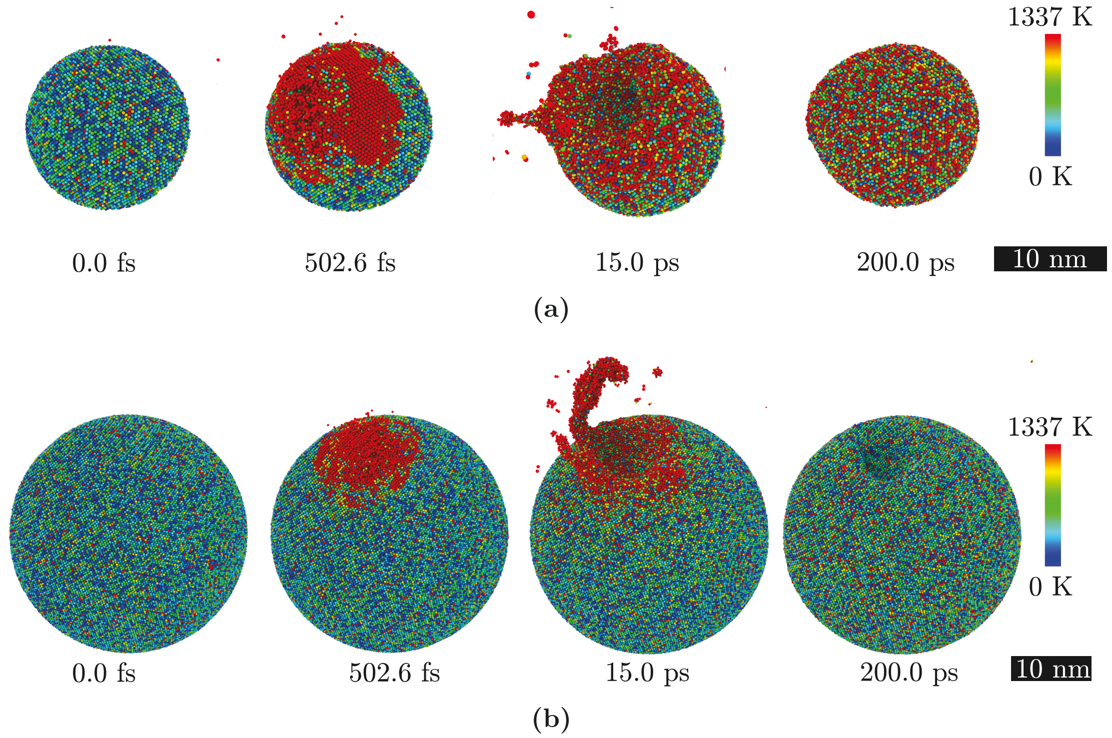

Figure 4.7: Images of an ion impact of a 25 keV Ga^+ ion on a Au nanoparticle with a diameter of (a) 15 nm and (b) 30 nm at different times after the ion impact. The color codes the temperature, where the the maximum temperature of atoms can exceed the maximum of the scale of 1337 K. The scale bar is shown on the bottom right of the respective figures.

sized nanoparticle. Additionally, material is ejected from the part, which was heated most before, shown in figure 4.7a. The temperature of the atoms inside the 15 nm sized nanoparticle is 737 K after 15 ps. In contrast, the 30 nm sized nanoparticle is still heated locally, but also ejects molten material explosively after 15 ps as a large cluster of some hundred atoms, as shown in figure 4.7b. The temperature of the large nanoparticle at this stage of the simulation is 356 K. After 200 ps, the 15 nm sized nanoparticle shows a smooth surface again, but has not returned to a full spherical shape yet. It remains at an elevated temperature of around 600 K. The nanoparticle with a diameter of 30 nm shows a temperature slightly above room temperature after 200 ps. Furthermore, a crater remains at the position where the ion impinged and the hot material expelled, because the energy and therefore the mobility of the atoms in the particle was too low to regain a smooth surface. The reason for the difference for both nanoparticle sizes can be summarized by the different amount of energy transferred from the ion to the individual target atoms. If the temperature difference between room temperature and the final temperature of the nanoparticles is considered and $E = k_B \cdot T$ is used for calculation, the transferred energy is $0.05\,{}^{\mathrm{eV}}/_{\mathrm{atom}}$ and $0.007\,{}^{\mathrm{eV}}/_{\mathrm{atom}}$ for the 15 nm and 30 nm sized nanoparticle, respectively. The previous discussion showed that nanoparticles, especially with diameters below 20 nm, can be heated up to the melting point by a single ion impact. The elevated temperature remains if the energy loss due to thermal conduction and radiation is low. In case of a consecutive ion impact on a heated nanoparticle, the nanoparticle would easily evaporate. In case of particles with diameters larger than 20 nm consecutive ion impacts would not lead to evaporation, but a deformed surface will remain. Craters and deformations do not smooth with increasing time.

4.5 Summary

The sputter yield as a function of ion energy and nanostructure diameter was investigated using the MC code *iradina* for Ar^+ and Ga^+ ions and spherical, cylindrical and bulk geometry, as shown in section 4.2. Additionaly, MD simulations were performed using the code *parcas* to investigate the diameter dependence of the sputter yield of 25 keV Ga^+ irradiated spherical nanoparticles. The sputter yield as a function of ion energy and nanoparticle diameter revealed a maximum where the ion range matched the nanostructure's size for both MC and MD simulation results. The spherical nanostructure showed a larger sputter yield than the cylindrical nanostructure in all cases. However, the sputter yields of both nanogeometries were significantly larger than the sputter yield for bulk. The sputter yield was also investigated as a function of the impact parameter with respect to the nanostructure radius, where impacts on the nanostructure's rim lead to larger sputter yields compared to central impacts. All these observations can be explained by the fact that the sputter yield is proportional to the intersection of the damage cascade with the target's surface. The cascade-surface intersection increases with the curvature of the structure [75, 76], which explains the larger sputter yield of spheres compared to cylinders, as well as the small sputter yields of bulk compared to nanostructures.

The angular distributions of sputtered atoms for random 25 keV Ga^+ ion impacts on spherical Au nanoparticles of different sizes was presented in section 4.3. The emission of sputtered atoms was isotropic in azimuthal direction (perpendicular to the ion beam), while it depends on the nanoparticle's size in polar direction. The polar angle distribution of the sputtered atoms converges to the bulk distribution with increasing nanoparticle size. Both MC and MD simulations showed comparable results.

The temperature of spherical Au nanoparticles after 25 keV Ga^+ ion impacts was investigated as a function of the nanoparticle diameter using the MD simulation results and was presented in section 4.4. The temperature after 200 ps after the ion impact increased above the melting point for nanoparticles with a diameter smaller than 10 nm and some small nanoparticles evaporated after a single ion impact. The temperature after 200 ps after the ion impact decreased with increasing nanoparticle diameter, because the transferred energy from the ion is distributed over a larger number of atoms in large nanoparticles compared to smaller nanoparticles.

5 Sputter yields of Au nanoparticles

This chapter presents the size and energy dependence of the sputter yield of Au nanoparticles, investigated by high resolution SEM. The interaction between nanoparticle and substrate was investigated in detail using various experimental techniques. Sputter yields measured from Au nanoparticle arrays, shown in section 5.1, were obtained in collaboration with the group of Claudia Pacholski at the Max Planck Institute (MPI) for Intelligent Systems in Stuttgart and the Institute for Physical Chemistry at the University of Heidelberg. Parts of the results were published in reference [137]. The *in situ* experiments shown in section 5.2 were performed in collaboration Julia Graupner in the scope of her Seminarfacharbeit. They were presented at the German "Jugend Forscht Bundeswettbewerb" 2016. The RBS experiments depicted in section 5.3 were performed in collaboration with Jura Rensberg.

5.1 Array measurements

Experimental details Samples with hexagonally ordered spherical Au nanoparticles on a Si substrate were irradiated with Ar^+ and Ga^+ ions in order to investigate the size and energy dependence of the sputter yield. The Ar^+ irradiation was performed using the linear ion implanter ROMEO. The Ga^+ irradiation was performed using the FEI Helios i600 Nano Lab FIB system. The ion energies of the Ar^+ and Ga^+ ions were varied in the ranges of 20 to 350 keV and 1 to 30 keV, respectively, and the ion fluence was kept constant to determine the energy dependence of the sputter yield. From the simulations performed with *iradina*, presented in section 4.2, the ion fluence was estimated to be $3 \cdot 10^{15}\,{}^{\mathrm{ions}}/_{\mathrm{cm}^2}$ to achieve a measurable diameter decrease of the particles of more than 2 nm, which is significantly larger than the resolution of the used SEM. The ion beam current was kept constant at low values of $0.5\,\mu$A and $0.1\,\mu$A for both Ar^+ and Ga^+ irradiation, respectively. The diameter dependence was investigated with 95 keV Ar^+ and 25 keV Ga^+ ions of both constant ion energy and ion fluence. The used ion fluences were $2 \cdot 10^{15}\,{}^{\mathrm{ions}}/_{\mathrm{cm}^2}$ for Ar^+ ions and $3 \cdot 10^{15}\,{}^{\mathrm{ions}}/_{\mathrm{cm}^2}$ for Ga^+ ions.

High resolution SEM images were obtained using the FIB dual beam system before and after irradiation. The position on the sample for image acquisition was marked using the Ga beam of the FIB before irradiation in order to find the exact same position and set of nanoparticles after irradiation again. The number of nanoparticles evaluated per

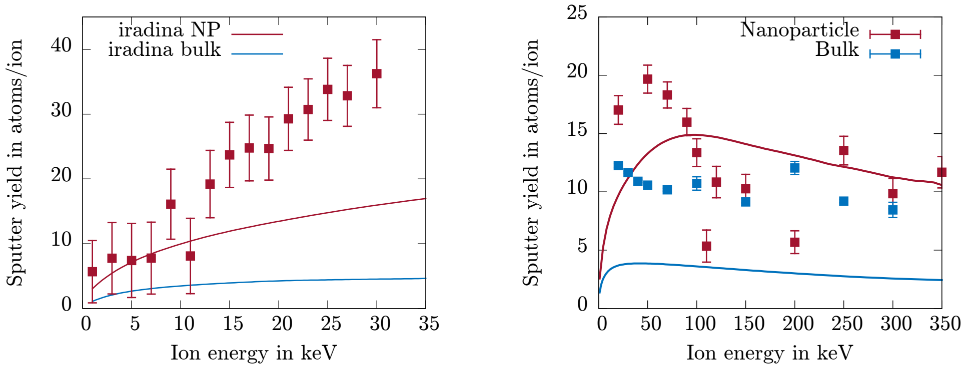

(a) **(b)**

Figure 5.1: Sputter yield as a function of the ion energy for spherical Au nanoparticles with an average diameter of 50 nm for (a) Ga$^+$ and (b) Ar$^+$ ions irradiation. The results for bulk geometry are shown in blue and for spherical nanonanoparticles in red, respectively. The data points show the experimentally obtained results, while solid lines show simulation results obtained with *iradina*. The error bars on the data points show the statistical errors of the mean values for respective energies. The experimentally obtained results for Ar$^+$ irradiation shows a large variation for ion energies larger than 100 keV.

sample was up to 3 500. The images were evaluated as described in section 3.3 using *imageJ*. The threshold circularity was set to 0.3, the grey value threshold was set to 150 for the Ar$^+$ irradiation and 120 for the Ga$^+$ irradiation. For each ion energy the averaged sputter yield over all nanoparticles on a pair of images was calculated to respectively investigate the energy dependence of the sputter yield. The diameter dependence of the sputter yield was determined by comparing each nanoparticle on the images before and after irradiation individually, utilizing the broad size distribution of the nanoparticles on the sample. The images taken at the same position of a pristine and irradiated sample were brought in coverage to compare the size of the nanoparticles.

Energy dependence of the sputter yield Figure 5.1a shows the *iradina* simulation results and experimentally obtained sputter yields for Ga$^+$ irradiation of Au nanoparticle arrays as well as for bulk geometry as a function of ion energy. The simulation results were already discussed in section 4.2. Both experimental and simulation results are comparable for ion energies up to 7 keV. The experimental sputter yields are larger than the simulation results for ion energies larger than 12 keV. However, the trend derived from simulations is followed by the experimental results. At an ion energy of 30 keV, the experimentally obtained sputter yield is about 2 times larger than the simulation value calculated by *iradina*.

The experimentally obtained sputter yields and the respective *iradina* simulation results for Ar$^+$ irradiation as a function of the ion energy are shown in figure 5.1b for nanoparticle and bulk geometry, respectively. The experimental results for bulk were obtained by irradiating thin Au layers on Si substrates with Ar$^+$ ions of different energies and

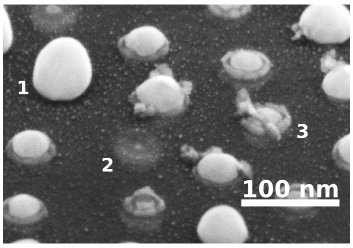

Figure 5.2: Representative SEM image of a Au nanoparticle array irradiated with $3 \cdot 10^{15}$ ions/cm^2 110 keV Ar$^+$ ions taken under an angle of 52°. Various effects on the nanoparticles are visible: particle 1 seems not to have changed its shape, while particle 2 disappeared. Particle 3 changed its shape dramatically. Other particles around the marked particles seemed to be sunk into the substrate.

measuring the film thickness using RBS, which is described in detail in section 5.3. All experimentally obtained sputter yields are higher compared to the bulk simulation for Ar$^+$ irradiation. The experimental values of the irradiation of nanoparticles follow the same trend as the simulation values, although the maximum of the experimental values is slightly shifted towards energies of ~ 50 keV compared to the simulation at ~ 100 keV. For ion energies larger than 100 keV, the experimental sputter yields deviate strongly from each other. The smallest experimental sputter yield is measured for an ion energy of 110 keV. Only above an ion energy of 250 keV the variation decreases and the experimental values are approaching the simulated sputter yields for nanoparticles again. Comparing the experimental results of bulk and nano geometry, an enhancement of the nanoparticle geometry compared to bulk is clearly visible for most ion energies, which is in line with the theory described in section 2.2. Some nanoparticle data points are below their bulk counterparts, which is due to the variation of these results.

The reasons for the discrepancies between experiment and simulation are diverse. First of all, the assumptions of the MC method are fairly simple. A freestanding nanoparticle is assumed in the simulation, while various particle-substrate interactions occur in the experiment (see also section 5.3), which are neglected in the simulation. The BCA is a good approximation for describing damage cascades, but it diminishes the sputter yield as demonstrated in section 4.2. Furthermore, thermally driven effects are excluded due to BCA and statistical representation of average atom positions in the target. But as shown in the literature [34, 141] and later in this work, thermally driven effects play a key role in the sputtering process.

The large variation of the experimental data points for Ar$^+$ ion energies larger than 100 keV and the steep decline of the sputter yield for an ion energy of 110 keV can be understood by taking a closer look at SEM images of the samples. A representative SEM image of a sample after 110 keV Ar$^+$ irradiation is shown in figure 5.2. Small dots can be seen around the particles, which are most likely tiny Au clusters sputtered in forward direction from the nanoparticles and deposited on the substrate. Furthermore, nanoparticles on the sample react differently to the ion bombardment. Three particles are marked in the image. Particle 1 seems not having changed its shape at all, in comparison to pristine nanoparticles (figure 3.3a, section 3.1). In contrast, particle 2 vanished completely. Most other particles, like particle 3, changed their shape dramatically. Also, many particles sank into the substrate (compare with section 5.3). The deformation and vanishing of

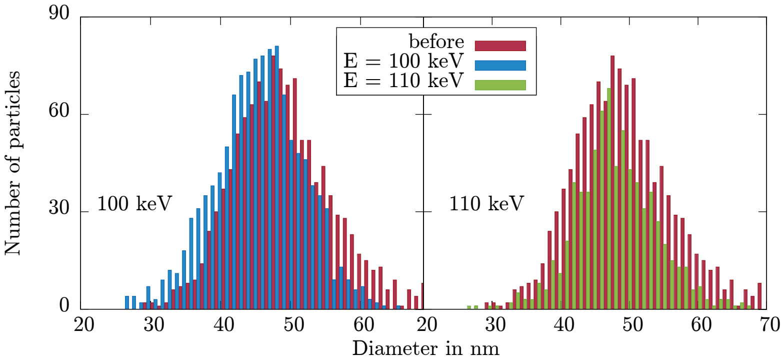

Figure 5.3: Size distributions of nanoparticles before (red) and after irradiation for Ar^+ ion energies of 100 keV (blue, left hand side) and 110 keV (green, right hand side). The mean diameter of the particles shows a significant shift to smaller diameters after irradiation for ion energies of 100 keV. The shift as well as the total number of evaluated nanoparticles is smaller for 110 keV Ar^+ irradiation.

nanoparticles is attributed to thermally driven effects, that were already described in section 4.4. Nanoparticles have a high surface-to-volume ratio and a small volume. Also, the thermal contact and conductivity between Au nanoparticles and Si substrate is weak. The situation should be illustrated with a simple calculation. Let's assume an ion with an energy of 100 keV, which is transferred completely as thermal energy to a nanoparticle with a diameter of 30 nm. The number of atoms is roughly $8 \cdot 10^5$ atoms. This leads to an energy transfer of about 0.1 eV/atom. If thermal losses like radiation, evaporation and heat conduction are neglected, according to $E = k_B \cdot T$ this would lead to a temperature increase of $\sim 1000\,°\mathrm{C}$. This argument is also supported by MD simulation results shown in section 4.4. Another indication for thermally driven effects are the so-called fingers or fringes, which are noticeable on particle 3 in figure 5.2. These structures arise due to ejection of molten material, which has been shown for bulk irradiation by Nordlund *et al.* [141] and appeared also in the MD simulations shown in section 4.4.

Small particles are more affected by the introduced thermal energy, as MD simulations (see section 4.2) and experiments show. The diameter distributions of the analyzed particles before and after 100 keV and 110 keV Ar^+ irradiation are shown in figure 5.3. The Gaussian shape of the distribution is conserved in both cases. Also, in both cases the mean diameter shifts slightly to smaller values. However, the number of particles with a diameter smaller than 40 nm after irradiation is larger in the statistic of the experiment with 100 keV ions compared to the one with 110 keV ions. Thus, the mean diameter after 100 kev Ar^+ irradiation is smaller than the mean diameter after 110 keV Ar^+ irradiation. Although the mean diameter of the nanoparticle distribution is shifted to a smaller diameter, the number of small particles is systematically decreasing. Small nanoparticles, that have vanished or have been deformed, are not counted by *imageJ* analysis. Therefore, the experimental sputter yield is underestimated. The deformation of nanoparticles is a statistical effect, therefore not all particles irradiated with ion energies between 110 and 250 keV are affected in the same way. The mean particle diameter decreases, which results in a decreased sputter yield. More small particles survive for ion energies larger than 200 keV. The higher rate of survival of the smaller particles for higher ion energies is due to the larger ion range in the material. The ions traverse small particles at higher ion energies without depositing the most part of their energies inside the particle. According to *SRIM*, a 250 keV Ar^+ ion has a projected range of 74 nm in Au. Thus, most particles with a diameter smaller than 50 nm will be traversed by the ions and therefore the measured sputter yield increases again.

Another possible explanation for the large variation of the sputter yields for different energies is given by the fact, that for all experiments the same ion beam current was used. The same ion beam current at different ion energies leads to different input powers (ion energy × ion flux) at the target during irradiation. This leads to a systematic variation of the results due to global heating of the samples at high ion energies.

Size dependence of the sputter yield Figure 5.4a shows the sputter yield of 95 keV Ar^+ irradiated individual Au nanoparticles as a function of particle diameter. A large spread of the sputter yields of individual nanoparticles is noticeable. At a diameter of 39 nm, for example, the measured sputter yields vary between 1 and 30 atoms/ion. No crucial deformation effects have been observed on those samples and most of the small particles were still present on the substrate. A possible explanation for this dramatic deviation is given by Greaves *et al.* [34]. The sputter yield strongly depends on the lattice orientation of the nanoparticle towards the ion beam. If the ion impinges in channeling direction, it will deposit only a small amount of its energy. In contrast, an impact in random direction results in a much higher sputter yield. Because the nanoparticles are spin-coated onto the substrate, their orientation is randomly distributed towards the ion beam. The variation of single particle sputter yields was also observable in the experiment using 25 keV Ga^+ ions, as shown in figure 5.4b. However, the variation of the sputter yields for single nanoparticles is much less pronounced here. One reason could be the smaller ion range of Ga^+ ions in Au compared to the nanoparticle sizes. According to *SRIM*, 95 keV Ar^+ ions have a mean range of 29 nm in Au, which almost matches the size with maximum sputter yield. In contrast, 25 keV Ga^+ ions only have an ion range of 6.7 nm in Au. Therefore, the ion-solid interaction is taking place mainly in the upper hemisphere of the particles facing the ion beam and deformation effects and effects due to channeling are less pronounced with 25 keV Ga^+ ions.

The dark red data points in figure 5.4 show the averaged sputter yields for size intervals of 1 nm in width. The averaged data points for Ar^+ irradiation in figure 5.4a do not match the simulation results. For particle sizes larger than 45 nm, the average sputter yield increases and reaches a yield which is a factor of 3 above the value of the *iradina* nanoparticle simulation. This behavior was also observed for other Ar^+ ion energies (not

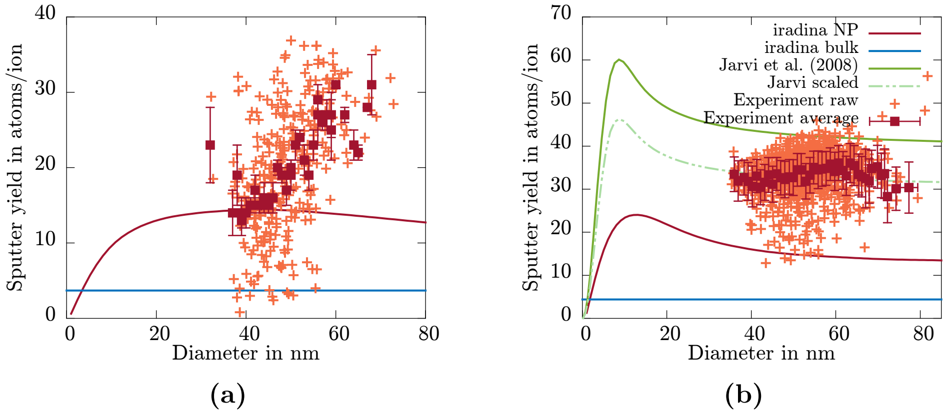

(a) (b)

Figure 5.4: Size dependence of the sputter yield for ion irradiated Au nanoparticles (a) with 95 keV Ar^+ ions and (b) with 25 keV Ga^+ ions. The solid lines represent the simulation results obtained with *iradina* for bulk (blue) and nanoparticle (red) geometry. The light orange crosses represent the results for single nanoparticles. The dark red squares show the average sputter yield over an interval size of 1 nm. The solid green line in (b) shows the model by Järvi *et al.* [51]. The dashed light green line is the Järvi model sclaed by a factor of 0.77 to fit the experimental data. The color coding is the same for both figures as shown in the legend in (b).

shown here) and can not be explained by models presented in the literature [51, 64]. The increase of sputter yields with increasing particle sizes for Ar^+ might be due to a systematic error in the experiment, which could not been ruled out.

The averaged sputter yields for Ga^+ irradiation presented in figure 5.4b show less variation and smaller statistical errors compared to Ar^+ irradiation. They also follow the trend provided by the *iradina* simulation and the model by Järvi *et al.* [51]. The averaged experimental values are twice as large as *iradina* predicts and are only slightly smaller than the model by Järvi *et al.*. The model is partly based on MD simulations, which have more realistic assumptions compared to *iradina* (see section 2.2). Järvi's model was scaled with a factor of 0.77 in order to fit the experimental data (dashed line in figure 5.4b). In the following this is denoted as "scaled Järvi's model". The curve obtained by *iradina* simulations can also be scaled by a factor of 2.2 to match the averaged experimental sputter yields. But due to a smoother slope and more data points, Järvi's model will be used for sputter yield calculations in chapter 6.

The presented experiments reveal the limitations of the used MC code. It is capable of a qualitative prediction of sputtering yields, but underestimates it most likely due to the neglection of thermally driven effects. The model presented by Järvi *et al.* is in better agreement for the sputter yields obtained by the Ga^+ irradiation, because it takes thermally driven effects into account since it is partially based on MD simulation results.

Another critical parameter in the MC code is the SBE. Figure 5.5 shows the *iradina* simulation for 25 keV Ga^+ irradiation of Au nanoparticles with a diameter of 50 nm for different SBEs. The sputter yield increases as the SBE decreases , of course. Nevertheless, even at unrealistically low SBE values of 0.1 eV the simulated sputter yield does not

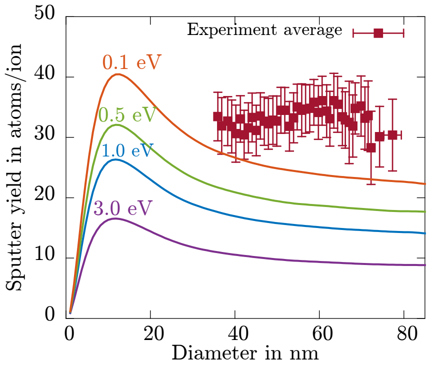

Figure 5.5: *iradina* simulation for 25 keV Ga$^+$ irradiation of spherical Au nanoparticles. The results arre shown for various SBE settings in the simulation as solid lines. The data points show the averaged experimental sputter yields.

match the experimentally obtained sputter yields. It should be mentioned, that *iradina* is not a dynamic code, which means any simulated ion is facing the same target conditions like material density and structure size when hitting the target. This assumption is obviously wrong, since already one ion impact can change the target composition and geometry dramatically, as shown in section 4.2 and references [34, 141, 142]. This has been taken into account in the recently published MC code *TRI3DYN* [46].

5.2 *In situ* measurements

Experimental details *In situ* experiments were performed using a FIB system to investigate the energy and size dependence of the sputter yield of single Au nanoparticle in contrast to array irradiations. Individual Au nanoparticles with an average distance of ~ 480 nm to their neighbors were irradiated with Ga$^+$ ions of various energies ranging from 1 to 30 keV. The initial Au nanoparticle diameters ranged from 40 to 70 nm. The ion beam was defocused in order to prevent large energy deposition on a small area, which would cause an immediate vanishing of the nanoparticles. The irradiated area on the samples was $2 \times 2\,\mu\mathrm{m}^2$. Thus, also the surrounding was affected by ions, but according to the results discussed in chapter 6, this has only a minor influence on the resulting sputter yields of the single nanoparticles with the given interparticle distance. The ion beam current was set to 1 pA to prevent thermally driven effects. The used ion fluence ranged from $5 \cdot 10^{15}\,{}^{\mathrm{ions}}/_{\mathrm{cm}^2}$ to $1 \cdot 10^{16}\,{}^{\mathrm{ions}}/_{\mathrm{cm}^2}$. Images under an angle of 52° were taken in equidistant fluence steps.

The analysis of the samples was carried out using *imageJ* with the method described in section 3.3. The volume of the approximated spheroid was calculated for the Au nanoparticle in every SEM image from the fitted ellipse. Each image corresponds to a certain irradiation step i after a fluence of ϕ_i. The fluence of step i was calculated by

$$\phi_i = \frac{i}{n} \cdot \phi_{total},$$

where ϕ_{total} is the total fluence irradiated on the nanoparticle and n the total number of images taken of the nanoparticle. The sputter yield was calculated by using a best-fit

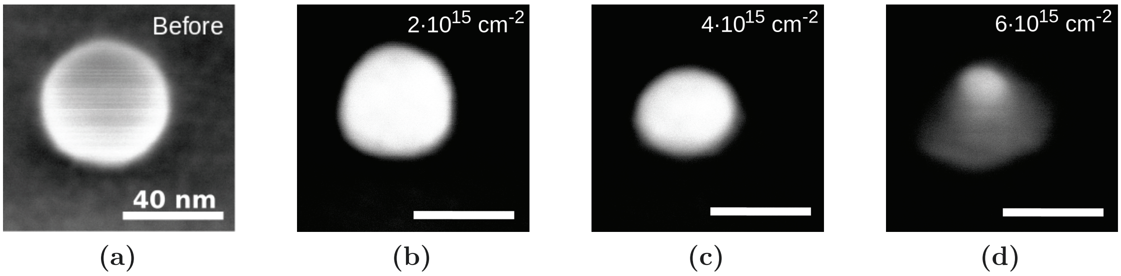

(a) **(b)** **(c)** **(d)**

Figure 5.6: High resolution SEM images of a nanoparticle before (a) and after irradiation with 30 keV Ga$^+$ ions. The fluences were (b) $2 \cdot 10^{15}$ ions/cm², (c) $4 \cdot 10^{15}$ ions/cm² and (d) $6 \cdot 10^{15}$ ions/cm². The images were taken under an angle of 52°. The nanoparticle decreases in size due to sputtering. A flattening due to irradiation is observable in (c). After $6 \cdot 10^{15}$ ions/cm² (d) the particle almost vanished. The scale is the same in all images.

line for four consecutive data points of the volume as a function of fluence as described in section 3.3, in order to reduce large variations and errors of the calculated sputter yield. A hexagonally arranged Au nanoparticle array with an interparticle distance of 50 nm on a Si substrate was irradiated with 30 keV Ga$^+$ ions on an area of $3 \times 3\,\mu\mathrm{m}^2$ with a total fluence of $5 \cdot 10^{15}$ ions/cm² using a FIB system to investigate the sputtering behavior of an ion irradiated Au nanoparticle array as a function of the ion fluence. The ion beam was defocused and a low ion beam current of 1 pA was used. SEM images were taken every $8 \cdot 10^{13}$ ions/cm² during the whole irradiation process under an angle of 52°. The SEM images were evaluated as described in section 3.3.

Energy dependence of the sputter yield In figure 5.6, typical SEM images of a Au nanoparticle in four different irradiation states are shown. The particle shown in figure 5.6a represents a nanoparticle before irradiation. The same nanoparticle is shown after irradiation with $2 \cdot 10^{15}$ ions/cm² (5.6b), $4 \cdot 10^{15}$ ions/cm² (5.6c) and $6 \cdot 10^{15}$ ions/cm² (5.6d) Ga$^+$ ions. The nanoparticle clearly decrease in size with increasing ion fluence. The spherical shape is not conserved, since the nanoparticle flattens with increasing ion fluence, which justifies the assumption of a spheroid shape of the particle for the analysis. A blurred area around the bright nanoparticle is visible in figure 5.6d, which is attributed to Au incorporated into the Si substrate due to ion beam mixing. This behavior is discussed in detail in section 5.3. The sputter yield was only evaluated until intermixing of Au and substrate made particle and substrate indistinguishable. Figure 5.7 shows the nanoparticle volume as a function of ion fluence for three particles irradiated with respective ion energies of 10, 20 and 30 keV. The solid lines show the respective simulation results obtained using *iradina*. The simulated nanoparticle volume dependence on the fluence was calculated by a pseudo-dynamic calculation from the *iradina* results by transforming the result of size-dependence of the sputter yield. The volumes of the nanoparticles decrease for all ion energies. However, the measured volume is decreasing

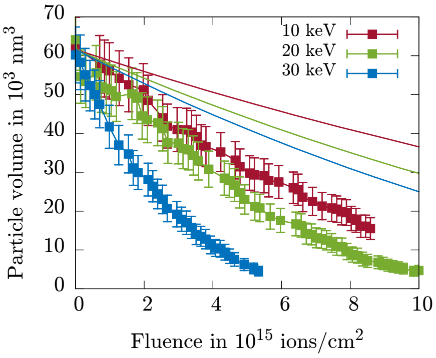

Figure 5.7: Nanoparticle volume as a function of the Ga^+ ion fluence for different ion energies of 10 (red), 20 (green) and 30 keV (blue). The data points show the experimental results from the *in situ* experiment, while the *iradina* simulation results are shown as solid lines. The experimental results show a steeper size decrease of the ion irradiated nanoparticles compared to the simulation. However, the relation between different ion energies is the same for simulation and experiment.

faster with increasing ion energy, which is in line with the simulation and the results from the array experiments.

Size dependence of the sputter yield The sputter yield was calculated from the fluence dependence of the nanoparticle volume. The results are shown in figure 5.8 for Ga^+ ion energies of 10 keV (5.8a) and 30 keV (5.8b) as a function of the particle volume. The sputtering yields could be determined down to small volumes, as visible in figure 5.8a. The trend of the simulations of the volume dependence of the sputter yield could be reproduced, although the maximum of the experimentally obtained sputter yield is shifted towards larger particle volumes compared to the *iradina* simulation. If the nanoparticle volume is below a value of $\sim 5 \cdot 10^3\,\mathrm{nm}^3$, the sputter yield decreases. The nanoparticle is barely visible at large fluences due to particle-substrate-interactions (compare figure 5.6d and also section 5.3 for details) and the nanoparticle volume is seemingly decreasing only slightly between two consecutive irradiation steps. Thus, the measured sputter yield decreases fast for high fluence irradiation. Notice that all experimental sputter yields for 10 keV Ga^+ irradiation are larger than the bulk and nanoparticle geometry simulation. The maximum sputter yield is 43 $^{\mathrm{atoms}}/_{\mathrm{ion}}$ at a particle volume of $3 \cdot 10^3\,\mathrm{nm}^3$. The smallest sputter yield is 20 $^{\mathrm{atoms}}/_{\mathrm{ion}}$ for small particle diameter of $7.5 \cdot 10^2\,\mathrm{nm}^3$, while the sputter yield for nanoparticle diameters larger than $35 \cdot 10^3\,\mathrm{nm}^3$ is around ~ 25 $^{\mathrm{atoms}}/_{\mathrm{ion}}$.
Figure 5.8b shows the sputter yield as a function of the nanoparticle volume for 30 keV Ga^+ ion irradiation. The sputter yield is comparable to the sputter yield for the particle irradiated with 10 keV for large nanoparticle volumes. The sputter yield steeply increases for the observed particle volumes smaller than $10 \cdot 10^3\,\mathrm{nm}^3$ with decreasing particle volume. The maximum sputter yield reaches (170 ± 65) $^{\mathrm{atoms}}/_{\mathrm{ion}}$ (not shown in the graph for reasons of clarity) which is ~ 7 times larger than the maximum of the *iradina* nanoparticle simulation and ~ 4 times larger than the value for the 10 nm sized nanoparticle. The reason for the large difference between the 10 and 30 keV irradiation for nanoparticle diameters smaller than 10 nm is most likely due to differences in the particle-substrate interactions and the resulting difference in image analysis. Such a large difference was also observed between two nanoparticles irradiated with the same ion energy (not shown here). Essential for the sputter yield calculation of small nanoparticle

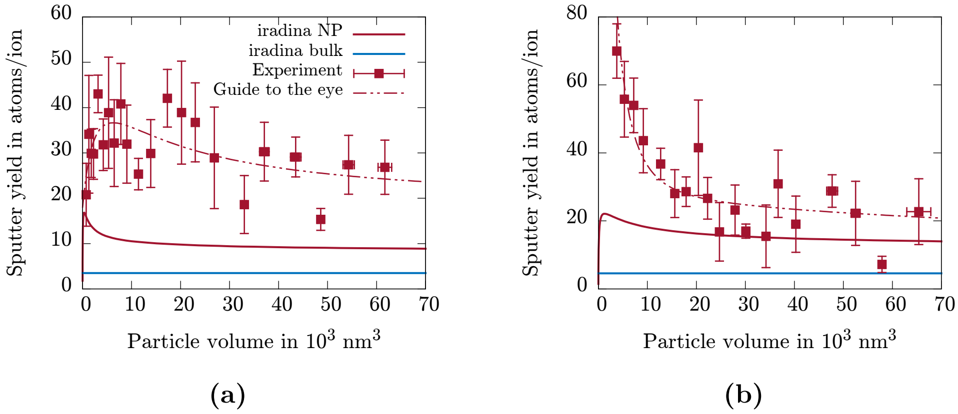

(a)

(b)

Figure 5.8: Sputter yield as a funtion of the nanoparticle volume for Ga^+ irradiation with (a) 10 keV and (b) 30 keV ion energy. The simulation results by *iradina* are shown as solid lines for bulk (blue) and nanoparticle (red) geometry. The data points show the experimental results. The dashed line shows a guide to the eye for the experimental results.

sizes is the level of intermixture of a nanoparticle with the substrate after a certain fluence. For nanoparticle sizes larger than $20 \cdot 10^3\,\mathrm{nm}^3$, the experimental data and the nanoparticle simulation results are in reasonable agreement in all cases (figures 5.8a and 5.8b). The simulated bulk values are again smaller than the experimental data for nanoparticles.

***In situ* experiment with nanoparticle arrays** SEM images of a Au nanoparticle array with an interparticle distance of 50 nm after certain irradiation steps with 30 keV Ga^+ ions are shown in figure 5.9. Figure 5.9a shows the array before irradiation with nanoparticles of different initial sizes. The nanoparticles decrease in size due to sputtering (figure 5.9b – 5.9d), but also the shape of the particles changes with increasing ion fluence. In contrast to the results presented in reference [46], most particles flatten during irradiation and only some nanoparticles obtain a conical shape. This is especially visible at the largest particles in the images. This is due to the fact that sputtering depends on the angle of incidence. The sputter yield is high for ion impacts on the side of the spherical nanoparticles, because the angle of incidence with respect to the surface normal is high compared to central impacts. Möller [46] illustrates the sputter erosion of ion irradiated Au nanoparticle by using the dynamic MC code *TRI3DYN*. The erosion in this literature example is preferentially on the sides of the sphere due to angle dependence and transmission sputtering. This effect is more pronounced at very large nanoparticles, where the deposited ion energy is distributed over a larger number of atoms. Thus, the largest nanoparticle is affected less by thermally driven effects. Smaller nanoparticles can melt during irradiation, as shown by simulations in sections 4.2 and 5.1 and solidify as a sphere because of surface tension and therefore do not show a pronounced shape change towards conical shape.

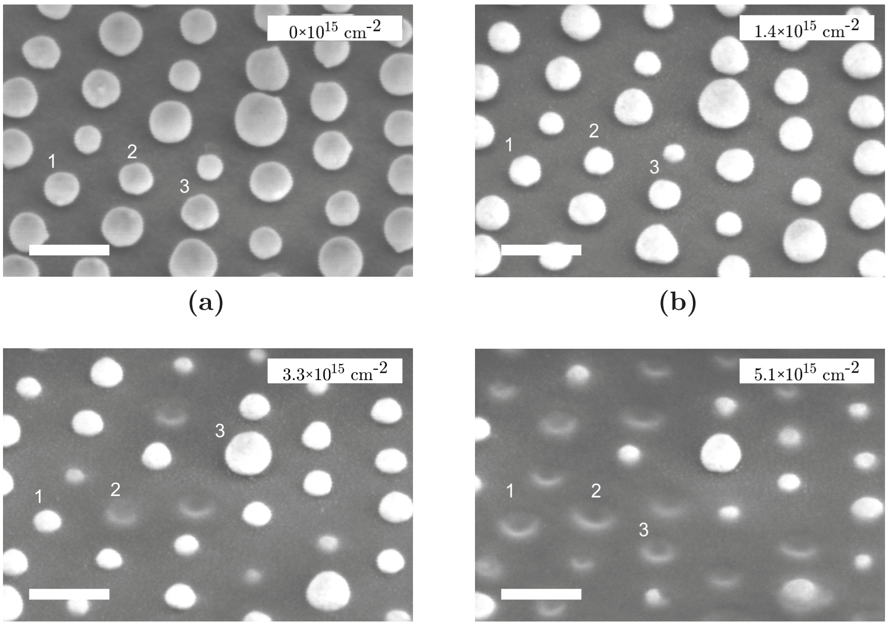

(a) **(b)** **(c)** **(d)**

Figure 5.9: SEM images of a Au nanoparticle array taken under an angle of 52 ° before (a) and after Ga^+ ion irradiation of different fluences: (b) $1.4 \cdot 10^{15}\,\text{ions}/\text{cm}^2$, (c) $3.3 \cdot 10^{15}\,\text{ions}/\text{cm}^2$, (d) $5.1 \cdot 10^{15}\,\text{ions}/\text{cm}^2$. The nanoparticles show a different sputtering behavior, even at similar initial sizes (marked with numbers 1 to 3). Almost all nanoparticles, except the largest, vanished after a fluence of $5 \cdot 10^{15}\,\text{ions}/\text{cm}^2$. The scale bar represents 100 nm, respectively.

Three particles with an almost equal initial size are marked in figure 5.9. Over the process of irradiation, particle 2 shrinks significantly faster than particles 1 and 3. This difference in shrinking rate becomes apparent after a fluence of $3 \cdot 10^{15}\,\text{ions}/\text{cm}^2$. The origin of this behavior could either be a different orientation of low index axises with respect to the ion beam and the dependence of the sputter yield on the lattice orientation or redeposition of sputtered atoms from neighboring particles, which slows down the sputtering of nanoparticles. The origin of different sputtering rates is discussed in detail in chapter 6.

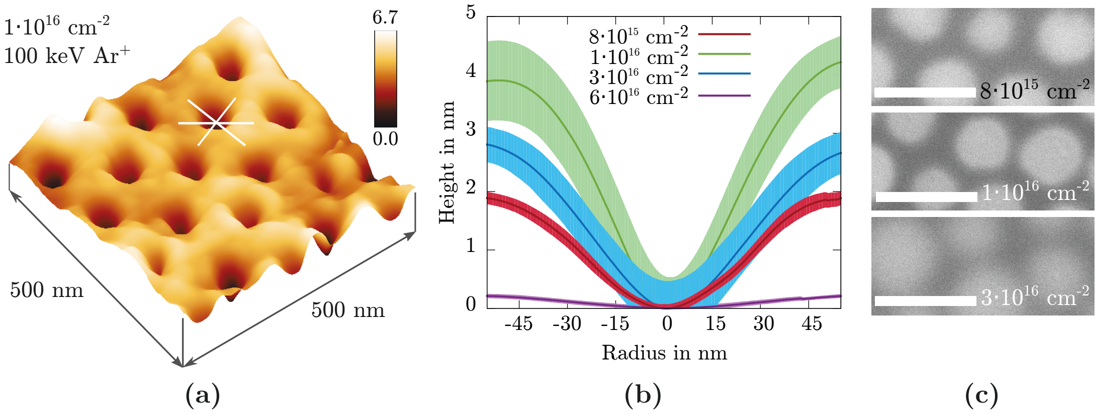

Figure 5.10: (a) Exemplary AFM image of a Si sample, which was covered with Au nanoparticles before irradiation, irradiated with $1 \cdot 10^{16}$ ions/cm² 100 keV Ar$^+$ ions. The positions where the nanoparticles used to lie are craters after high fluence irradiation. The three white lines show representative line scans taken for cross sections over a crater. (b) Profiles of the craters in Si for different ion fluences of 100 keV Ar$^+$ ions. The light colored areas indicate the error of the respective profiles. (c) SEM backscatter electron images of Si substrates after irradiation with different fluences of 100 keV Ar$^+$ ions. The bright regions correspond to Au in the Si substrate. No nanoparticles are visible on top of the substrates. The scale bars indicate 100 nm.

5.3 Particle-substrate interaction

AFM, SEM and STEM investigation Si substrates covered with 50 nm Au nanoparticles were irradiated with 100 keV Ar$^+$ with different fluences from $1 \cdot 10^{15}$ to $6 \cdot 10^{16}$ ions/cm² to analyze the particle-substrate interaction. All samples showed craters after irradiation at the nanoparticle positions, if the nanoparticles vanished during the irradiation process (compare figures 5.9c and 5.9d). A typical AFM image for a sample irradiated with a fluence of $1 \cdot 10^{16}$ ions/cm² is shown in figure 5.10a. The craters are arranged similar as the nanoparticles before. The depth of the craters is ion fluence dependent. Therefore, cross sections of ten craters of each sample were measured in three different directions through the minimum (see figure 5.10a). The average results are shown in figure 5.10b as a function of ion fluence. The depth of the crater was ~ 2 nm at a fluence of $8 \cdot 10^{15}$ ions/cm² and increased to a fluence of $1 \cdot 10^{16}$ ions/cm², where it reaches a depth of ~ 4 nm. With further increasing fluence the crater depth is decreasing again. At the maximum fluence of $6 \cdot 10^{16}$ ions/cm², the craters are barely visible with depths below 1 nm. The width of the craters, however, are constant over the fluence. SEM images with backscatter electrons were used to investigate whether Au is left in the substrate in vicinity of the craters. Three different SEM images for different fluences are shown in figure 5.10c. Electrons are favorably backscattered on high mass elements in a sample, which is why the bright regions in the images show likely incorporated Au and the dark regions pure Si of the substrate. Gold is present in regions below the former nanoparticles

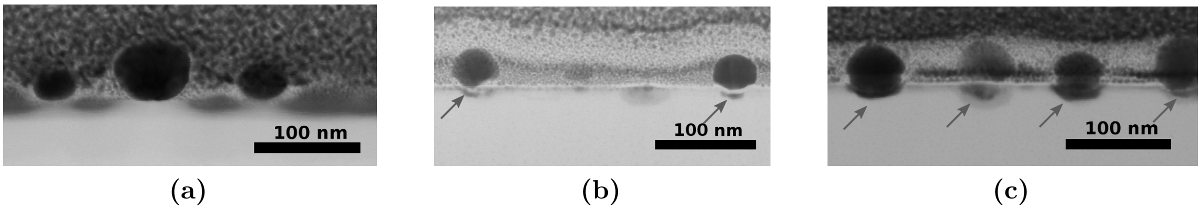

Figure 5.11: STEM images of Au nanoparticles on a Si substrate (a) before irradiation and after irradiation with (b) 100 keV and (c) 350 keV Ar^+ ions with an ion fluence of $3 \cdot 10^{15}$ ions/cm². In all images the deposited Pt on top of the nanoparticles and substrate is visible. The Pt deposition caused some damage in the Si substrate in the uncovered areas, visible as dark parts in the substrate area in (a). The particles are lying on top of the substrate before irradiation. The nanoparticles are partly sinking into the substrate and the nanoparticle material is intermixing with the substrate after irradiation with ions, visible as dark areas beneath the nanoparticles in (b) and (c) (marked with arrows). The intermixing is stronger for higher ion energies and thus with higher ion range, as visible from comparison of image (b) and (c).

after all fluences. It is also noticeable that Au is distributed over a larger areas for a fluence of $3 \cdot 10^{16}$ ions/cm² compared to the lower fluences. The reason for this is ion beam mixing, which is discussed in detail in the following paragraph.

Representative TEM lamellas of irradiated and unirradiated samples were prepared using a FIB system in order to investigate the Au distribution inside the substrate after irradiation in beam direction. STEM images of three lamellas are shown in figure 5.11. The images show nanoparticles before (figure 5.11a) and after irradiation with 100 keV (figure 5.11b) and 350 keV Ar^+ ions (5.11c). In figure 5.11a, Au nanoparticles on top of Si and embedded in deposited platinum (Pt), which is necesarry for TEM lamella preperation, can be observed. The dark parts in the substrate are damaged Si areas due to Pt deposition on uncovered parts of the substrate. Figure 5.11b shows nanoparticles after 100 keV Ar^+ irradiation. It is apparent that the depicted nanoparticles sank slightly into the substrate. In addition, dark areas are visible directly beneath the particles, indicating Au-Si mixed regions. With increasing Ar^+ ion energy up to 350 keV, the ion range is also increasing. Thus, more material and intermixing of nanoparticle and substrate is visible in figure 5.11c, where the sample was irradiated with 350 keV Ar^+ ions. The particles are now buried deeper into the substrate and the darkened areas beneath the nanoparticles are larger and more pronounced. According to Klimmer *et al.* [106], the reason for the burrowing of nanoparticles irradiated with ion beams is locally induced viscosity and resulting capillary forces according to the work of Hu *et al.* [143]. As a result of the viscous flow of the substrate upon irradiation, nanoparticles sink into the substrate, depending on their size, the irradiated fluence, the substrate material and ion species [106].

The intermixing areas beneath the nanoparticles are caused by the effect of ion beam mixing [144]. If the ion range is larger than the particle diameter, ions can enter the substrate after traversing the particle. Because the momentum of the ion is directed

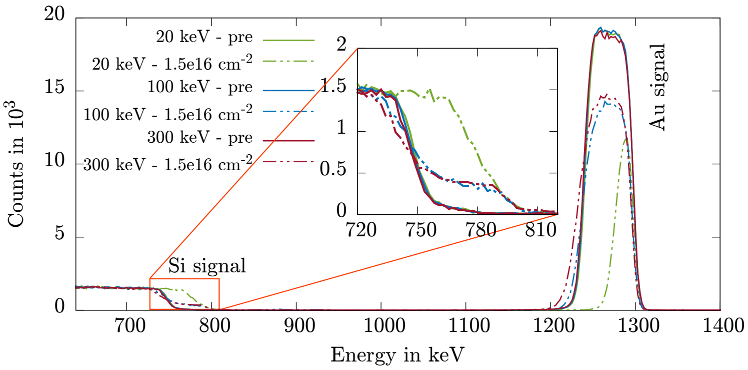

Figure 5.12: RBS spectra of Si samples with 40 nm Au layers on top. The solid lines show the spectra of the samples before irradiation. The dashed lines show the results after irradiation with 20 keV (green), 100 keV (blue) and 300 keV (red) Ar^+ ions. All irradiations were performed using a total ion fluence of $1.5 \cdot 10^{16}$ ions/cm². The inset shows the detailed section of the Si spectra of the samples. The step in the spectra indicate an intermixing layer of Au and Si.

towards the substrate, atoms from the particle which are sputtered are also likely to be sputtered in forward direction towards the substrate and can be incorporated into the substrate. Additionally, also scattered atoms from the substrate can be transfered into the particle. An intermixed layer, ranging from the bottom of the particle towards the substrate, successively forms during irradiation, which can influence the sputtering process significantly.

RBS investigation An experiment with thin Au layers on Si substrates was performed to simulate the nanoparticle-substrate interaction. At first, a 40 nm thick Au layers were thermally evaporated on Si substrates with native oxide layer. These samples were irradiated with Ar^+ ions to a total fluence of $1.5 \cdot 10^{16}$ ions/cm² in steps of $0.5 \cdot 10^{16}$ ions/cm². The ion energy ranged from 20 to 300 keV to cover the whole energy range used in the nanoparticle experiments presented in section 5.1. The samples were investigated using 1.4 MeV He^+ RBS in random direction before and after each irradiation step in order to determine the sputter yield of the Au layer.

The results of these experiments are shown in figure 5.12. The Si signal can be seen at energies below ~ 810 keV and the Au signal between energies of 1200 and 1300 keV. The pre-irradiadiation curves are in almost perfect agreement, indicating homogeneous initial Au layers. The dashed lines show the spectra for the samples after irradiation with 20 keV, 100 keV and 300 keV Ar^+ ions with an ion fluence of $1.5 \cdot 10^{16}$ ions/cm². First of all, it is apparent that the shape of both Au and Si signal change during irradiation, depending on the ion energy. The spectrum after 20 keV Ar^+ irradiation shows a decrease of the Au signal in height and width and a shift of the Si signal towards higher energies. The Au layer thins due to sputtering and the He^+ ions, which are scattered at Si atoms, have a higher energy. The spectra of Au layers irradiated with higher Ar^+ ion energies

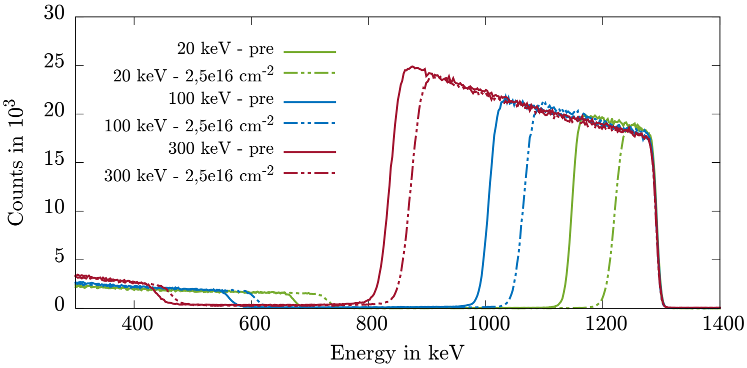

Figure 5.13: RBS spectra of Si samples with 100 nm (green), 200 nm (blue) and 300 nm (red) thick Au layers on top. The samples with 100, 200 and 300 nm thick Au layer were irradiated with 20, 100 and 300 keV Ar$^+$ ions, respectively. The RBS spectra were measured before (solid lines) and after (dashed lines) the irradiation with a total ion fluence of $2.5 \cdot 10^{16}$ ions/cm².

show a different behavior. The height of the Au signal decreases due to less Au on the sample. Gold is distributed over a larger depth in the sample, thus the width of the Au peak is broadened and the starting point is shifted to lower energies for Ar$^+$ ion energies of 100 keV and 300 keV. Au was incorporated into the Si substrate which is obvious when taking a closer look at the Si signal, especially at the inset of figure 5.12. A step is noticeable in the Si signal for ion energies of 100 keV and 300 keV. This indicates that in depths, where He$^+$ ions are scattered at Si atoms, also other scattering processes, in this case at Au atoms, appear. Therefore, energies between 195 and 210 keV show the intermixing layer of Au and Si. The steps in the Si signals are almost equally shaped for both 100 and 300 keV Ar$^+$ irradiation. This shows the solid solubility of Au in Si.

Subsequently, thicker Au layers were evaporated on Si substrates and irradiated with Ar$^+$ ions of the same ion energies and a total ion fluence of $2.5 \cdot 10^{16}$ ions/cm² in steps of $0.5 \cdot 10^{16}$ ions/cm². The thicknesses of the Au layers were 100, 200 and 300 nm for irradiations with 20, 100 and 300 keV Ar$^+$ ions, respectively. The Au layer thicknesses were chosen in a way that even for the largest ion fluence the layer is still thick enough to stop all ions completely. The RBS spectra of these experiments are shown in figure 5.13. Only the width of the Au peak decreased as result of sputtering. The height of the spectra before and after irradiation remained the same. Thus, no intermixing took place in these experiments, because the Ar$^+$ ions were fully stopped within the Au layer.

The evolution of the 40 nm thick Au layer RBS signal under consecutive ion irradiation is shown in figure 5.14. The signals of Au (5.14a) and Si (5.14b) are shown for different ion energies and different ion fluences. The results for 20 keV irradiation show the expected behavior for a decreasing Au layer because of sputtering. The spectra of the 100 keV and 300 keV spectra show how gold silicide forms. The amount of Au decreases from the pristine sample to the state after $0.5 \cdot 10^{16}$ ions/cm². However, the broadness of the peak remains almost constant. This is a result of the intermixing of Au and Si, as the Au is

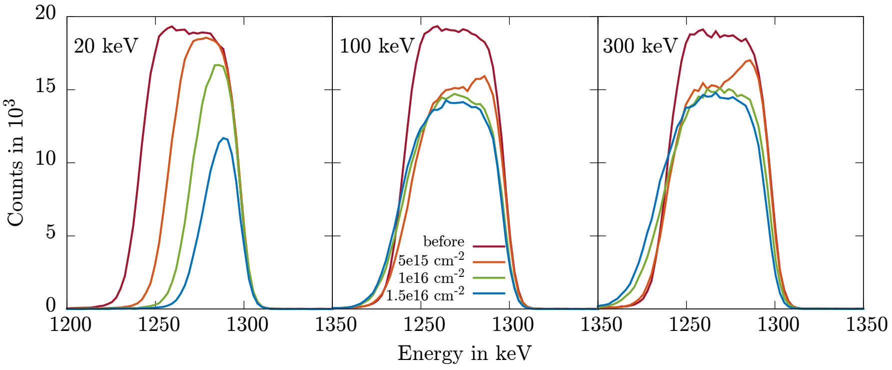

(a)

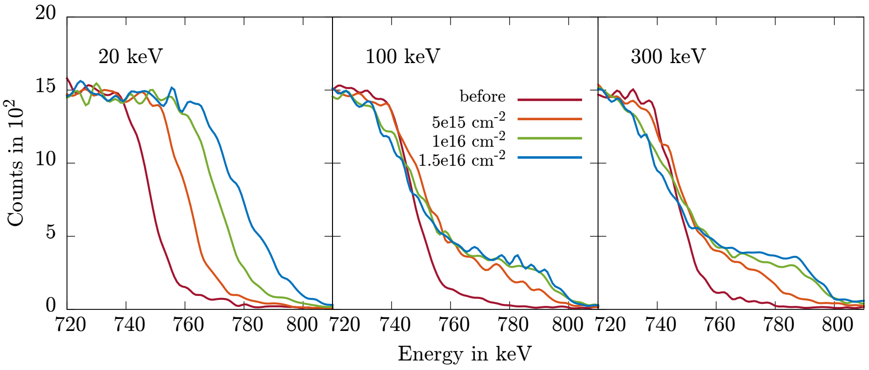

(b)

Figure 5.14: Evolution of the RBS signals of (a) Au and (b) Si irradiated with Ar^+ ion energies of 20, 100 and 300 keV and different ion fluences. The initial Au layer thickness was 40 nm. The Au layer intermixes with the Si substrate, which is clearly visible for 100 and 300 keV Ar^+ irradiation with increasing ion fluence, if the ion range is larger than the Au layer thickness.

pushed into the substrate and Si into the Au layer. The concentrations of Au and Si in the intermixed layer after 100 and 300 keV Ar+ irradiation is 55 at% and 45 at%, respectively. With increasing ion fluence, the peaks of the 100 keV and 300 keV irradiations broaden even more. The Au signals after $1.0 \cdot 10^{16}\ {}^{\mathrm{ions}}/_{\mathrm{cm}^2}$ and $1.5 \cdot 10^{16}\ {}^{\mathrm{ions}}/_{\mathrm{cm}^2}$ are significantly enhanced at energies below ~ 1220 keV compared to the $0.5 \cdot 10^{16}\ {}^{\mathrm{ions}}/_{\mathrm{cm}^2}$ signals.

The influence of the intermixing of Au and Si on sputtering was investigated by comparing the results of the RBS measurements as a function of ion fluence on both thin and thick Au layers. The atomic area density of Au is obtained by integrating the RBS counts of the Au peaks in figure 5.14 over all energies. The atomic area densities are shown in figure 5.15 for all Au layer thicknesses and ion energies. The atomic density is decreasing almost linearly for 20 keV Ar^+ ions, which indicates that each irradiation step removed about the same amount of Au from the sample. With increasing ion energy, already at 50 keV, the trend of the atomic density is non-linear for thin films and the decrease of the atomic density is slowing down with increasing ion fluence. The atomic density seems to saturate for ion energies larger than 70 keV at a fluence of $1.0 \cdot 10^{16}\ {}^{\mathrm{ions}}/_{\mathrm{cm}^2}$.

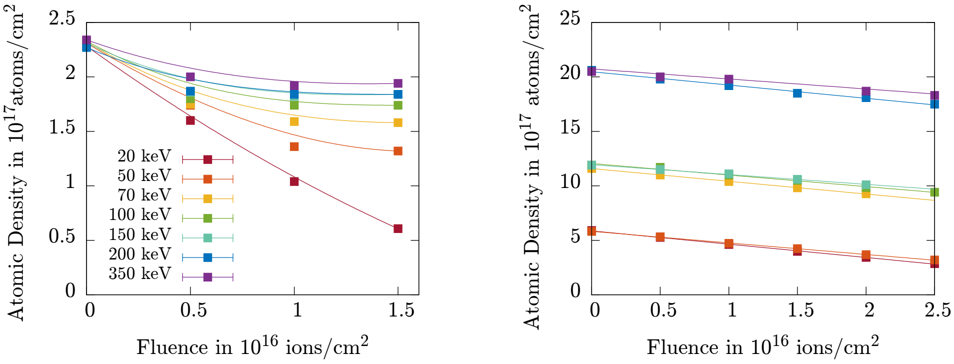

(a) **(b)**

Figure 5.15: Atomic area densities of Au as a function of the ion fluence for different Au layer thicknesses and Ar^+ ion energies. (a) Atomic densities for samples with 40 nm thick Au layer on Si substrate for different ion fluencies and various ion energies. The atomic density saturates for almost all ion energies with increasing ion fluence, if the ion range is large compared to the Au layer thickness. The curves are guides to the eye. (b) Results for samples, where the Au layer was in any case thicker than the ion range at the respective energies. The atomic density is decreasing linearly with ion fluence. The lower set of data points are for Au layer thicknesses of 100 nm, the middle set of data points represents Au layer thicknesses of 200 nm and the upper data points show results for 300 nm thick Au layers. The lines are linear fits of the data points. The color coding is the same for both figures.

No Au is sputtered anymore from the sample. This is a result of ion beam mixing for ion ranges larger than 40 nm and preferential sputtering of Si (compare equation 2.7). The intermixing of Au and Si slows down the sputtering process of Au and stops almost completely when the layers are fully mixed to gold silicide.

The atomic densities as a function of the ion fluence for Au layers thicker than the ion range are shown in figure 5.15b. The atomic density is decreasing linearly with ion fluence for all ion energies. The amount of sputtered Au is the same in each irradiation step. The sputter yield can be derived from the data in figure 5.15 by measuring the slope between data points. The sputter yield is given as a function of energy in three intervals, 1) derived from 0 to $0.5 \cdot 10^{15}$ ions/cm², 2) $0.5 \cdot 10^{15}$ ions/cm² to $1.0 \cdot 10^{15}$ ions/cm² and 3) $1.0 \cdot 10^{15}$ ions/cm² to $1.5 \cdot 10^{15}$ ions/cm² in figure 5.16a. In agreement with Mayer *et al.* [144], the ion beam mixing process becomes more pronounced with increasing ion energy and thus the sputter yields are decreasing faster with increasing ion fluence. The sputter yields are near 0 for ion energies of 100 keV and above, for measurements using ion fluences of $1.0 \cdot 10^{16}$ ions/cm² and larger. The fraction of gold silicide is increasing with increasing ion fluence, while the sputtering of Au is decreased due to preferential sputtering. The sputter yields for layer thicknesses for which the intermixing is ruled out are shown in figure 5.16b. The trend of the experimentally obtained data points follows the trend given by the *iradina* simulation, although the absolute values are around 3 times larger compared to the simulation. The cause of the discrepancy between experiment and MC simulation are the same as already

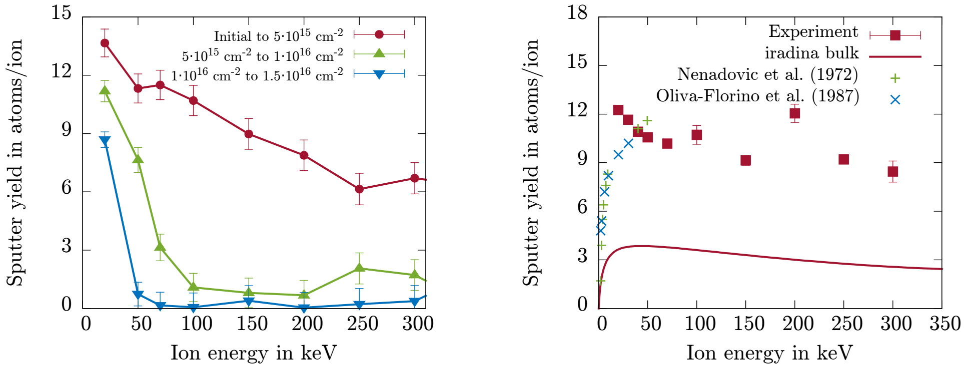

(a) (b)

Figure 5.16: Experimentally obtained sputter yields as a function of ion energy for Au layers on Si irradiated with Ar^+ ions. (a) Results for Au layers with a thickness of 40 nm. The results are shown for different fluence intervals as circular and triangular data points with dotted lines. The error bars of the interval data points are the errors due to the fit. The sputter yield decreases with increasing ion energy and increasing ion fluence. (b) Sputter yields for samples with thick Au layers. The experimental data is shown as red data points. The error bars are the fitting errors. The simulation result for bulk geometry by *iradina* is shown as solid red line. Additionally, results from the literature for small ion energies obtained by Nenadovic *et al.* [145] (green crosses) and Oliva-Florio *et al.* [146] (blue crosses) are shown.

discussed in section 5.1. In contrast to figure 5.16a, the sputter yield decreases slower with increasing ion energy. The obtained values extend the available literature data and are in good agreement with those in references [145, 146] for ion energies smaller than 50 keV.

The results discussed here can explain the formation of craters shown in the previous paragraph and especially in figure 5.10. The Au from the nanoparticles is mixed into the substrate and remains there, even for high fluence irradiation, and Si is preferentially sputtered. This leads to a local enhancement of Si sputtering at the nanoparticle positions compared to the surrounding substrate and therefore to crater formation. The crater depth increases with increasing ion fluence. However, the substrate around the crater is also sputtered, which leads to an antagonizing effect that the crater is sputtered at the top. While the irradiation proceeds, the Au is further distributed in the substrate due to ion beam mixing. This was shown in figure 5.10c for a fluence of $3 \cdot 10^{16}\,{}^{\mathrm{ions}}/_{\mathrm{cm}^2}$ compared to smaller fluences. As a result, Si is sputtered almost everywhere after a certain fluence and the surface smooths again with a decrease of crater depth. This effect is used in the "surfactant sputtering" technique for surface patterning and structuring [147, 148].

5.4 Summary

Section 5.1 and 5.2 presented the sputter yields of Ar^+ and Ga^+ irradiated Au nanoparticles as a function of ion energy and nanoparticle diameter by high resolution SEM measurements on Au nanoparticle arrays and *in situ* measurements on single Au nanoparticles and arrays. Both experimental methods reproduced the trend of the *iradina* simulation results presented in chapter 4 qualitatively, but were quantitatively higher due to the simplified assumptions in BCA based *iradina*. Thermally driven effects like melting and evaporation of Au nanoparticles occured for Ar^+ irradiation with ion energies between 110 and 250 keV, which could be explained by the MD simulation results presented in chapter 4. The *in situ* experiment on a Au nanoparticle array revealed different sputtering rates of equally sized nanoparticles, which can be explained either by ion channeling [34] or redeposition of sputtered material (see chapter 6). Additionaly, an interaction of nanoparticles and substrate was visible. The *in situ* measurement of the sputter yield of single Au nanoparticles irradiated with Ga^+ ions with energies from 1 to 30 keV were limited by these particle-substrate interactions.

The particle-substrate interaction was investigated by AFM, SEM, STEM and RBS measurements and presented in section 5.3. STEM images of 100 keV Ar^+ irradiated Au nanoparticles revealed that nanoparticles sink into the substrate with increasing ion fluence. AFM measurements on 100 keV Ar^+ irradiated Au nanoparticles revealed crater formation at the nanoparticle positions after high fluence irradiation. The crater depth varied with fluence, while the crater width was independent of the ion fluence. Backscattering SEM images showed Au at the nanoparticle positions where no nanoparticles were left on the surface. RBS measurements on thin Au films on Si showed intermixing of Au and Si with increasing ion fluence. These RBS measurements led to the conclusion that the sputtering of nanoparticles is lowered by the intermixing processes. Since the particles are only slightly sunken into the substrate in the array experiment presented in section 5.1, the effect is rather small for ion fluences smaller than $3 \cdot 10^{15}\,\mathrm{ions/cm^2}$, as the STEM images showed. However, the effect has a larger impact on the *in situ* experiments on single Au nanoparticles shown in section 5.2, because the ion fluences here were larger compared to the array experiments and an intermixing of nanoparticle and substrate is clearly visible at higher fluences, although the ion ranges of Ga^+ ions with energies below 30 keV are rather small.

6 | Redeposition

This chapter displays the sputtering and redeposition of atoms on ion irradiated Au nanoparticle arrays. Results of a newly developed MC simulation code are directly compared to *in situ* experiments. The work was done in collaboration with Kai Nordlund, Flyura Djurebakova and Andrey Ilinov from the University of Helsinki. Parts of sections 6.2 and 6.3 were recently submitted to New Journal of Physics [149]. The Au nanoparticle samples were fabricated by Christoph Stanglmair from the group of Claudia Pacholski at the MPI for Intelligent Systems in Stuttgart.

6.1 Dual particle interaction

Simulation details The interaction between two nanoparticles was modeled using the algorithm presented in section 3.4.2. Two particles with three different size combinations were set next to each other with a rim-to-rim distance of 50 nm in every case (as schematically shown in figure 3.8b). The size of one nanoparticle was kept constant at 50 nm while the other particle's diamater was varied between 10, 50 and 90 nm. Gallium ions with an energy of 25 keV were used with an ion fluence of $5 \cdot 10^{14}\ \mathrm{ions/cm^2}$. The number of simulated ions was calculated with respect to the cross section area of the two particles at the beginning and every simulated ion hit one of the two particles randomly. The sputtering results obtained by *iradina* (compare section 4.2) and the sputtering model presented by Järvi *et al.* [51] were used for the calculations. Angular distributions of sputtered atoms obtained by *iradina* simulations (see section 4.3) were in use for various nanoparticle sizes. Only results by *iradina* inputs are discussed here, since the observed behavior is the same for both *iradina* and Järvi's model, they only differ in absolute numbers.

Simulation results Figures 6.1a to 6.1c show the evolution of the particle's size as a function of the number of impinged ions. In cases of different nanoparticle sizes, shown in figures 6.1a and 6.1c, the smaller particles decreased faster in size because of higher sputter yields of smaller particles compared to larger ones. The size decrease of equally sized nanoparticles is almost the same, as shown in figure 6.1b. However, after $\sim 7 \cdot 10^3$ ions, one particle shrinks slightly faster than the other.

The number of sputtered atoms as a function of the number of ions is shown in figure 6.1d and 6.1f. The larger nanoparticle always sputters more material than the smaller one, because of a higher probability of being hit by an ion. When comparing equally sized

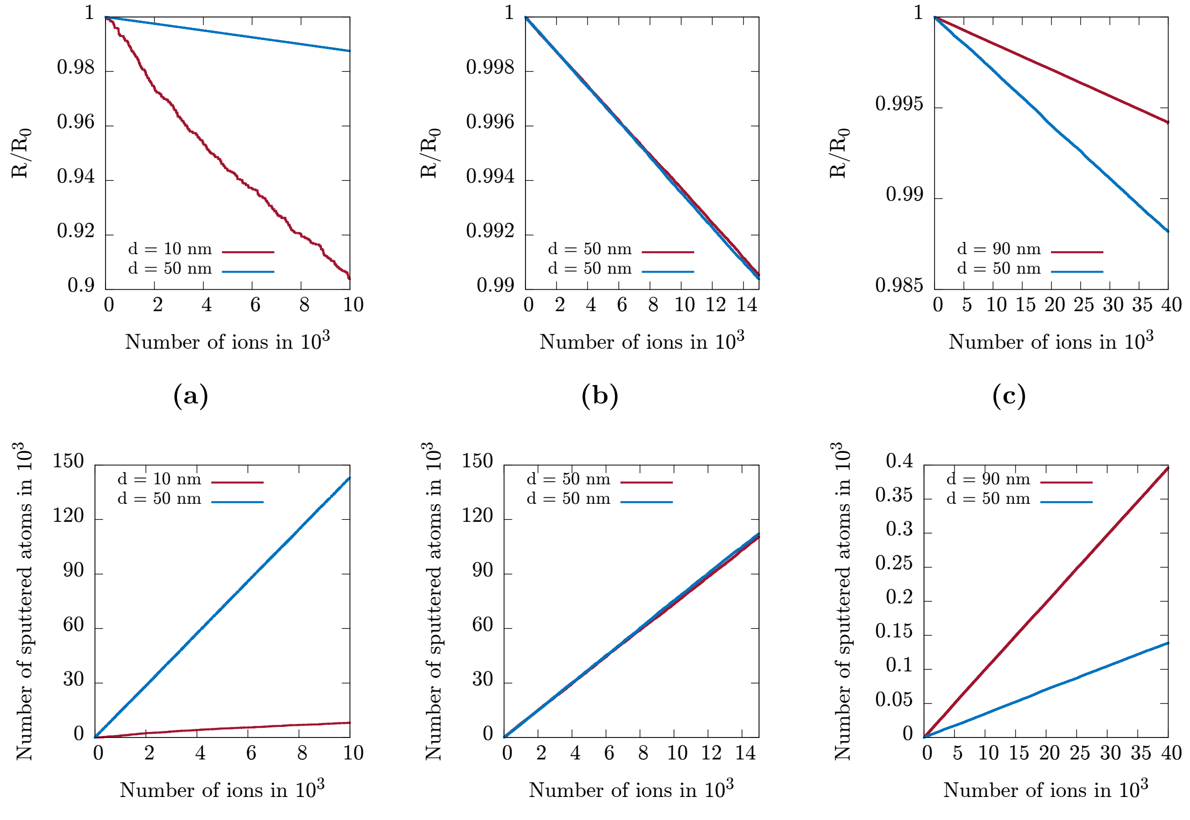

(a) **(b)** **(c)**

(d) **(e)** **(f)**

Figure 6.1: Simulation results for the interaction of two Ga$^+$ irradiated Au nanoparticles. Three simulations were performed with three different size combinations: 10 nm–50 nm, 50 nm–50 nm and 90 nm–50 nm. Figures (a) to (c) show the fraction of particle radii of the particles versus the initial particle radius as a function of the number of impinged ions on the simulation volume. Figures (d) to (f) show the number of sputtered atoms from the particles for the three particle size combinations. The colors for the respective nanoparticle sizes are shown in the images. The result for the particle with a constant diameter of 50 nm is always plotted in blue.

nanoparticles in terms of sputtered atoms (figure 6.1e), the particle with a slightly faster size decrease rate (figure 6.1b) sputters slightly more material.

The number of collected atoms is plotted in figures 6.2a to 6.2c as a function of the different size combinations. It is apparent in figure 6.2a that the nanoparticle with a diameter of 10 nm collects 5 times more atoms than the 50 nm sized nanoparticle, because the 50 nm nanoparticle emits two orders of magnitude more atoms than the 10 nm sized particle. In case of the 90 nm–50 nm combination (figure 6.2c), the larger nanoparticle collects more material, because the difference between the total number of sputtered atoms for the two particles is not as large as for the 10 nm–50 nm combination and the 90 nm sized nanoparticle covers a larger solid angle Ω. Figure 6.2b shows the number of collected atoms of equally sized nanoparticles. Both nanoparticles collect approximately the same number of atoms, although the number is oscillating over the course of the simulated irradiation.

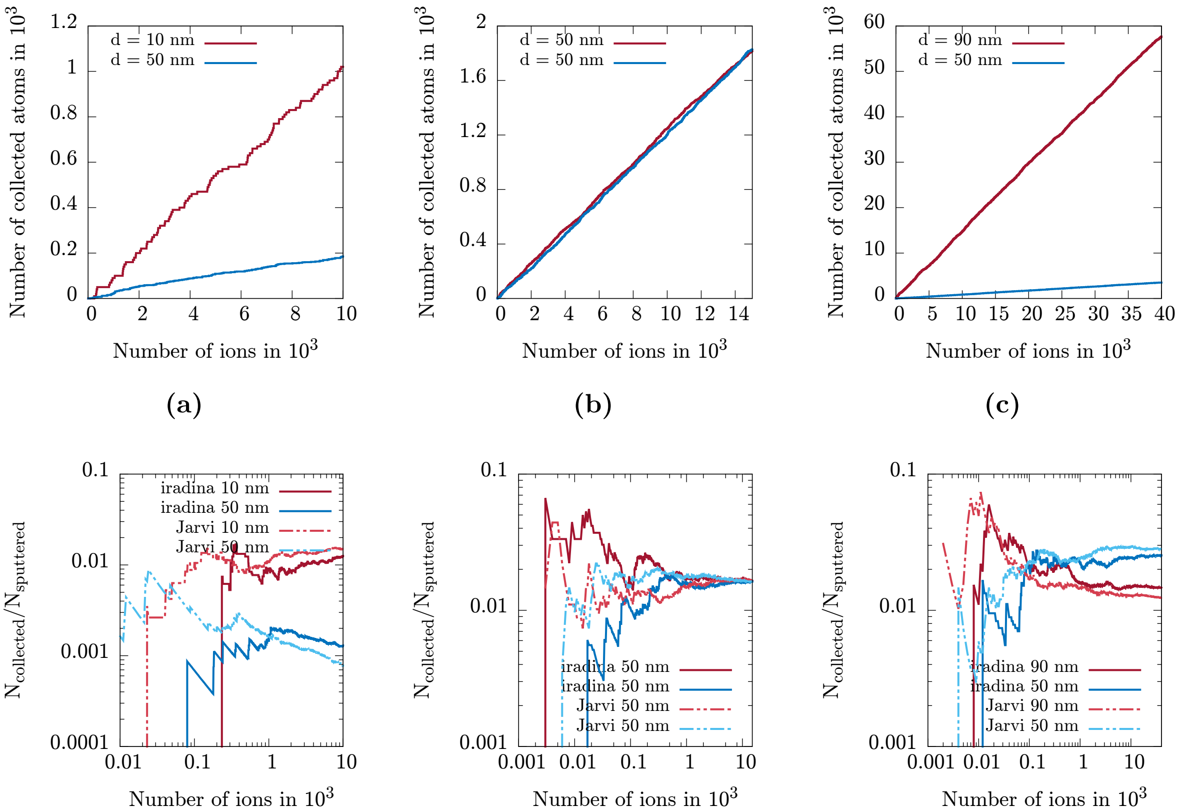

(a) (b) (c)

(d) (e) (f)

Figure 6.2: Simulation results for the interaction of two ion irradiated Au nanoparticles. The results for the numbers of sputtered atoms and the ratio of collected versus sputtered atoms as a function of the number of impinged ions on the nanoparticles are shown for three different size combinations. Figures (a) to (c) show the number of collected atoms for the different size combinations. The ratio of collected versus sputtered atoms is plotted for different size combinations and two different sputtering models in figures (d) to (f): *iradina* (solid lines) and Järvi [51] (dashed lines). Different sputtering models lead to a comparable result in terms of collecting versus sputtering.

The conclusive summary of the redeposition behavior for two nanoparticles is depicted in figures 6.2d to 6.2f for different size combinations. Here, the fraction of collected versus sputtered atoms as a function of the number of impinged ions is shown for both *iradina* and Järvi's sputtering models. At first it is obvious that both sputtering models lead to approximately the same result. This shows that the simulation is working properly. The logarithmic plot emphasizes the stochastic nature of the process. The fraction of collected versus sputtered atoms is around 1 % for the 10 nm sized particle, while the larger 50 nm sized particles shows a fraction of around 0.1 % for both sputtering models after 10^4 ions. Therefore, the influence of redeposition on the size decrease of the 50 nm sized nanoparticle is therefore negligible. For the 50 nm–90 nm nanoparticle combination, the fraction of collected versus sputtered atoms reaches a value of around 2 % and 1 %, respectively, after 10^4 ions. The equally sized nanoparticles (figure 6.2e) both reach values

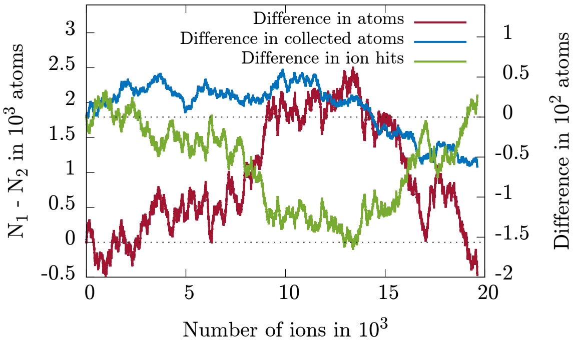

Figure 6.3: Difference in nanoparticle parameters for the combination of equally sized nanoparticles with a diameter of 50 nm. The difference in number of atoms between both are shown as a red line on the left axis over the number of impinged ions. The difference in the number of collected atoms is plotted as a blue line using the right axis. The difference in the number of ions hitting the nanoparticles is plotted as a green line on the right axis. The zero axes of the respective y axes are plotted as black dotted lines.

of collected versus sputtered number of atoms of $\sim 2\,\%$.

The interaction between equally sized particles should be discussed further in detail. Figure 6.3 shows details from the simulation between equally sized nanoparticles with a diameter of 50 nm. Differences between the number of atoms, the number of collected atoms and the number of ion hits of the two nanoparticles are shown in order to highlight the previously discussed differences in the simulation results. The difference between the number of atoms is directly correlated to the difference in the number of ion hits. The nanoparticle, which receives most ion hits loses most atoms, of course. Additionally, the nanoparticle with less ion hits collects more atoms. However, the trend turns after $\sim 14 \cdot 10^3$ ion impacts. The nanoparticle, which was hit more often before now receives less ion impacts and collects more atoms. The sputtering and collection of atoms of both particles oscillates over the number of ion impacts. Several simulations with equally sized particles confirm this result. In total, both particles lose and collect almost the same amount of material with some fluctuations in the sputtering/collection of atoms during the process, especially at the beginning of the simulation.

6.2 Interaction of nanoparticle arrays

Simulation details Several simulations with different starting conditions and sputtering models were performed to investigate the interaction of ion irradiated Au nanoparticles, ordered in an array, in detail. Simulations with a 4×4 grid were performed 120 times in order to analyze the sputtering and redeposition processes statistically. The nanoparticles were positioned in the center of the square-shaped cells with a side length (cell size) of 95 nm, which corresponds to the average interparticle distance in the experiments (see section 5.1 and reference [137] for details). The nanoparticle size distribution used for these simulations was the experimentally obtained Gaussian size distribution with a mean diameter of 51.0 nm and a standard deviation of 7.6 nm. The nanoparticle sizes were randomly chosen from this distribution. It is unlikely that particle sizes smaller than 20 nm appear in the simulations using the described size distribution. Thus, another 120 simulations with a Gaussian size distribution with a mean diameter of 25.0 nm and a standard deviation of 7.6 nm were performed in order to achieve a better understanding of the interaction of particles with diameters smaller than 20 nm. The grid and cell size were the same as in previous simulations. Järvi's and scaled Järvi's model (see figure 5.4b, section 5.1) were used to investigate the influence of the absolute amount of sputtering on the statistics. Additionally, a set of simulations was carried out using scaled Järvi's model, where the redeposition was switched off, in order to understand the role of redeposition.
A first simulation with equal sized nanoparticles with a diameter of 50 nm was performed to analyze the influence of the cut-off distance parameter d_{cut} on the number of redeposited atoms, as the computational time had to be optimized. For this purpose, d_{cut} was variied between 10 and 2 000 nm. The cell size was kept constant at 95 nm. The results for these simulations are shown in figure 6.4, where the number of redeposited atoms is plotted as a function of the cut-off distance. The number of redeposited atoms is zero for d_{cut} being smaller than the interparticle distance, of course. If the value of d_{cut} surpasses the interparticle distance, the number of redeposited atoms increases fast with d_{cut}. The number of redeposited atoms reaches a maximum at $d_{cut} = 500$ nm and saturates at this value for further increasing d_{cut}. The number of redeposited atoms shows

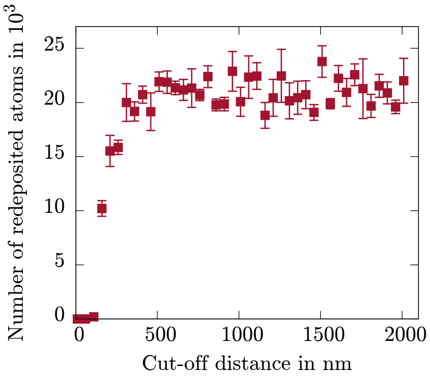

Figure 6.4: Number of redeposited atoms as a function of the cut-off distance parameter. The error bars represent the statistical errors. The number of redeposited atoms is almost constant for recoil ranges larger than 5000 Å. This value is used for the presented simulations.

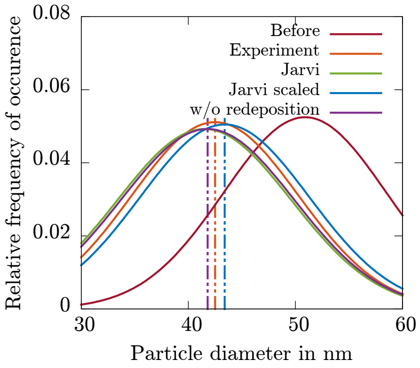

Figure 6.5: Size distributions of the nanoparticles before (dark red) and after the experimental (orange) and simulated irradiation with 25 keV Ga^+ ions for different sputtering models: Järvi (green), scaled Järvi (blue) and without redeposition (purple). Only the Gaussian fits of the size distributions are shown for reasons of clarity. The mean values are plotted as dashed lines in the respective color.

only fluctuations around the saturation value for larger d_{cut}. Therefore, a value of d_{cut} of 500 nm is suitable for the simulations and was fixed for all further described simulations in this chapter.

Statistical Results The size distributions of the nanoparticles of both experiment and simulations before and after irradiation are shown in figure 6.5. Only the Gaussian fits to the size distributions are shown for clarity. The Gaussian shape of the distributions are conserved in all investigated cases after irradiation. The mean diameters of the size distributions shift to smaller values due to sputtering, compared to the initial size distribution. Table 6.1 lists the mean values and standard deviations of the size distributions. Compared to the mean diameter of 42.5 nm of the experiment after irradiation, the simulation using Järvi's model underestimates the mean diameter after irradiation by $\sim$ 1 nm, while the simulation with scaled Järvi's model slightly overestimates it. However, both simulations match the experimental result within the error, while the mean diameters of both simulations after irradiation differ only by 2 nm. Thus, only the simulation results using scaled Järvi's model are discussed in the following paragraphs.
The number of sputtered and collected atoms are shown as a function of the initial nanoparticle diameter in figures 6.6a and 6.6b, respectively. Two domains are noticeable in the graphs: (1) The upper data shows the simulation results with the experimental size distribution with a mean diameter of around 50 nm. (2) The lower part shows the simulation results using the size distribution with the small mean diameter of 25 nm. Figure 6.6a shows the number of sputtered atoms as a function of the initial nanoparticle diameter. The plot shows a quadratic relation between sputtered atoms and nanoparticle size for both size regimes. Since the sputter yield reaches a maximum for nanoparticles

Table 6.1: Mean sizes and standard deviations of size distributions before and after irradiation for simulations and experiment. The irradiated fluence was $3 \cdot 10^{15}\,\mathrm{ions/cm^2}$. The simulations used the scaled Järvi model for sputter calculations.

	Before	Experiment	Järvi	Järvi scaled	w/o redeposition
d [nm]	50.9	42.5	41.5	43.4	41.8
σ [nm]	7.6	7.8	8.1	7.9	8.1

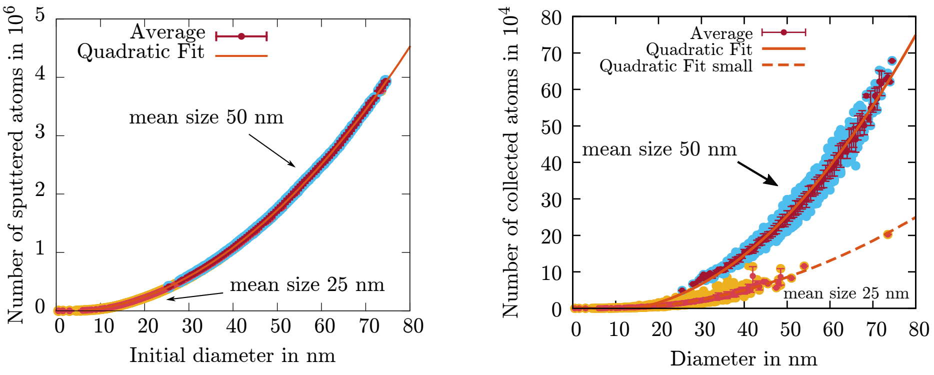

(a) **(b)**

Figure 6.6: (a) Number of sputtered atoms as a function of the initial particle size. A quadratic fit is shown to underline the trend. (b) Number of sputtered atoms as a function of the initial particle diameter. The blue and yellow points in both figures are the results for single nanoparticles for a mean initial size distribution with a mean diameter of 50 and 25 nm, respectively. The dark and light red points are the mean values of the shown quantity for 50 and 25 nm, respectively. Quadratic fits are shown for the different size distributions in orange color as a solid and dashed lines for 50 and 25 nm mean diameter, respectively.

with sizes around 10 nm compared to nanoparticles with smaller and larger sizes, one would expect a larger number of sputtered atoms for the particles sized ∼ 10 nm. But in fact, the probability of an ion impact on nanoparticles is decreasing with decreasing nanoparticle size, which compensates the enhanced sputter yields of small nanoparticles and conserves the quadratic dependence of sputtered atoms on the particle diameter. The quadratic dependence is due to the nanoparticle's cross section dependence (more accurate the solid angle Ω, see following paragraph) on the square of the nanoparticle diameter.

The number of collected atoms as a function of the initial nanoparticle diameter is shown in figure 6.6b. As nanoparticles gain atoms by redeposition, collected atoms are also referred as gained atoms from the collecting nanoparticle's perspective. In figure 6.6b, the two simulated nanoparticle size regimes do not overlap. The total number of sputtered atoms is small for particle sizes distributed with a mean diameter of 25 nm. Therefore, the total amount of redeposited atoms has to be smaller than for larger mean nanoparticle diameters. The number of collected atoms also shows a quadratic relation to the nanoparticle diameter, as the quadratic fits show in figure 6.6b. The reason is the same as for the quadratic dependence of the sputtered atoms on the diameter.

How the particle size dependence of the sputter yield influences the redeposition is shown in figure 6.7a. Here, the ratio of nanoparticle diameters after and before irradiation is plotted as a function of the initial diameter. The depicted graph shows a distinct minimum at a diameter of ∼ 10 nm. The largest sputter yield appears at this diameter (see figure 5.4b). Therefore, the size differences before and after irradiation are largest. The ratio of the sizes after and before irradiation increases again with nanoparticle diameters

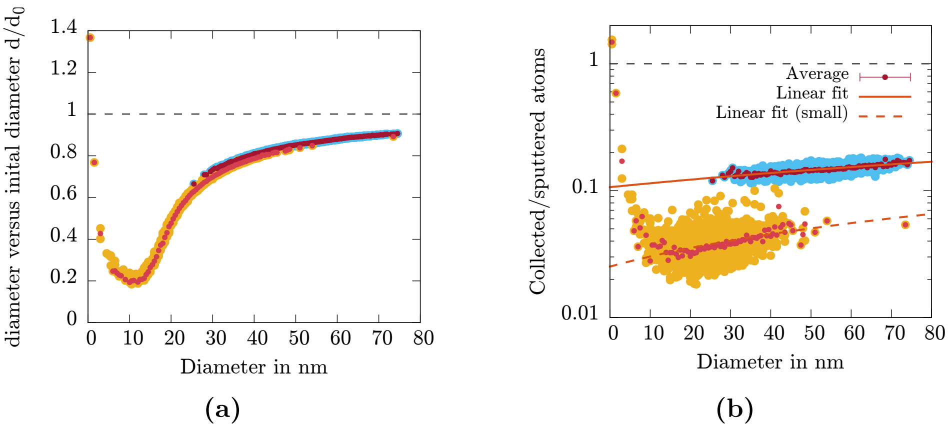

(a) (b)

Figure 6.7: (a) Fraction of the nanoparticle sizes after and before the simulated irradiation as a function of the initial nanoparticle size. Small nanoparticles with sizes smaller than 2 nm are growing because of the collection of atoms. (b) Ratio collected versus sputtered atoms as a function of the initial nanoparticle diameter. The simulations with a mean nanoparticle diameter of 50 nm show a linear behavior in the observed particle diameter range. The simulation results for size the distribution diameters with a mean diameter of 25 nm shows a linear behavior down to particle sizes of $\approx$ 10 nm, whereat the ratio of collected versus sputtered atoms is dramatically increasing for nanoparticle sizes smaller than 10 nm.

smaller and larger than 10 nm and reaches a value larger than 1 for initial nanoparticle diameters of $\sim$ 1 nm, which means growth of these particles. The sputter yield for such small nanoparticles shows a steep decrease with decreasing nanoparticle diameter. The ratio of diameters after and before irradiation increases to values between 0.8 and 0.9 for nanoparticle diameters larger than 40 nm due to an almost constant sputter yield for these diameters. The ratio of collected versus sputtered atoms is plotted as a function of the initial nanoparticle size in logarithmic scale in figure 6.7b. This plot results by dividing the data plotted in figure 6.6b by the data plotted in figure 6.6a. A large variation of the data points is visible for individual nanoparticles due to different sized neighboring particles in the array. This is discussed in detail in section 6.3. The ratio of collected versus sputtered atoms increases linearly with the nanoparticle diameter for particle sizes larger than 20 nm, as highlighted by the linear fits shown in figure 6.7b for both simulated size distributions. The fit of the size distribution with a small mean diameter shows a slightly larger slope compared to the fit of the data using a distribution with a large mean diameter. A totally different behavior show nanoparticles with diameters smaller than 20 nm as the ratio of collected versus sputtered atoms increases rapidly for such small particles. While the ratio of collected versus sputtered atoms is between 12 % and 18 % for nanoparticles with a size distribution with a mean diameter of 50 nm, the nanoparticles with a size distribution with a mean diameter of 25 nm reach values larger than 100 % for nanoparticle sizes of $\backsim$ 1 nm. Nanoparticles with a diameter of $\sim$ 1 nm can therefore grow by redeposition as collected material compensates their own sputtering. Such small nanoparticles were not investigated experimentally within this thesis, because of the relatively low resolution of the used SEM. Also the influence of these nanoparticles on others in terms of redeposition is insignificantly small, as figure 6.6a shows. Therefore, this effect is negligible for experimental observations.

Analytical estimate of the competition of collection and sputtering of atoms
In order to understand the results shown in figures 6.7a and 6.7b, the probabilities of atoms to get sputtered from one nanoparticle and get redeposited on another need to be considered.

A sketch underlining the following considerations is shown in the inset of figure 6.8a. Let's assume a particle 1 with radius R_1 sputters atoms, in the following referred as sputtering particle. A particle 2 with radius R_2 can possibly collect these sputtered atoms, which is from now on also called collecting particle. In the following it is assumed that the sputtering of atoms is isotropic. A measure for the probability of a sputtered atom getting collected by a nanoparticle is the solid angle Ω covering along the direction of this atom. The solid angle is defined as $\Omega = {}^{A}/_{d^2}$, where $A = \pi \cdot R_2^2$ is the cross section area of particle 2 and d the projected center-to-center distance of the two particles as it is defined in the simulation. From the schematic inset in figure 6.8 it is apparent that the actual center-to-center distance between the two particles is d'. This leads to a solid angle of $\Omega = {}^{A}/_{d'^2}$ for this case, and therefore

$$\Omega(R_1, R_2, d) = \frac{\pi \cdot R_2^2}{d^2 + (R_2 - R_1)^2}. \tag{6.1}$$

Figure 6.8a shows the solid angle calculated by equation 6.1 for a radius $R_1 = 50\,\text{nm}$ and various radii R_2 ranging from 5 to 50 nm as a function of the interparticle distance. It is obvious that the solid angle decreases inverse quadratic with the distance between the particles. In total, larger nanoparticles cover a larger solid angle for all calculated distances. Figure 6.8b shows the solid angle covered by particle 2 as a function of the collecting particle's radius for a projected interparticle distance $d = 95\,\text{nm}$. The solid angle is larger for larger radii R_1, although the difference is significant only for collecting particle diameters larger than 50 nm. A measure for the probability of a nanoparticle to sputter atoms is it's cross section area A weighted with the normalized sputter yield Y_n (normalized to the maximum). The comparison of both described probabilities explains the behavior in figure 6.7b and leads to a function f, which describes the ratio collected versus sputtered atoms:

$$f = \frac{\Omega(R_1, R_2, d)}{Y_n \cdot A(R_1)} = \left(\frac{R_2}{R_1}\right)^2 \frac{1}{Y_n \cdot (d^2 + (R_2 - R_1)^2)}. \tag{6.2}$$

Figure 6.9 shows the function f plotted versus the radius of the collecting particle for various radii of the sputtering particle. The interparticle distance for these calculations

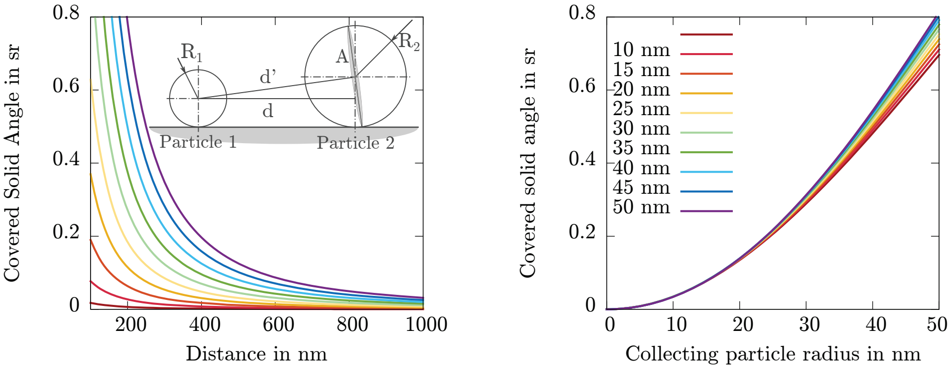

(a) (b)

Figure 6.8: Covered solid angle Ω of a nanoparticle in direction of a sputtered atom as a function of interparticle distance (a) and the nanoparticle size of the collecting nanoparticle (b). The different colors depict different radii of the sputtering nanoparticles ranging from 5 to 50 nm as shown in the legend of (b). The legend is the same for both figures. The inset in figure (a) shows the schematic illustration for deriving equation 6.1. Particle 1 emits atoms by sputtering, which get possibly redeposited on particle 2. Here, R_1 and R_2 are the radii of the respective nanoparticles, d' is the center-to-center distance of the nanoparticles, while d represents the projection of d'. The covered area of particle 2 is A.

was set to 95 nm. The trends of the calculated curves are similar to the average data points shown in figure 6.7b for small particles. The minima of the calculated curves match the maximum of the sputter yield (figure 6.9). However, the minima of the analytic curves are slightly shifted towards smaller nanoparticle diameters compared to the minimum of the simulation results depicted in figure 6.7b. It is also noticeable that the absolute value of the minimum is increasing with decreasing sputtering particle size. This was not investigated in the simulations. The ratio of collected versus sputtered atoms is increasing for nanoparticle radii smaller and larger than 3.8 nm. The trend for smaller particle radii than 3.8 nm is comparable to the simulation results. For particle radii larger than the minimum, the curve shows a linear increase in the simulations. In contrast, the analytically calculated curve shows an inverse quadratic behavior, as can be concluded from equation 6.2 with a maximum around the radius of the sputtering particle radius. The curves for different sputtering particle diameters intersect at a radius of ~ 15 nm. The ratio of collected versus sputtered atoms is larger for large sputtering particle sizes for collecting particle radii larger than 30 nm. This result is in line with the simulations for the two different simulated particle size distributions. For diameters larger than this maximum, the ratio of collected versus sputtered atoms is decreasing again almost linearly.

The trend of the modeled curves can be explained by the competition of both effects, sputtering and redeposition. On one hand, the probability of collecting atoms by redeposition is decreasing with decreasing particle size. On the other hand, the probability of emitting atoms by sputtering is decreasing in the same way. However, for small particle

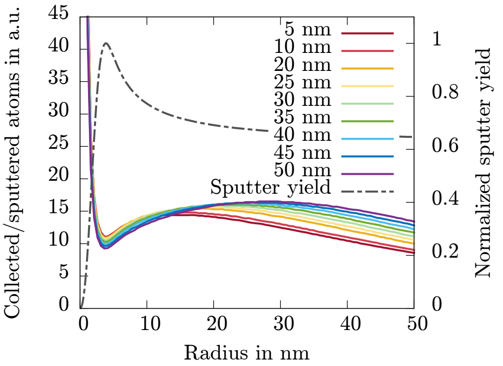

Figure 6.9: Calculated qualitative ratio of collected versus sputtered atoms as a function of the radius of the collecting particle in arbitrary units from equation 6.2. Different colors show the result for different radii of the sputtering particle. The dashed line shows the normalized sputter yield based on Järvi's model [51].

sizes, the size dependence of the sputter yield is the key factor of the above described behaviour, which moderates which effect is dominant. While the sputter yield is almost constant for particle diameters larger than 40 nm, it changes it's behavior dramatically for particle diameters smaller than 40 nm. The size dependence of the sputter yield changes for particle diameters smaller than 7.6 nm in favour of the redeposition effect due to its steep decrease with decreasing particle size. For particle diameters between 7.6 and 40 nm, the sputter yield is the dominating factor in the model described by equation 6.2. The presented analytic calculation is fairly simple. Some important effects, which are implemented into the simulations, are neglected and might explain the qualitative differences between simulation results and analytic calculations. First, the emission of sputtered atoms is highly anisotropic, as shown in section 4.3. Since sputtered atoms leave a nanoparticle preferably in direction of other nanoparticles in polar direction, the redeposition is expected to be higher than predicted by the analytic calculations, especially for large nanoparticles. Secondly, the analytic calculations just consider two nanoparticles. The neighborhood of various particles with different sizes plays a role of the amount of redeposited atoms on a certain particle in the simulations. The MC simulations solve the (unknown) more detailed analytical equations by using random numbers. However, the simple analytic calculations presented here helps to understand the basic competition of the sputtering and redeposition effects and how they influence each other.

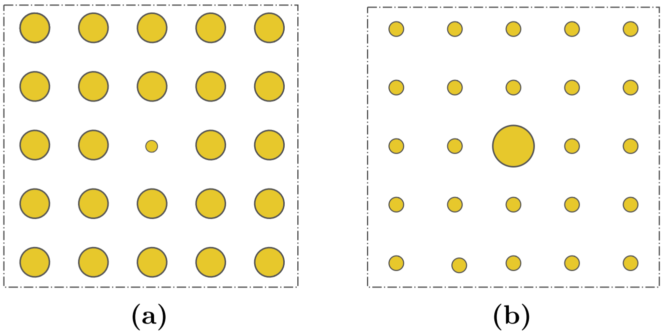

Figure 6.10: Schematic illustrations of 5 × 5 square nanoparticle array situations simulated to investigate the influence of neighboring nanoparticle sizes on the redeposition. For two special cases, the central nanoparticle size was varied between 1 nm and 90 nm, while the surrounding particles had a constant size. (a) A central nanoparticle is surrounded by equally sized nanoparticles with a diameter of 50 nm. (b) The central nanoparticle is surrounded by equally sized nanoparticles of 20 nm in diameter

6.3 Neighborhood dependence

Simulation details Simulations with two different model systems were performed to understand the role of different sized neighbors on a nanoparticle in terms of redeposition. A central nanoparticle was surrounded by two different groups of nanoparticles on a 5 × 5 array, as shown in top-view in figure 6.10. The surrounding nanoparticles had two different diameters, 20 nm or 50 nm, referred in the following as small and large neighboring nanoparticles, respectively. The nanoparticle diameters were equal within the groups. The diameter of the central particle was varied from 1 to 90 nm in each case. The size of the cells hosting the nanoparticles was set to 95 nm for both situations. The ion species was Ga^+ with an energy of 25 keV and a fluence of $3 \cdot 10^{15}$ atoms/ion.

Simulation results Figure 6.11a shows the diameter of the central particle after irradiation as a function of it's initial diameter. In general, the diameter of the central nanoparticle changes its size similar irrespective on the size of the neighboring particles, whereat the diameter of the central particle is slightly larger in case of large neighboring particles. This fact is more visible in the inset of figure 6.11a, which shows the diameter of the central nanoparticle after irradiation in logarithmic scale. This leads to the conclusion that small neighboring nanoparticles promote a faster erosion of the central nanoparticle. Figure 6.11b shows the ratio of diameter of the central nanoparticle after irradiation versus the initial diameter as a function of the initial central particle diameter. The difference between the two simulated situations is largest for nanoparticle sizes smaller than 10 nm. The growth of nanoparticles with diameters around 1 nm is only possible in vicinity of large nanoparticles.

The ratio of collected versus sputtered atoms is shown in figure 6.11c as a function of the

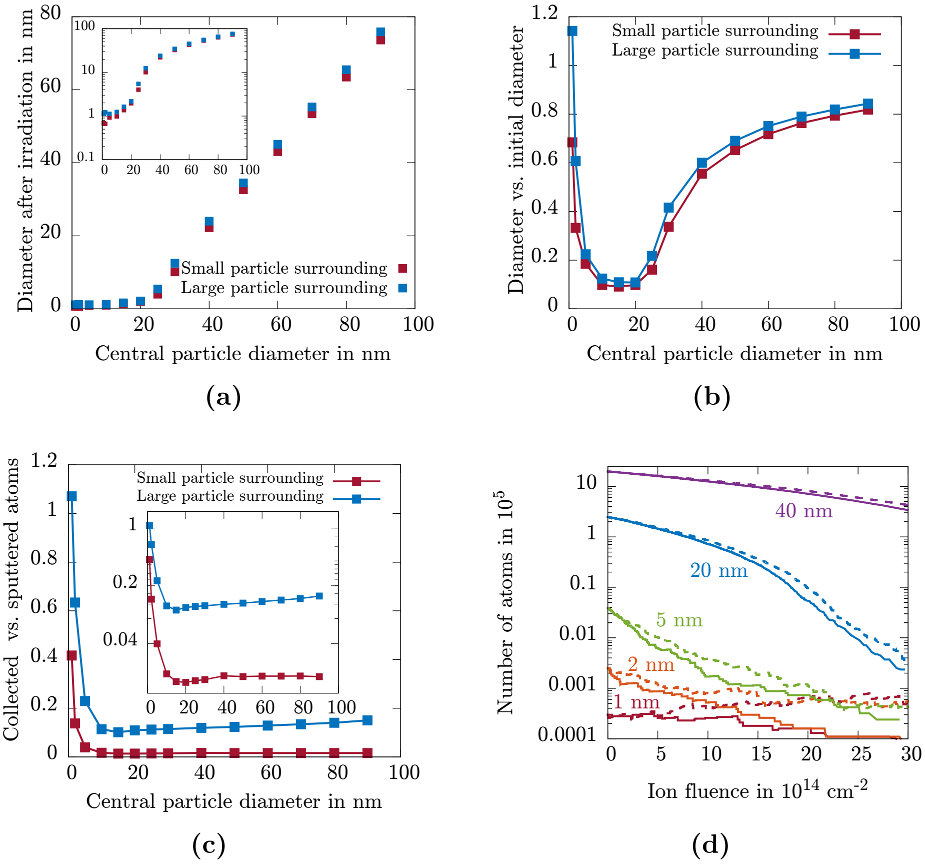

(a)

(b)

(c)

(d)

Figure 6.11: (a) Diameter of the central nanoparticle as a function of its initial diameter for small (red) and large nanoparticle neighborhood (blue). The color coding is the same for all graphs in this figure. The inset shows the graph in logarithmic scale. (b) Ratio of the central nanoparticle size after and before irradiation as a function of its initial diameter. (c) Fraction of collected vs. sputtered atoms of the central nanoparticle as a function of the initial central particle diameter. The inset shows the graph in logarithmic scale. (d) Number of atoms as a function of ion fluence for various central particle diameters: 1 nm (red), 2 nm (orange), 5 nm (green), 20 nm (blue) and 40 nm (purple). Solid lines show the simulation results for small nanoparticle neighbors, dashed lines for large neighbors.

central particle diameter. The difference between both groups of neighbors is best visible here. The ratio of collected versus sputtered atoms is about one order of magnitude larger for large neighboring particles compared to small ones. The minima of both curves are at the same initial central particle diameter of 10 nm. It becomes apparent that the slope of the data points is larger for large particle surroundings, compared to small ones, when taking a look at the linear regime of the plot for central particle diameters larger than 10 nm. Nanoparticles, which are smaller than 10 nm in diameter, profit most from redeposition, as they compensate more of their sputtered material than large nanoparticles. The ratio steeply increases for even smaller central nanoparticle sizes.

The evolution of the number of atoms of five central nanoparticle sizes over the ion fluence is shown in figure 6.11d for both groups of neighboring particle sizes. All nanoparticles decrease in size with increasing fluence, except the nanoparticle with a diameter of 1 nm for large neighboring particles. The 1 nm sized nanoparticle gradually grows with increasing ion fluence after $5 \cdot 10^{14}\,{}^{\text{ions}}/_{\text{cm}^2}$, because the collecting versus sputtering ratio is > 1. The deviation of the number of atoms for the 2 nm sized nanoparticle between small and large neighboring particles is significant after $1 \cdot 10^{15}\,{}^{\text{ions}}/_{\text{cm}^2}$. Nevertheless, the average slope of the number of atoms of the 2 nm sized central particle is negative even for large neighboring particles, which means it shrinks. Both central particles with 1 and 2 nm in diameter vanish after $\sim 2.1 \cdot 10^{15}\,{}^{\text{ions}}/_{\text{cm}^2}$ with small neighboring nanoparticles. Already for slightly larger nanoparticle diameters, e.g. 5 nm, sputtering is the dominating effect and the particles shrink significantly for both small and large neighboring particles, as shown in figure 6.11d. The difference between the curves for small and large nanoparticles decreases with increasing central nanoparticle size.

6.4 Experiment vs. simulation

Simulation details The *in situ* experiment on a nanoparticle array presented in section 5.2 was modeled using the MC redeposition code. The simulation volume was represented by one cuboid cell with a squared base with a side length of 550 nm. The position of the nanoparticles was extracted from the SEM images and used as (x, y) positions inside the cell. The cell height was defined as the maximum diameter of the nanoparticles, which were also derived from the SEM images. The simulated ion fluence of 25 keV Ga^+ ions was $5 \cdot 10^{15}\,{}^{\text{ions}}/_{\text{cm}^2}$. Scaled Järvi's model was in use as sputtering model. Periodic boundary conditions were applied in x and y direction. The difference of the sputter yields of 25 and 30 keV Ga^+ ions are negligible (compare sections 4.2 and 5.1), therefore the simulation and experimental results are comparable.

Simulation results Figure 6.12 shows the comparison of both experimentally obtained SEM images and images produced by the simulation for three selected ion fluencies. Three nanoparticles, which are of major interest for the discussion, are marked with red circles. Particles 1 and 2 have almost equal sizes before irradiation, while particle 3 in the center of the image is the largest nanoparticle investigated in this experiment. Particle 1 decreased in size after a fluence of $3.3 \cdot 10^{15}\,{}^{\text{ions}}/_{\text{cm}^2}$, whereat particle 2 already completely vanished. Particle 3 showed a small size decrease compared to particles 1 and 2.

Two possible mechanisms may describe the different sputtering rates of equally sized nanoparticles: 1. Greaves *et al.* [34] showed that the sputter yield depends on the angle of the ion beam direction with respect to the crystal lattice direction. Small angles may lead to channeling, reduced energy deposition by the ion and therefore reduced sputtering. If the ion beam direction is in direction of a low index axis of particle 1, the sputter yield would be reduced at low ion fluences. 2. Redeposition of sputtered material from

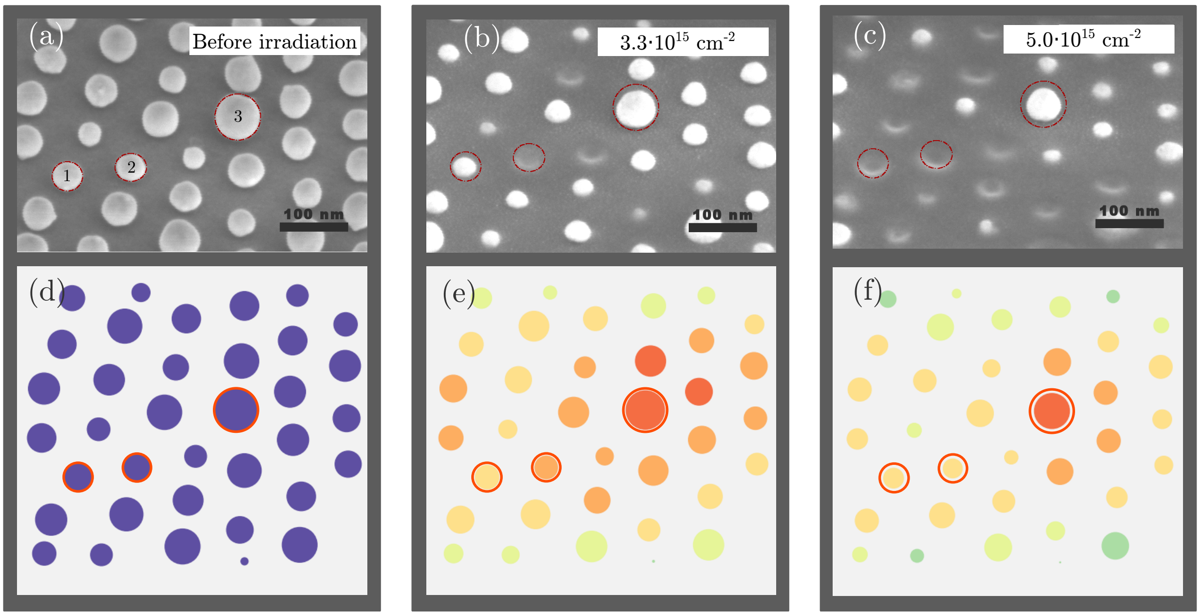

Figure 6.12: (a) – (c) SEM images and (d) – (f) images obtained by the MC simulations for an ion irradiated Au nanoparticle array. The total fluence irradiated was $5 \cdot 10^{15}\ \mathrm{ions}/\mathrm{cm}^2$. The initial state is shown in the left column. The middle column shows the state after a fluence of $3.33 \cdot 10^{15}\ \mathrm{ions}/\mathrm{cm}^2$, while the right column shows the final state after the irradiation. The sputter model used for the simulation was the scaled Järvi model. The colors in figures (e) and (f) indicate the relatice amount of redeposited atoms on the respective nanoparticles ranging from red (high) to green (low).

surrounding particles might slow down the erosion of particle 1 compared to particle 2. Since particles 1 and 2 have differently sized neighbors, they might gain a different amount of atoms which leads to the different erosion rates. This effect would be more pronounced on particle 3 due to its large size.

Qualitative results obtained by the MC simulation performed with the experimental parameters are shown in figures 6.12d to 6.12f as a function of the ion fluence. It is obvious that the size decrease of the nanoparticles in the simulation is much smaller. After an ion fluence of $3.3 \cdot 10^{15}\ \mathrm{ions}/\mathrm{cm}^2$, both particles 1 and 2 are still present in the simulated situation, while particle 2 already vanished in the experiment. After $5.0 \cdot 10^{15}\ \mathrm{ions}/\mathrm{cm}^2$, most of the particles vanished in the experiment, while all simulated particles remained and decreased relatively little in size compared to the experiment. Most interestingly, particle 1 and 2 seem to erode with almost the same rate with increasing fluence. The simulation was repeated by using Järvi's model, which lead only to a minor difference in the result.

A quantitative analysis of the simulation results is shown in figure 6.13. Figure 6.13a shows the relative number of atoms with respect to the initial number of atoms as a function of ion fluence for the three particles marked in figure 6.12. Experiment and simulation results show a comparable rate of size decrease over the ion fluence for all three nanoparticles. The experimental data of both particles 1 and 2 show a fast size

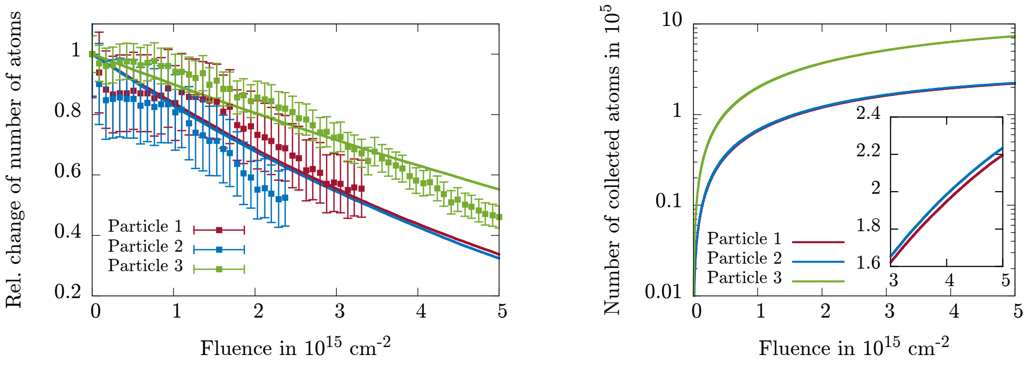

(a) **(b)**

Figure 6.13: (a) Relative change of the number of atoms of the three nanoparticles marked in figure 6.12 as a function of ion fluence. Particles 1 and 2 are shown in red and blue, respectively, particle 3 is shown in green. The solid lines show the MC simulation results. (b) Number of collected atoms as a function of ion fluence, plotted in logarithmic scale. The inset shows the number of collected atoms for particles 1 and 2 in detail for fluences between 3 and $5 \cdot 10^{15}$ ions/cm² in linear scale.

decrease at the beginning with a phase of seemingly no size decrease for $\sim 1 \cdot 10^{15}$ ions/cm². After $1 \cdot 10^{15}$ ions/cm², the size decrease of particles 1 and 2 is slightly faster compared to the simulation, although the error bars of the experimental data are relatively large and overlap. Particle 2 could not be evaluated after an ion fluence of $2.4 \cdot 10^{15}$ ions/cm² due to particle-substrate interactions, particle 1 was not evaluated after $3.3 \cdot 10^{15}$ ions/cm². Particle 3 could be analyzed experimentally over the whole irradiated fluence. Experiment and simulation are in line up to a fluence of $3.9 \cdot 10^{15}$ ions/cm². The reasons for the discrepancy of experiment and simulation, especially for the abrupt disappearing of particles 1 and 2 in figure 6.13a, can be explained by the simple assumptions made in the simulations, like negligence of particle-substrate interaction and the simple implemented sputtering model. Especially particle-substrate interactions hinder the evaluation of the nanoparticles experimentally. The nanoparticles descend into the substrate in the experiment, as shown in section 5.3.

Figure 6.13b shows the number of collected atoms of the three nanoparticles in logarithmic scale as a function of the ion fluence obtained by the simulation. The number of collected atoms is increasing over the fluence for all particles. Particle 3 collects almost one order of magnitude more atoms than the other two particles. The number of collected atoms is almost equal for particles 1 and 2, whereat particle 2 gains slightly more atoms than particle 1, as shown in the inset of figure 6.13b for the ion range from $3 \cdot 10^{15}$ to $5 \cdot 10^{15}$ ions/cm². Therefore, particle 2 should erode slightly slower than particle 1 according to the simulation, although the number of redeposited atoms is small compared to the number of sputtered atoms.

The results of the MC simulation show that redeposition cannot explain the different erosion rates of equally sized nanoparticles in the experiment. Hence, most likely the channeling effect is responsible for the experimental observations of different erosion rates.

6.5 Summary

A dynamic MC simulation code was developed to model the interaction of 25 keV Ga^+ irradiated Au nanoparticles ordered in an array in terms of redeposition of sputtered atoms. The nanoparticles in the array showed a Gaussian size distribution, which was conserved after the irradiation in any case. The mean diameters after irradiation with and without redeposition in the simulation matched the experimental mean diameters within the simlation and experimental error. The amount of redeposited material appeared to be diameter dependent and was on average $10 - 20\,\%$ with respect to the amount of sputtered material for nanoparticle diameters larger than 30 nm. The redeposition is minimal for diameters with a maximum sputter yield and steeply increases for decreasing nanoparticle diameters. Nanoparticles with diameters of ~ 1 nm can grow during irradiation due to redeposition.

Redeposition affects mainly nanoparticles with diameters smaller than 5 nm, when the neighboring particles are large enough to provide a sufficient amount of material by sputtering. On one hand, the surrounding nanoparticles need to be large enough to receive enough ion impacts to emit enough atoms. On the other hand, small nanoparticles need to be small enough to have a small chance to get hit by ions, and if so, to have a small sputter yield that they can grow by collecting atoms. Only in case of large neighboring nanoparticles, 1 nm sized nanoparticles can grow due to redeposition.

The developed MC simulation described the *in situ* experiment with a nanoparticle array (see section 5.2) well to the point, where particle-substrate interaction made nanoparticle and substrate indistinguishable by image analysis. The simulation revealed that the different sputtering rates of equally sized nanoparticles could not be explained by redeposition effects. Most likely ion channeling and other thermally driven effects lead to different sputter rates [34].

7 | Nanostructuring of lithium niobate

This chapter presents the results for structuring $LiNbO_3$ using ion beam irradiation and self organized grown nanostructures as irradiation mask material instead of conventional masks produced by electron beam lithography. The masks were Au nanoparticles, grown by the technique described in section 3.2.2, and imprinted zinc oxide (ZnO) nanowires. The masks were succesfully transferred into the $LiNbO_3$ by IBEE using Ar^+ and Kr^+ ions of various energies and fluences. The $LiNbO_3$ structures became even more pronounced after annealing and a second irradiation and etching step. The $LiNbO_3$ samples with the Au nanoparticles, which were used for the experiments presented in this chapter, were produced by the group of Claudia Pacholski at the MPI for Intelligent Systems in Stuttgart and the Institute for Physical Chemistry at the University of Heidelberg. The $LiNbO_3$ wafers for the sample preparation were delivered by CrysTec GmbH and Crystal GmbH. The experiments presented here were performed and evaluated in collaboration with Sven Bauer in the scope of his master's thesis [54].

7.1 Simulation results and irradiation parameters

Simulation setup Simulations were performed using *iradina* to estimate the ion energy and fluence for a sufficient damage of uncovered areas of $LiNbO_3$ as deep as possible for subsequent etching, while preferably keeping the damage in the covered areas low. Equation 3.1 gives the critical normalized fluences for the IBEE process of 0.15 and 0.08 for Ar^+ and Kr^+ ions, respectively.

The simulation setup in case of a Au nanoparticle was a sphere lying on a cuboid substrate, as shown in figure 7.1a. The sphere was centered in y and z direction and the ion beam impinged in x direction perpendicular to the substrate's surface. A cylinder, which was centered in y direction, represented the nanowire in the simulation. The length of the cylinder was equal to the length of the simulation volume in z direction (compare figure 7.1a). The simulation was performed by using a cell size of 2 nm in all directions and PBC's were applied in y and z direction in order to emulate bulk. The substrate had a total length of 300 nm in x direction. The width of the simulation volume was defined by the diameter of the simulated Au nanoparticle; the simulated diameters were 50 and 250 nm with a respective simulation volume width of 100 and 290 nm. The simulated ion energies ranged from 50 to 350 keV for each ion species and the number of simulated ions

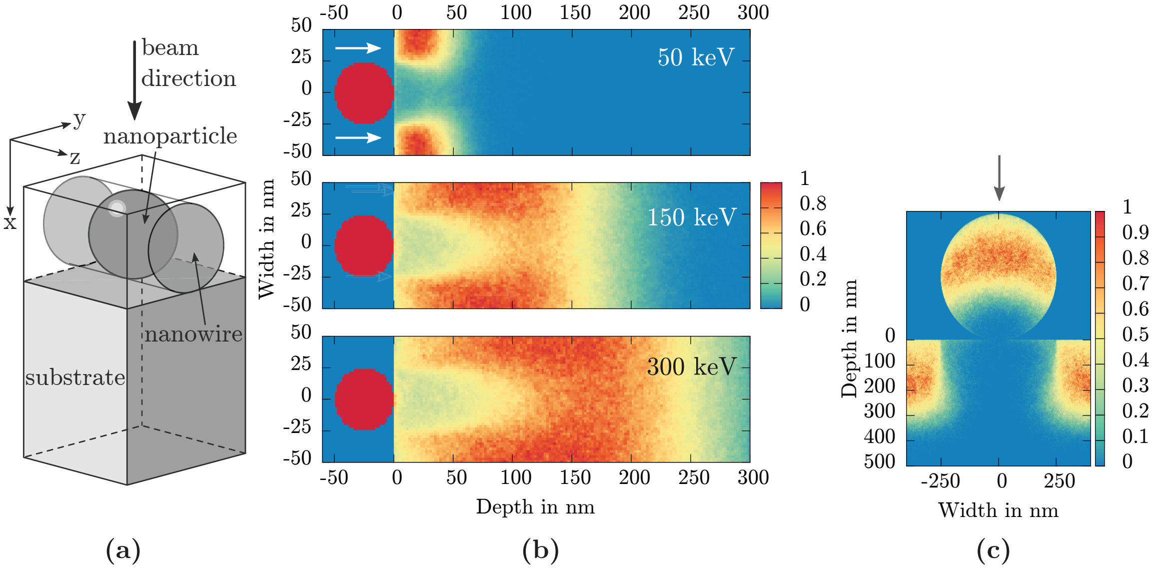

Figure 7.1: (a) Schematic illustration of the simulation volume. (b) – (c): Damage maps (n_{dpa}) of Ar$^+$ ion irradiated LiNbO$_3$ for different simulation setups obtained by *iradina* simulations. The maps show the cross section in the $x - y$ plane of the simulation of the center of the simulation volume for different mask structures. The arrows indicate the ion beam direction. (b) n_{dpa} underneath a spherical Au nanoparticle with a diameter of 50 nm for different Ar$^+$ ion energies: 50 keV (top), 150 keV (middle) and 300 keV (bottom). (c) n_{dpa} underneath a cylindrical ZnO nanowire with a diameter of 500 nm irradiated with 350 keV Ar$^+$ ions.

was set to 500 000. A similar simulation setup was used to simulate the irradiation of LiNbO$_3$ with zinc oxide (ZnO) nanowires as mask martial on top. The nanowire diameter was set to 500 nm, while the depth of the LiNbO$_3$ substrate was set to 600 nm.

Simulation results The simulation results for Ar$^+$ irradiation of the LiNbO$_3$ covered with 50 nm sized Au nanoparticles is shown in figure 7.1b for ion energies of 50 (top), 150 (middle) and 300 keV (bottom) as a map of n_{dpa} over the cross section of the simulation volume. The n_{dpa} of the nanoparticle was set to 1 to improve the visibility on the substrate. The damage increases over the depth with increasing ion energy due to the larger ion range. The substrate shows significantly lower damage underneath the nanoparticles. However, a damaged band forms ~ 100 nm underneath the nanoparticles for ion energies larger than 100 keV. The damage in the band is high enough to be etched by HF for ion energies larger than 150 keV. This would result in a complete removal of the top layer of LiNbO$_3$ in the etching step of the IBEE process without conserving the desired geometry of the nanostructures. Therefore, only ion energies smaller than 150 keV were used in the experiments using 50 nm Au nanoparticles as masks. The region underneath the nanoparticles shows a sufficiently low n_{dpa}, smaller than 0.25, to endure the etching step. An energy-fluence series was simulated (also for other Au nanoparticle diameters) in order to achieve a homogeneous damage profile over the depth in the uncovered areas and preferably steep edges of the structures. The expected structure height after etching is ∼ 80 nm. The used energies and fluences are shown in table 7.1.

Additionally, simulations were performed using Kr^+ ions, since they are also possible projectile candidates for the IBEE process, as the ion range of Kr^+ in $LiNbO_3$ is lower due to it's higher mass. Therefore, higher ion energies need to be used to achieve comparable n_{dpa} over depth with the same mask structure. The energies and fluences obtained by these simulations are also shown in table 7.1.

Figure 7.1c shows the simulated damage over the cross section of the simulation volume for 350 keV Ar^+ ion irradiation of $LiNbO_3$ with a 500 nm ZnO nanowire mask. The ZnO stops the ions almost completely, which results in an almost undamaged area underneath the nanowire. The Ar^+ ions can damage the $LiNbO_3$ up to a depth of 300 nm with the used ion energy. In comparison, Kr^+ ions with the same energy would lead to a comparable result in a depth of 250 nm, without damaging the material directly underneath the mask significantly. Therefore, ZnO nanowires are suitable as masks for IBEE. The irradiation parameters were the same as for 250 nm Au nanoparticles, shown in table 7.1.

The sputter yields of the simulations discussed above are shown in table 7.1 for the respective ion species and energies. The sputter yields are between 5 and 18 $^{\text{atoms}}/_{\text{ion}}$. This would result in ∼ 1% loss of the mask material with the aimed ion fluences, which results in an insignificant size decrease of the masks. Even a two times larger sputter yield is considered (as would be expected from the results of previous chapters), the size decrease is negligible if no thermally driven effects appear in the experiments.

7.2 Nanostructures in lithium niobate

Au nanoparticle masks The IBEE process was first applied to samples with 50 nm Au nanoparticle masks with an interparticle distance of 10 nm. A typical SEM image of such a sample is shown in the top image of figure 7.2a. The empty spaces on the substrate as well as the small interparticle distance can be accounted to the patterning process of the nanoparticles, which was optimized for Si substrates and did not work ideal on $LiNbO_3$. The sample was irradiated with Ar^+ ions using the parameters shown

Table 7.1: Irradiation parameters for the IBEE process using nanoparticles (NP). The samples cylindrical ZnO nanowires were irradiated with the same parameters as the 250 nm Au nanoparticles. The parameters are ion species, ion energy E, fluence ϕ and sputter yield Y.

Mask	*50 nm Au NP*				*100 nm Au NP*		*250 nm Au NP*		
Ion species	Ar^+		Kr^+		Ar^+		Ar^+		
E [keV]	40	120	60	200	30	200	30	150	350
ϕ [cm^{-2}]	2.4e13	2.0e13	8.0e12	5.2e1013	1.7e13	2.0e14	4.4e13	3.2e13	2.6e14
Y [at/ion]	9.8	7.6	17.7	17.3	6.4	7.0	5.1	6.2	5.6

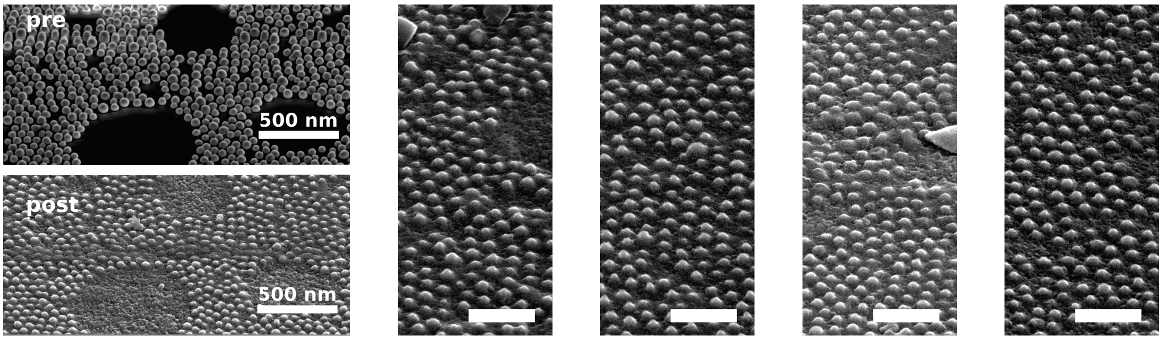

(a) (b) (c) (d) (e)

Figure 7.2: (b) SEM images of x cut $LiNbO_3$ samples before (top) and after (bottom) the IBEE process. The used ion species was Ar^+ with a maximum energy of 120 keV. The masks on top of the substrate were 50 nm sized Au nanoparticles. (b) – (e): SEM images of $LiNbO_3$ samples after the IBEE process irradiated with different ion species on different $LiNbO_3$ substrates. (b) Ar^+, x cut $LiNbO_3$, (c) Ar^+, z cut $LiNbO_3$, (d) Kr^+, x cut $LiNbO_3$, (e) Ar^+, z cut $LiNbO_3$. The scale bar in figures (b) – (e) represents 250 nm. All SEM images were taken under an angle of 52 ° to the surface normal.

in table 7.1. The bottom image of figure 7.2a shows the same position after the IBEE process. Small hillocks at the positions of the nanoparticles are visible. The diameters at the base of the hillocks are the same as the diameters of the nanoparticle masks. Pillar shaped nanostructures are expected from the simulation results shown in the previous section. However, the damage directly beneath the nanoparticles must have extended n_{dpa}^{crit}, so that $LiNbO_3$ on the top edges of the structures was etched away. Another noticeable effect is the roughening of the uncovered areas. A reason for this might be a heterogeneous defect distribution over the irradiated area. Ion beam irradiation is a statistical process, which can result in a different number of ions impinging on different area fractions at low fluences. Therefore, some parts of the substrate would be etched more than others, because the etching rate strongly depends on the defect concentration [123]. There were no Au mask residuals left on the sample surface, as EDX measurements with 15 keV showed. The EDX spectra (not shown here) of the investigated samples also showed the Kα line of carbon (C), which is a residual of carbon evaporation for SEM imaging. For details about the EDX investigations of the samples the reader is referred to the master's thesis of Sven Bauer [54].

A comparison of the produced $LiNbO_3$ nanostructures by different ion species and different $LiNbO_3$ substrates after the IBEE process with Ar^+ and Kr^+ ions and x and z cut $LiNbO_3$ substrate is shown in figures 7.2b to 7.2e. The structures look similar and no significant difference between different ion species and substrate types is visible. Cross sections of the structures after the IBEE process were produced by FIB to analyze the shape of the structures in detail. The cross sections are shown in figure 7.3a and show random cuts through the structures. Some structures show the pillar shape, which are expected from the simulation. Several cross sections on random positions of the samples were

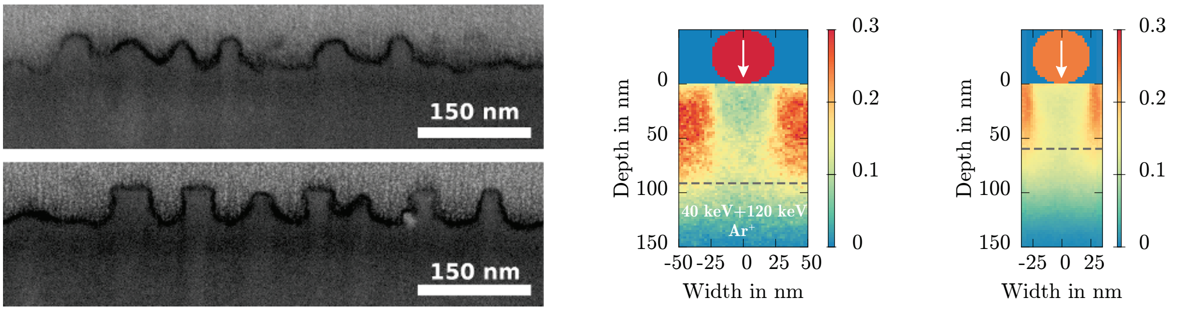

(a) **(b)** **(c)**

Figure 7.3: (a) Representative SEM images of cross sections of $LiNbO_3$ samples with x (top) and z cut (bottom) $LiNbO_3$ substrate after Ar^+ IBEE with 50 nm sized Au nanoparticles masks. The images were taken under an angle of 52 ° to the surface normal. (b) Simulation results of the irradiation of $LiNbO_3$ with $2.4 \cdot 10^{13}\,\mathrm{ions/cm^2}$ 40 keV and $2.0 \cdot 10^{14}\,\mathrm{ions/cm^2}$ 120 keV Ar^+ ions with a mask of 50 nm sized Au nanoparticles. The figure shows a map of n_{dpa} over the cross section of the simulation volume. The arrow indicates the ion beam direction. The dashed line is at a depth of 90 nm beneath the surface, where the n_{dpa} is smaller than n_{dpa}^{crit}. (c) The simulation with the same irradiation parameters, but for an interparticle distance of 10 nm. The defect concentration exceeds n_{dpa}^{crit} only in depths 60 nm beneath the surface.

produced and the heights of 8 – 16 nanostructures were measured. The structures on the x cut substrates had an average height of (58.7 ± 9.1) nm, while the average height of the structures on z cut substrates was (62.4 ± 4.1) nm. The nanostructres produced by Kr^+ irradiation had an average height of (59.6 ± 6.0) and (63.9 ± 6.8), for x and z cut $LiNbO_3$, respectively. The structure height is therefore independent of the $LiNbO_3$ cut direction and the used ion species. Thus, the measured structure height differs from the simulated height (~ 90 nm) for the irradiation series for the Ar^+ irradiation, as shown in figure 7.3b for a particle with a simulated interparticle distance of 50 nm. The simulation was repeated with the same energies for a smaller simulation volume, which corresponds to the interparticle distance of 10 nm observed in the experiment. The defect concentration map of this simulation is shown in figure 7.3c. The defect concentration exceeds n_{dpa}^{crit} only in depths below ~ 60 nm, which fits the experimental results almost perfectly. The screening of the substrate is larger with masks showing a smaller interparticle distance compared to larger distances. Additionally, the simulated defect concentration underneath the nanoparticles is larger for an interparticle distance of 10 nm compared to the results for an interparticle distance of 50 nm. Ions, which impinge on the edge of a particle deposit less energy inside the particle and are preferably scattered into the substrate underneath the particle. Since the number of simulated ions was the same for both simulations, the total irradiated area was smaller for an interparticle distance of 10 nm and the "edge area" of nanoparticles was larger with respect to the total area. Thus, the substrate underneath the nanoparticles with a smaller interparticle distance shows a seemingly larger damage. The experiment was repeated with commercial Au nanoparticles on $LiNbO_3$ with interparticle distances larger than

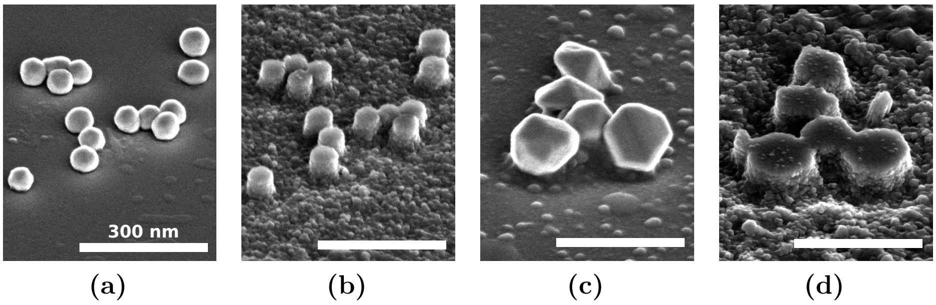

(a) (b) (c) (d)

Figure 7.4: SEM images of x cut $LiNbO_3$ substrates before irradiation with (a) 100 nm and (c) 250 nm sized Au nanoparticles on top. Figures (b) and (d) show the respective substrates after the IBEE process. The scale bar shows the same length in all images.

100 nm without a specific order to verify the screening effect. The average height of the $LiNbO_3$ nanostructures of these nanostructures was $\sim$ 80 nm, which confirms the simulation results with an interparticle distance of 50 nm and proves the shadowing effect of nanoparticle masks with small interparticle distances.

The experiments described above were repeated using Au nanoparticles with diameters of 100 and 250 nm. Commercial Au nanoparticles were deposited on $LiNbO_3$ substrates without a specific order. The irradiation parameters are shown in table 7.1. Figures 7.4a and 7.4c show SEM images of nanoparticles with a diameter of $\sim$ 100 nm and $\sim$ 250 nm on $LiNbO_3$ before the irradiation, respectively. Figures 7.4b and 7.4d show SEM images of the respective positions on the $LiNbO_3$ substrate after the IBEE process. The structures obtained by larger masks are more defined than the structures produced by the 50 nm Au nanoparticle masks. The average heights of the structures are (81.0 ± 7.4) nm and (101.1 ± 13.8) nm for 100 and 250 nm nm sized Au nanoparticle masks, respectively. The top surface of the nanostructures are planar and smooth and the side facets are steep in both shown cases. The lateral sizes of the nanostructures match the sizes of the nanostructure masks. However, the side facets of the structures and the substrate seem rough. The reason for this might be the larger ion straggling in the depth compared to the surface-near region of the $LiNbO_3$ underneath the particle, which leads to defect concentration variations near the side facets in the $LiNbO_3$ and therefore to different etching results and roughening.

Repeated IBEE The $LiNbO_3$ nanostructure height is limited by the mask material and size, and therefore by the used ion species and energy. The height of the structures could not be increased further with 50 nm sized Au nanoparticles. An approach to increase the height of the produced structures was to repeat the IBEE process after annealing the samples after a first IBEE step, where the $LiNbO_3$ nanostructures itself would work as masks. The ions may be scattered at atoms in the $LiNbO_3$ nanostructure and inflict additional damage in the substrate around the structure, which leads to the assumption

that already existing $LiNbO_3$ structures can act as masks.
A simulation of pre-structured $LiNbO_3$ was performed in order to simulate the damage in the material in a subsequent irradiation after a first IBEE step using 50 nm Au nanoparticle masks. It was assumed that the $LiNbO_3$ structure is a cylinder with a half sphere on top after the first IBEE step, in the following also referred as "nano-pillar" (compare figure 7.5a). The height of the structure was set to 60 nm with a diameter of 50 nm. The width of the simulation volume in y and z direction was set to 60 nm with PBC's in both directions. The ion energy was varied between 40 and 120 keV. The simulated damage in a 120 keV Ar^+ irradiated cylindrical $LiNbO_3$ pillar shaped nanostructure on $LiNbO_3$ substrate is shown in figure 7.5a in a n_{dpa} map of the structure's cross section. It is apparent that the defect concentration inside the structure is ~ 0.75 times the defect concentration inside the substrate. A damage distribution, which allows etching of the substrate while conserving the pillar shape of the nanostructure, can be achieved in a small fluence intervall. An ion energy of 120 keV with a fluence of $1.5 \cdot 10^{14}\,{}^{\text{ions}}/_{\text{cm}^2}$ was obtained as optimal irradiation parameters for this experiment from simulations with different ion energies. The simulation results shown in figure 7.5a reveal a defect concentration below n_{dpa}^{crit} in the $LiNbO_3$ nano-pillar, because ions would be straggled in lateral direction and deposit only a small amount of energy inside the nanostructure. The ions would then deposit a major amount of their energy in the previously unmasked areas.
The samples were annealed for 30 min in air at a temperature of 400 °C after the first IBEE process, because $LiNbO_3$ recrystallizes at this temperature [150, 151]. If the temperatures rise above 400 °C, Li diffuses out and lithium triniobate ($LiNb_3O_8$) forms [152]. It is possible that small defect concentrations remain in the material, which makes it difficult to calculate the right fluence for the irradiation. Therefore, already processed samples (see previous paragraph) were irradiated with 120 keV Ar^+ ions with different ion fluences of $1.1 \cdot 10^{14}\,{}^{\text{ions}}/_{\text{cm}^2}$, $1.3 \cdot 10^{14}\,{}^{\text{ions}}/_{\text{cm}^2}$ $1.5 \cdot 10^{14}\,{}^{\text{ions}}/_{\text{cm}^2}$ and $1.7 \cdot 10^{14}\,{}^{\text{ions}}/_{\text{cm}^2}$. SEM images of z cut $LiNbO_3$ samples after a second IBEE step performed using 120 keV Ar^+ ions with an ion fluence of $1.7 \cdot 10^{14}\,{}^{\text{ions}}/_{\text{cm}^2}$ are shown in figures 7.5b to 7.5d. Comparing figures 7.5b and 7.5c, it is obvious that the nanostructures became more pronounced after the second IBEE step. This effect was visible for both Ar^+ and Kr^+ ions. Figure 7.5d shows cross sections of z cut $LiNbO_3$ nanostructures after the second IBEE step using 120 keV Ar^+ ions. The images were obtained on the same sample on different positions. Some structures became cone-shaped (top image), while some structures conserved their pillar shape (bottom image). This shows that the defect concentration on the outside of the nanostructure was still larger than n_{dpa}^{crit}, which led to the etching of these structures. The heights of the structures were (77.3 ± 5.0) nm and (85.9 ± 5.3) nm for Ar^+ and Kr^+ irradiation, respectively, which is an enhancement of ~ 20 nm in comparison to the heights after the first IBEE step. Nevertheless, these results are not in line with the

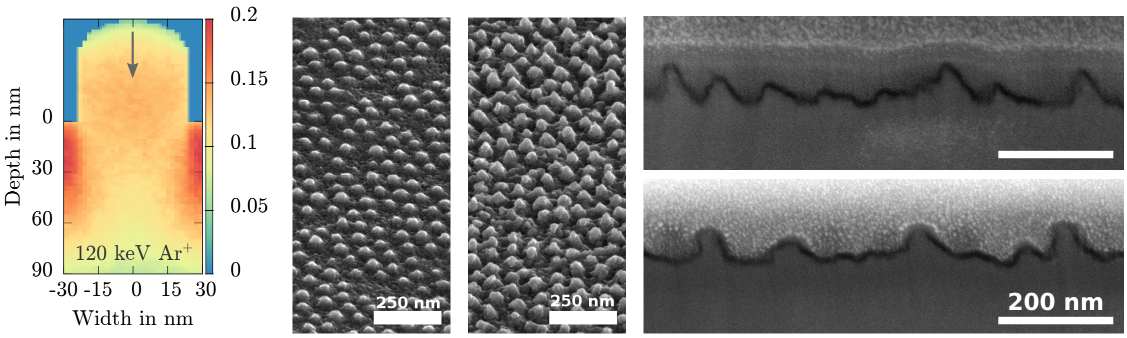

(a) **(b)** **(c)** **(d)**

Figure 7.5: (a) n_{dpa} in a LiNbO$_3$ nanostructure irradiated with 120 keV Ar$^+$ ions. The map shows the damage for a irradiation with a fluence of $1.5 \cdot 10^{14}$ ions/cm². (b) and (c): SEM images of z cut LiNbO$_3$ nanostructures after the (b) first and (c) second IBEE step. The substrate was z cut LiNbO$_3$. The used ion species was Ar$^+$. The ions had an energy of 120 keV in the second irradiation step, the fluence was $1.7 \cdot 10^{14}$ ions/cm². (d) Cross sections of a z cut LiNbO$_3$ nanostructures at different positions on a sample. The second IBEE step was performed using $1.7 \cdot 10^{14}$ ions/cm² 120 keV Ar$^+$ ions. The scale bars show the same length in both iamges. All images shown here were taken under an angle of 52 °.

simulations, which predicted even higher nanostructures. A possible explanation for the differences are the small ion fluences used for the second irradiation step, which have led to a defect concentration smaller than n_{dpa}^{crit}. Therefore, the substrate was not etched down to the undamaged areas. However, the damage on top of the nanostructures was in some cases already large enough that the pillar shape was not conserved, as shown in figure 7.5. This leads to the conclusion that the maximum ion fluence of $1.7 \cdot 10^{14}$ ions/cm² is already the limit for conserving the shape of the nanostructures produced in the first IBEE step without etching them down from the top. Thus, the LiNbO$_3$ nanostructures could not be enlarged further in height.

ZnO nanostructure masks The ZnO nanostructure masks were transferred to the LiNbO$_3$ substrates by imprinting technique, where the LiNbO$_3$ substrate and the ZnO growth substrate with the covered side were put together. After removing the ZnO growth substrate, ZnO nanostructures are transferred to the LiNbO$_3$ substrate randomly. The ZnO structures were inhomogeneous in size and shape with some nanowires inbetween. However, they had an average thickness larger than 500 nm. The irradiation parameters were the same as for 250 nm sized Au nanoparticles (see table 7.1).

Exemplary SEM images of ZnO nanostructures on a LiNbO$_3$ substrate before and after Ar$^+$ IBEE are shown in figure 7.6a and 7.6b, respectively. A sail-like structure lying next to a nanowire is depicted. The shape of the structures were perfectly reproduced in the LiNbO$_3$, as visible in figure 7.6b. The top surfaces of the LiNbO$_3$ nanostructures are smooth compared to the surrounding substrate. The ZnO nanowire in figure 7.6a has a diameter of $\sim$ 150 nm. Nevertheless, it was thick enough to slow down even 350 keV

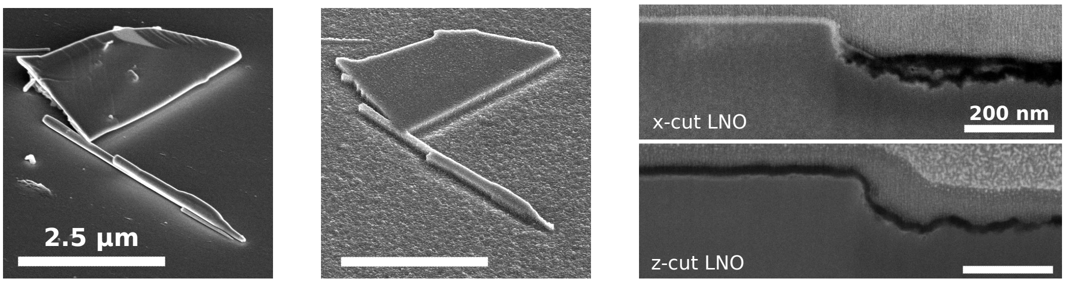

(a) (b) (c)

Figure 7.6: SEM images of a x cut $LiNbO_3$ substrate with a ZnO nanostructure as mask (a) before and (b) after the IBEE process using Ar^+ ions. The scale bar shows the same scale in both images. (c) Cross sections of x (top) and z cut (bottom) $LiNbO_3$ substrates after the IBEE process which were covered with a ZnO nanostructure. The used ion species was Ar^+. The scale bars are equal in both images. All images were taken under an angle of 52 ° with respect to the surface normal.

Ar^+ ions sufficiently. Cross sections of $LiNbO_3$ nanostructrures obtained by using ZnO nanowire masks were prepared to analyze the size and morphology of the nanostructures. Two cross sections are shown in figure 7.6c for x and z cut substrates. The top area of the nanostructures are very smooth compared to the substrate. The side facets of the structures are not very steep and the transition to the substrate is smooth. The average height is (195.0 ± 7.0) nm and (195.9 ± 13.3) nm for structures in x and z cut $LiNbO_3$, respectively.

The simulations predicted nanostructure heights of ~ 300 nm, which is a bigger difference compared to the experimental results in previous experiments using Au nanoparticle masks. It is possible that not all of the damaged material was etched and a defect-rich layer remains in the previously uncovered substrate ares. TEM investigations were performed to analyze the irradiated $LiNbO_3$ substrate over the depth. Figure 7.7a shows a TEM image of a lamella prepared from a x cut $LiNbO_3$ substrate after the IBEE process on an unmasked area. The structure of surface-near region differs from the substrate below over a depth from the surface of ~ 150 nm. The regions marked with α and γ show dark domains, which are not present in area β and δ and below. Areas α and γ may be regions where the respective 150 and 350 keV Ar^+ ions preferably come to rest. This would lead to stress in these regions. Another possible effect might be the creation of blisters, as previously reported for H^+ and He^+ ion irradiation of $LiNbO_3$ [153, 154]. A definitive answer to the question of the origin of the dark domains can not be given from the TEM image. Figures 7.7b and 7.7d show close-up images of regions β and ε, while figures 7.7c and 7.7e show the fast Fourier transforms (FFT) of the respective images of regions β and ε. The FFT of region ε clearly shows reflexes of the lattice planes, while the FFT of region β only shows a few defined reflexes of lattice planes and mostly blurred reflexes. This shows that region β is damaged, but not amorphized. Therefore, not all damaged regions were etched.

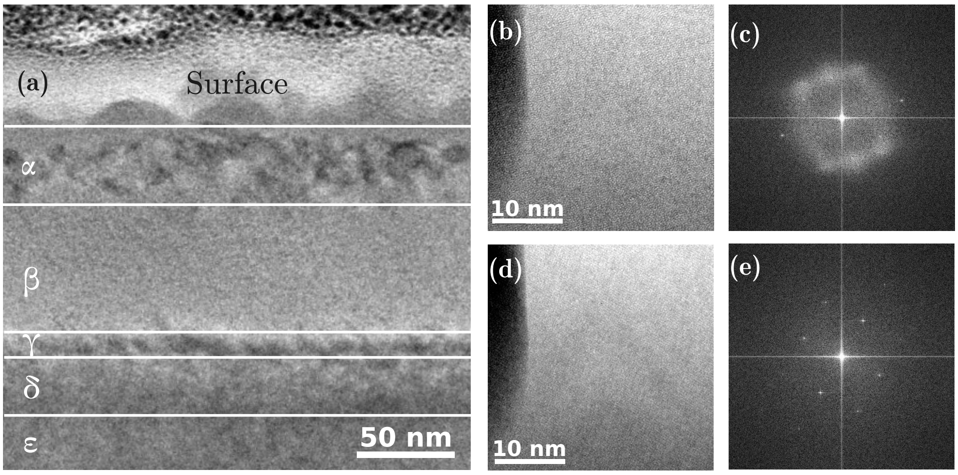

Figure 7.7: TEM images of a lamella from a x cut $LiNbO_3$ sample after the IBEE process using Ar^+ ions. The mask was a ZnO nanostructure. (a) Overview image. The layers of different defect concentrations are numbered from the surface from α to ε. (b) Close-up image of region β, (c) FFT of β, (d) close-up image of region ε, (e) FFT of ε.

7.3 Annealing

A possible way to reduce surface roughness and increase the height of structures produced by IBEE can be annealing between irradiation and etching step. The depdence of defect concentration, structure height and roughness on the annealing time at 300 °C under air was investigated using x cut $LiNbO_3$ samples with ZnO nanostructure imprints. The irradiation parameters are the same as used in previous experiments with ZnO nanostructure masks.

Structural changes The defect concentration as a function of depth was investigated using RBS. For this purpose, pristine $LiNbO_3$ samples were irradiated without any mask structures. Afterwards, the samples were annealed at 300 °C in air. The samples were analyzed by RBS before irradiation and after IBEE with subsequent annealing. The defect concentration was calculated using *DICADA* [132]. Figure 7.8a shows the defect concentration n_{da} as a function of the depth and annealing time. The highest defect concentration can be observed up to a depth of 200 nm. This depth is independent of the annealing time. The annealing of high defect concentrations is low, because point defects above a certain concentration agglomerate and form stable dislocation loops [155]. However, a slight decrease of the defect concentration is noticable. The defect concentration is lower in depths below 200 nm from the surface, where the annealing is more significant. The amount of defects decreases most in the region between 200 and 400 nm depth, where the transition between damaged and crystalline material is located. This region is marked with β in the TEM image of a sample after IBEE and annealing in figure 7.8b. Region α is a defect rich region with a width of $200 - 300$ nm

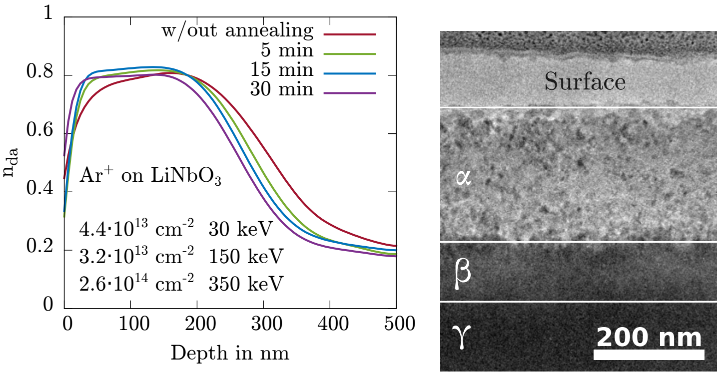

(a) **(b)**

Figure 7.8: (a) Defect concentration in x cut LiNbO$_3$ after ion beam irradiation with the irradiation parameters given in the figure after different times of annealing at 300 °C. The data was obtained by RBS measurements. (b) TEM image of a lamella from a x cut LiNbO$_3$ sample after the IBEE process using Ar$^+$ ions with the parameters listed in figure 7.8a. The mask was a ZnO nanostructure. The sample was annealed for 30 min at 300 °C before etching.

and γ the undamaged crystalline LiNbO$_3$. The defects migrate from the transition region (β) towards the surface with proceeding annealing time [150]. Thus, the heights of the nanostructures would be reduced by $\sim$ 50 nm compared to the samples without annealing. Figures 7.9a and 7.9b show SEM images of nanostructures in x cut LiNbO$_3$ after the IBEE process without annealing and after 30 min annealing at 300 °C, respectively. The substrate around the nanostructures was etched away in case of the unannealed sample (7.9a). However, it seems that the etching rate on the uncovered substrate of the annealed sample (7.9b) was sigificantly smaller than in the substrate directly next to the nanostructure: the nanostructure seems to be sunk into the substrate where a trench is visible around the nanostructure. The RBS results in figure 7.8a show that the defect concentration at the surface is low. It is possible that the defects at the surface have annealed and formed an inert layer, which was not etched by HF. This is underlined by

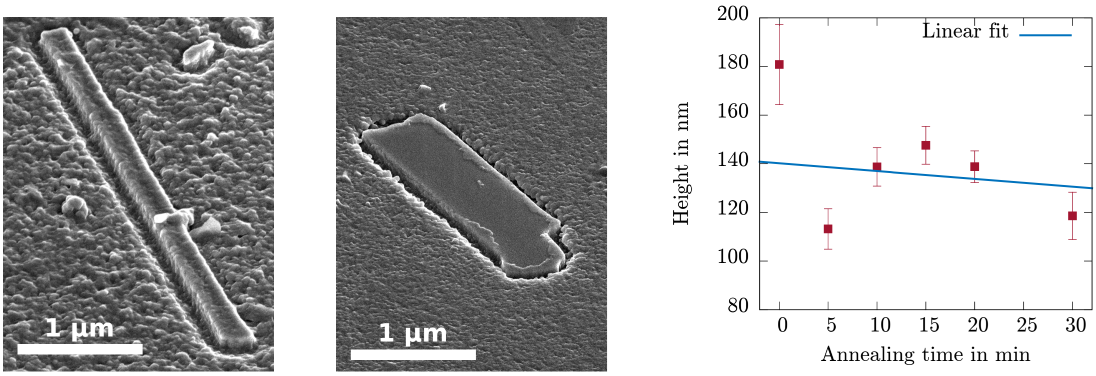

(a) **(b)** **(c)**

Figure 7.9: (a) and (b) show SEM images of LiNbO$_3$ nanostructures produced by IBEE using ZnO nanostructure masks. (a) sample without annealing, (b) sample after 30 min annealing at 300 °C. The SEM images were taken under an angle of 52 ° to the surface normal. (c) Height of the nanostructures in x cut LiNbO$_3$ after the IBEE process as a function of annealing time. The blue line shows a linear fit $f(x) = a \cdot x + b$, with $a = -0.3\,{}^{\mathrm{nm}}/_{\mathrm{min}}$.

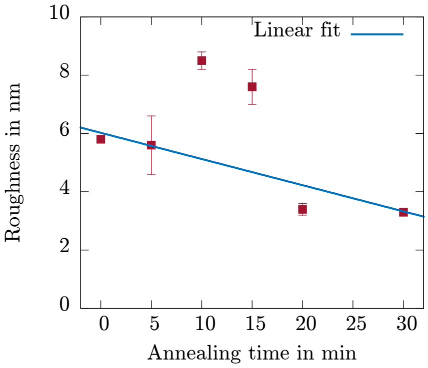

Figure 7.10: Roughness of x cut LiNbO$_3$ samples after the IBEE process as a function of the annealing time at 300 °C. The blue line is a linear fit with the function $f(x) = a \cdot x + b$, with a slope $a = -0.1\,{}^{\mathrm{nm}}/_{\mathrm{min}}$.

the fact that the surface of the unannealed sample shows a significantly higher roughness than the annealed sample.

The heights of the nanostructures were measured by preparing cross sections. The results of the height measurements are shown in figure 7.9c as a function of the annealing time. A large variation of the data points without a clear trend is apparent. However, the nanostructure height seems to decrease with increasing annealing time, as the linear fit in figure 7.9c indicates. The fit considers the error bars of the data and has a negative slope of $a = -0.3\,{}^{\mathrm{nm}}/_{\mathrm{min}}$, which indicates a small height decrease with increasing annealing time. The fit does not consider the fact that the ZnO nanostructure sizes may vary before the irradiation, which defines the nanostructure heights. Therefore it has to be concluded that the height of the LiNbO$_3$ nanostructures produced by IBEE with the presented parameters is more or less independent on the annealing time.

Surface roughness Figures 7.9a and 7.9b suggested that the roughness of the surfaces of the etched samples changes with annealing time. Surface roughness might be undesirable for optical applications. The roughness was measured by AFM as a function of the annealing time on samples after the IBEE process. Every LiNbO$_3$ sample analyzed by RBS in terms of defect concentration (see previous paragraph) was investigated on three randomly chosen positions on an area of $1 \times 1\,\mu\mathrm{m}^2$. The results are shown in figure 7.10. The trend (shown as a linear fit) of the data points shows that the roughness decreases with the annealing time with a slope of $a = -0.1\,{}^{\mathrm{nm}}/_{\mathrm{min}}$, which is almost constant (in consideration of uncertainties). Therefore, no clear relation between annealing time and surface roughness could be found using AFM. However, the data points at 10 and 15 min are out of line. Still, the 30 min annealing time shows the lowest roughness of all samples.

7.4 Summary

A "top-up" approach was successfully applied to $LiNbO_3$ by using Ar^+ and Kr^+ ions of energies between 30 and 350 keV with "bottom-up" grown Au nanoparticles and imprinted ZnO nanowires as irradiation masks in the IBEE process. Small nanoparticles with a diameter of 50 nm led to hillock-shaped nanostructures with a height of $\sim$ 60 nm in $LiNbO_3$ substrates, while Au nanoparticles with diameters of 100 and 250 nm produced pillar-shaped nanostructures with heights of $\sim$ 80 and $\sim$ 100 nm, respectively. The height of $LiNbO_3$ nanostructures depended on the interparticle distance of the Au nanoparticles. Shadowing effects on Au nanoparticles with interparticle distances of 10 nm reduced the ion range in the uncovered $LiNbO_3$. Zinc oxide nanostructures were found to be also a suitable masks, which led to structure heights of $\sim$ 200 nm. The experiments revealed that the produced $LiNbO_3$ nanostructure height was independent of the substrate type (x and z cut $LiNbO_3$). The height of the structures could be increased by 30 nm with a second IBEE step after annealing the samples. The $LiNbO_3$ nanostructures after the first IBEE step itself served as irradiation masks.

The height of the $LiNbO_3$ nanostructures was investigated as a function of the annealing time of an annealing step between irradiation and etching step. It was found that the structure height was independent of the annealing time between 5 and 30 min at annealing temperatures of 300 °C. However, TEM investigations at the annealed samples revealed that not all damaged material was etched by HF. Additionally, the $LiNbO_3$ substrate was preferably etched around the nanostructures after annealing. The surface roughness was investigated by AFM as a function of annealing time, which was found to be constant.

8 | Conclusion and outlook

Ion-solid interaction, and especially sputtering, was investigated extensively in the past for bulk structures and thin films and is nowadays used in a wide range of industrial applications, such as doping of integrated circuits or sputter deposition of thin films. However, the interaction of ions and nanostructures is only investigated recently due to the newly found advantages of the ion beam modification of nanostructured materials. New simulation codes like *iradina* [45] and *TRI3DYN* [46] allow a detailed study of ion-solid interactions on the nanoscale, which was already presented in the literature. Experimental investigations, however, were rare. Gold nanoparticles are excellent model system to investigate ion-nanostructure interactions experimentally. This thesis reports in detail on the effects, which occur when nanoparticles on substrates are irradiated with ions, focusing on sputtering effects. This topic was investigated applying Monte Carlo (MC) and Molecular Dynamic (MD) simulations as well as a wide range of experiments. The ion-nanostructure interaction was modelled using the binary collision approximation (BCA) based MC code *iradina* and the MD code *parcas* [48] in order to determine significant parameters for the experimental ion irradiation of Au nanostructures to investigate the energy and structure size dependence of the sputter yield. As nanoparticles are typically arranged in an array on substrates, also the interaction between ion irradiated Au nanoparticles was investigated. Redeposition of sputtered atoms from nanoparticles on their neighbors was studied by using a recently developed dynamic MC code, which was developed within this thesis. The results from these simulations were compared to *in situ* experiments on a Au nanoparticle array. Besides their role as functional elements in devices, nanostructures can further be used as irradiation masks in order to structure lithium niobate ($LiNbO_3$) by ion beams. Therefore, these findings from the experiments and simulations in combination with previous works on the method of ion beam enhanced etching (IBEE) [53] allowed to structure ($LiNbO_3$) with Au and semiconductor nanostructures as masks.

Chapter 4 discusses the simulation of sputtering of ion irradiated Au nanostructures using *iradina* and *parcas*. Spherical and cylindrical Au nanopstructures with fixed diameters of 50 nm were (virtually) irradiated with Ar^+ and Ga^+ ions of various energies between 1 and 350 keV. Subsequently, the nanostructure's sizes were varied, while the ion energies were kept constant at 100 and 25 keV for Ar^+ and Ga^+ ions, respectively. The sputter yield is strongly influenced by the ion's energy and nanostructure size and revealed a maximum at the energy, at which the ion range matches the nanostructure's diameter.

The sputter yield depends further on the projectile's mass, such that the sputter yield increased with the ion mass due to denser collision cascades in the irradiated material. Additionally, spherical nanoparticles revealed a higher sputter yield upon ion irradiation compared to cylindrical nanowires for both simulated ion species and all ion energies and structure diameters. Nonetheless, the sputter yields of both nanostructures were significantly enhanced compared to bulk morphology up to a factor of ~ 6. These dependecies of the sputter yield on ion energy, structure diameter and geometry are explained by the intersection area of the damage cascade inflicted by the ion with the surface of the nanostructure. This intersection area increases with surface curvature and reaches its maximum when the damage cascade overlaps with most of the nanostructure's volume. These results explain the appearance of a maximum sputter yield when the ion range matches the particle diameter. These results are in agreement with recently published literature [75, 76, 140]. Additionally, the sputter yield depends on the surface-cascade intersection, thus the impact position of the ion relatively to the nanostructure strongly influences the sputter yield. Consequently, the sputter yield was larger for grazing ion impact than for central impacts. This was analytically described by a model based on Gaussian damage distributions. The angular distribution of the sputtered atoms of a spherical nanoparticle turned out to be symmetric in azimuthal direction while being size dependent in polar direction. The maximum in polar direction shifts between 0 and $\pi/2$ towards smaller angles with increasing nanoparticle size.

MD simulations were performed for 25 keV Ga^+ ions irradiating spherical Au nanoparticles of various sizes, because this corresponds to the experimental conditions of an experiment within this thesis. The obtained size dependence of the sputter yield was qualitatively comparable to the MC result. It was one order of magnitude larger compared to the MC result in it's quantitative value. The reasons for this difference are the simplified assumptions of the MC simulation of binary collisions in contrast to the more detailed MD calculations. However, the angular distributions of the sputtered atoms obtained with the MD simulations matched those from the MC simulations. Additionally, the MD simulations revealed that the temperature inside a nanoparticle can rise considerably above the melting point after a single ion impact and depends inverse proportional on the nanoparticle diameter or the number of atoms. The extreme heating of particles with diameters smaller than 20 nm may even lead to a complete evaporation of the material. If small nanoparticles do not evaporate, they mostly regain their spherical shape. In contrast, nanoparticles with diameters larger than 20 nm retained carters at the ion impact position.

The results from chapter 4 were experimentally verified using Ar^+ and Ga^+ ions, which were presented in chapter 5. The ion irradiation on Au nanoparticle arrays as well as single Au nanoparticles were investigated using high resolution scanning electron microscopy (SEM). The statistical evaluation of the experiments using Ga^+ ions on nanoparticle arrays reproduced the trend of the energy dependence of the sputter yield from the MC simulations qualitatively for ion energies smaller than 30 keV. However, the amount of sputtered atoms was almost up to twice the number from the *iradina* nanoparticle simulations. Additionally, the energy dependence of the sputter yield was investigated over a larger energy range from 10 to 350 keV using Ar^+ ions. The MC simulation underestimates the experiment by $5\,{}^{\text{atoms}}/_{\text{ion}}$, which is not as significant as in the Ga^+ experiments. The trend of the MC simulated sputter yield as a function of energy agreed also qualitatively for ion energies smaller than 110 keV and larger than 250 keV. The energy range between 100 and 250 keV was governed by a large spread of the sputter yield due to thermally driven effects. These thermally driven effects originate from the evaporation of the nanoparticles, as explained by MD simulations.

The size dependence of the sputter yield was also experimentally investigated on nanoparticle arrays using Ga^+ ions. Here, the trend of the simulated sputter yield was also in agreement with the MC simulation for nanoparticle diameters larger than 30 nm. However, the experimental results lay in between the *iradina* simulation sputter yields and the values predicted by Järvi *et al.* [51].

The *in situ* experiments on single Au nanoparticles using Ga^+ ions revealed a similar dependence on the ion energy as the experiments on nanoparticle arrays in the investigated energy range. The size dependence of the sputter yield of single nanoparticles was measured using the evolution of the nanoparticle size with progressing irradiation steps. The results of MC and MD simulation and experiment coincide qualitativley (in most cases). However, the experimentally measured sputter yields also lay in between the smaller value of the MC simulation and the larger value of the MD simulation.

The maximum of the sputter yield could not be investigated in these *in situ* experiments as a significant intermixing of Au and the Si substrate occured for high fluence irradiations. This was proven using Rutherford backscattering spectrometry (RBS), scanning transmission electron microscopy (STEM) and atomic force microscopy (AFM). The STEM experiments revealed an increasing amount of Au sinking from the nanoparticles into the substrate with increasing ion fluence. The RBS measurements on reference samples consisting of 40 nm thin Au layers on Si confirmed this observation. Additionally, the RBS showed that the formation of Au silicide slows significantly down Au sputtering with increasing fluence because of preferential sputtering of Si. The AFM investigations showed that craters form at high fluence Ar^+ irradiation at Au nanoparticle positions. Backscatter SEM images revealed that Au is still present at these positions inside the subsrtate. The craters became deeper with increasing ion fluence, until the digging saturates at crater depths of ~ 4 nm for a fluence of $1 \cdot 10^{16}\,{}^{\text{ions}}/_{\text{cm}^2}$. Having reached this maximum, the crater depth decreased and the sample surface smoothed almost completely at high ion fluences of $6 \cdot 10^{16}\,{}^{\text{ions}}/_{\text{cm}^2}$. The crater width was almost constant for all investigated fluences.

The interaction between neighboring and ion irradiated Au nanoparticles arranged in an array was investigated in chapter 6 using a newly developed dynamic MC code based on *iradina* simulation results presented in chapter 4 and Järvi's sputtering model [51]. The code simulates the interaction between ion irradiated Au nanoparticles with a Gaussian size ordered in an array by taking both sputtering and redeposition of sputtered atoms into account. The results of the simulation showed that the Gaussian distribution of the nanoparticle diameters was conserved during irradiation. The mean diameter shifted towards smaller diameters as the sputtering is pronounced compared to redeposition. The mean diameter after irradiation for simulations with redeposition was 2 nm larger than for the simulation without redeposition. Both simulated size distributions with and without redeposition matched the experimental size distribution of Ga^+ irradiated Au nanoparticle arrays within the experimental error when scaled Järvis model was applied. In addition, the simulation revealed that the redeposition rate depends on the nanoparticle size: for nanoparticle sizes larger than 30 nm, approximately $10 - 20\,\%$ of the sputtered material was redeposited at the other nanoparticles, whereas the redeposition is minimal for nanoparticle sizes, where the sputter yield reaches it's maximum. The amount of redeposited material increases steeply for nanoparticle diameters smaller than 10 nm, such that small nanoparticles with a diameter of $\sim$ 1 nm can even grow due to redeposition. Furthermore, the amount of redeposited material also increases with increasing size of neighboring nanoparticles, since only large particles with a high ion impact probability can deliver a sufficient number of atoms for redeposition. In general, *in situ* experiment and MC simulation are in good agreement, until intermixing of Au nanoparticle and substrate starts in the experiment.

The fundamental insights gained within the previous chapters were used in order to structure lithium niobate ($LiNbO_3$) on the nanoscale by a top-up approach. Various types of Au nanoparticles and zinc oxide (ZnO) nanostructures were used as irradiation mask to structure $LiNbO_3$ using the established IBEE process [53]. The appropriate irradiation parameters for Ar^+ and Kr^+ ions and for different mask materials and geometries were calculated by *iradina* simulations. The samples with the respective masks were irradiated and wet chemically etched using hydrofluoric acid (HF) according to the process given in references [53, 123]. The process worked for all used nanostructures; however, nanostructures with diameters larger than 100 nm led to more defined structures in the $LiNbO_3$ substrate. Masks with 50 nm diameter Au nanoparticles led to cone-shaped nanostructures, while Au nanoparticles with diameters larger than 100 nm produced pillar-shaped nanostructures in $LiNbO_3$. It also becomes apparent that due to small interparticle distances of hexagonally arranged Au nanoparticles, the height of the produced $LiNbO_3$ nanostructures was reduced. The height of $LiNbO_3$ nanostructures created with 50 nm sized Au nanoparticles could be significantly increased up to $\sim$ 80 nm by a second IBEE step without additional mask structures with an annealing step between both IBEE steps.

The work presented in this thesis generated significant insights into the physics of ion-nanostructure interactions and will stimulate further researchg in this field. Simulations are a valid way to model complex physical interactions and can be used to draw a path for setting up valid experimental parameters. Experiments, on the other hand, are the most reliable source of knowledge and, as this thesis showed, can be used to verify simulation models. Furthermore, the interplay of simulation and experiment helps to adjust the algorithms and inputs towards more realistic predictions. The *in situ* experiments presented in this thesis revealed their limitations in the intermixing of Au nanoparticle and the Si substrate. The use of other substrate materials than Si, such as sapphire, might solve this problem, because Klimmer *et al.* showed that nanoparticles do not get burried in sapphire during ion irradiation [106]. However, the experiment can be repeated for other nanostructure geometries, materials and ion species, as already performed in reference [32, 38], to gain a quantitative reliable source of sputter yields of ion irradiated nanostructures for other applications like ion beam doping. Unfortunately, sputtering is usually an undesired side effect when trying to tailor the properties of materials by ion beams. Thus, the exact knowledge of sputter yields of nanostructures can help to adjust the irradiation parameters of experiments for other purposes. The exact knowledge of sputtering can on one hand be used effectively to change the morphology of nanostructures, or, on the other hand, be used to circumvent undesired effects such as increased dopant concentration in ion beam doped nanowires due to sputtering [32].

The MC code for simulating interactions between ion irradiated Au nanoparticles ordered in an array gave first insights into the redeposition of sputtered atoms. The model was simple and can be expanded by implementing other nanostructure geometries like nanowires and using more complex sputtering models. The implementation of the impact parameter dependent sputtering, as shown in section 4.2, and the respective angular distributions as well as cluster sputtering would result in a more defined picture of the particle-particle interactions.

The top-up process for nanostructuring $LiNbO_3$ can be expanded to other mask geometries. Therefore, the self-organized growth of nanostructures on top of $LiNbO_3$ substrate needs to be investigated more in detail. If defined $LiNbO_3$ nanostructures are produced, they can be investigated on their optical properties for possible future applications.

Bibliography

[1] G. E. Moore. Cramming more components onto integrated circuits. *Electronics*, 38(8):114 ff, 1965.

[2] K. Autumn, Y. A. Liang, S. T. Hsieh, W. Zesch, W. P. Chan, T. W. Kenny, R. Fearing, and R. J. Full. Adhesive force of a single gecko foot-hair. *Nature*, 405(6787):681–685, 2000.

[3] M. Sarikaya, C. Tamerler, A. K. Y. Jen, K. Schulten, and F. Baneyx. Molecular biomimetics: nanotechnology through biology. *Nature Materials*, 2(9):577–585, 2003.

[4] G. A Ozin. Nanochemistry: synthesis in diminishing dimensions. *Advanced Materials*, 4(10):612–649, 1992.

[5] J.M. Gutierrez, C. Gonzalez, A. Maestro, I. Sole, C.M. Pey, and J. Nolla. Nano-emulsions: New applications and optimization of their preparation. *Current Opinion in Colloid & Interface Science*, 13(4):245 – 251, 2008.

[6] E. H. Chowdhury and T. Akaike. Bio-Functional Inorganic Materials: An Attractive Branch of Gene-Based Nano-Medicine Delivery for 21st Century. *Current Gene Therapy*, 5(6):669–676, 2005.

[7] M. S. Moghimi, C. A. Hunter, and C. J. Murray. Nanomedicine: current status and future prospects. *The FASEB Journal*, 19(3):311–330, 2005.

[8] R. S. Friedman, M. C. McAlpine, D. S. Ricketts, D. Ham, and C. M. Lieber. Nanotechnology High-speed integrated nanowire circuits. *Nature*, 434(7037):1085–1085, 2005.

[9] A. K. Geim and K. S. Novoselov. The rise of graphene. *Nature Materials*, 6(3):183–191, 2007.

[10] T. P. H. Sidiropoulos, R. Röder, S. Geburt, O. Hess, S. A. Maier, C. Ronning, and R. F. Oulton. Ultrafast plasmonic nanowire lasers near the surface plasmon frequency. *Nature Physics*, 10(11):870–876, 2014.

[11] L. Levy, Y. A. Sahoo, K. Kim, E. J. Bergey, and P.N. Prasad. Nanochemistry: Synthesis and Characterization of Multifunctional Nanoclinics for Biological Applications. *Chemistry of Materials*, 14(9):3715–3721, 2002.

[12] K.P. Rajurkar, G. Levy, A. Malshe, M.M. Sundaram, J. McGeough, X. Hu, R. Resnick, and A. DeSilva. Micro and Nano Machining by Electro-Physical and Chemical Processes. *CIRP Annals - Manufacturing Technology*, 55(2):643 – 666, 2006.

[13] M. Esmaili, S. M. Ghaffari, Z. Moosavi-Movahedi, M. Sadat Atri, A. Sharifizadeh, M. Farhadi, R. Yousefi, J.-M. Chobert, T. Haertlé, and A. A. Moosavi-Movahedi. Beta casein-micelle as a nano vehicle for solubility enhancement of curcumin; food industry application. *LWT - Food Science and Technology*, 44(10):2166 – 2172, 2011.

[14] S. Marchesan and M. Prato. Nanomaterials for (Nano)medicine. *ACS Medicinal Chemistry Letters*, 4(2):147–149, 2013.

[15] Y. Lu and P. K. Liaw. The mechanical properties of nanostructured materials. *The Journal of The Minerals, Metals & Materials Society*, 53(3):31–35, 2001.

[16] C. Q. Chen and J. Zhu. Bending strength and flexibility of ZnO nanowires. *Applied Physics Letters*, 90(4), 2007.

[17] F. Flory, L. Escoubas, and G. Berginc. Optical properties of nanostructured materials: a review. *Journal of Nanophotonics*, 5(1):052502–052502–20, 2011.

[18] C. Gutsche, R. Niepelt, M. Gnauck, A. Lysov, W. Prost, C. Ronning, and F.-J. Tegude. Direct Determination of Minority Carrier Diffusion Lengths at Axial GaAs Nanowire p-n Junctions. *Nano Letters*, 12(3):1453–1458, 2012.

[19] D. Cammi and C. Ronning. Persistent Photoconductivity in ZnO Nanowires in Different Atmospheres. *Advances in Condensed Matter Physics*, 2014, 2014.

[20] L.-E. Wernersson, E. Lind, L. Samuelson, T. Löwgren, and J. Ohlsson. Nanowire Field-Effect Transistor. *Japanese Journal of Applied Physics*, 46(4S):2629, 2007.

[21] R. Röder, M. Wille, S. Geburt, J. Rensberg, M. Zhang, J. G. Lu, F. Capasso, R. Buschlinger, U. Peschel, and C. Ronning. Continuous wave nanowire lasing. *Nano Letters*, 13(8):3602–3606, 2013.

[22] P. K. Jain, X. Huang, I. H. El-Sayed, and M. A. El-Sayed. Review of Some Interesting Surface Plasmon Resonance-enhanced Properties of Noble Metal Nanoparticles and Their Applications to Biosystems. *Plasmonics*, 2(3):107–118, 2007.

[23] X. Gong, Z. Yang, G. Walters, R. Comin, Z. Ning, . Beauregard, V. Adinolfi, O. Voznyy, and E. H. Sargent. Highly efficient quantum dot near-infrared light-emitting diodes. *Nature Photonics*, 10(4):253–257, 2016.

[24] C. Haginoya, M. Ishibashi, and K. Koike. Nanostructure array fabrication with a size-controllable natural lithography. *Applied Physics Letters*, 71(20):2934–2936, 1997.

[25] B. J.M. Hausmann, M. Khan, Y. Zhang, T. M. Babinec, K. Martinick, M. McCutcheon, P. R. Hemmer, and M. Loncar. Fabrication of diamond nanowires for quantum information processing applications. *Diamond and Related Materials*, 19(5–6):621 – 629, 2010.

[26] D. Dobkin and M. K. Zuraw. *Principles of Chemical Vapor Deposition.* Springer Science & Business Media, 2013.

[27] D. M. Mattox. *Handbook of Physical Vapor Deposition (PVD) Processing.* William Andrew, 2010.

[28] J. Sadowsk, P. Dluzewski, S. Kret, E. Janik, E. Lusakowska, J. Kanski, A. Presz, F. Terki, S. Charar, and D. Tang. GaAs:Mn Nanowires Grown by Molecular Beam Epitaxy of (Ga,Mn)As at MnAs Segregation Conditions. *Nano Letters*, 7(9):2724–2728, 2007.

[29] P. Xie, Y. Hu, J. Fang, Y.and Huang, and C. M. Lieber. Diameter-dependent dopant location in silicon and germanium nanowires. *Proceedings of the National Academy of Sciences*, 106(36):15254–15258, 2009.

[30] M. Nastasi, J. Mayer, and J. K. Hirvonen. *Ion-solid interactions: fundamentals and applications.* Cambridge University Press, 1996.

[31] E. Wendler, A. Heft, and W. Wesch. Ion-beam induced damage and annealing behaviour in SiC. *Nuclear Instruments and Methods in Physics Research Section B: Beam Interactions with Materials and Atoms*, 141(1-4):105 – 117, 1998.

[32] A. Johannes, H. Holland-Moritz, and C. Ronning. Ion beam irradiation of nanostructures: sputtering, dopant incorporation, and dynamic annealing. *Semiconductor Science and Technology*, 30(3):033001, 2015.

[33] T.T. Järvi and K. Nordlund. Sputtering of freestanding metal nanocrystals. *Nuclear Instruments and Methods in Physics Research Section B: Beam Interactions with Materials and Atoms*, 272:66 – 69, 2012.

[34] G. Greaves, J. A. Hinks, P. Busby, N. J. Mellors, A. Ilinov, A. Kuronen, K. Nordlund, and S. E. Donnelly. Enhanced Sputtering Yields from Single-Ion Impacts on Gold Nanorods. *Physical Review Letters*, 111(6):065504, 2013.

[35] P. Williams. Secondary Ion Mass Spectrometry. *Annual Review of Materials Science*, 15(1):517–548, 1985.

[36] P. M. Nellen, V. Callegari, and R. Brönnimann. FIB-milling of photonic structures and sputtering simulation. *Microelectronic Engineering*, 83(4-9):1805 – 1808, 2006.

[37] L.A. Giannuzzi and F.A. Stevie. A review of focused ion beam milling techniques for TEM specimen preparation. *Micron*, 30(3):197 – 204, 1999.

[38] A. Johannes, S. Noack, W. Paschoal Jr, S. Kumar, D. Jacobsson, H. Pettersson, L. Samuelson, K. A. Dick, G. Martinez-Criado, M. Burghammer, and C. Ronning. Enhanced sputtering and incorporation of Mn in implanted GaAs and ZnO nanowires. *Journal of Physics D: Applied Physics*, 47(39):394003, 2014.

[39] S. Geburt, A. Thielmann, R. Röder, C. Borschel, A. McDonnell, M. Kozlik, J. Kühnel, K. A. Sunter, F. Capasso, and C. Ronning. Low threshold room-temperature lasing of CdS nanowires. *Nanotechnology*, 23(36):365204, 2012.

[40] S. Zimmermann and H. M. Urbassek. Sputtering of nanoparticles: Molecular dynamics study of Au impact on 20 nm sized Au nanoparticles. *International Journal of Mass Spectrometry*, 272(1):91–97, 2008.

[41] T. Teranishi, M. Haga, Y. Shiozawa, and M. Miyake. Self-Organization of Au Nanoparticles Protected by 2,6-Bis(1'-(8-thiooctyl)benzimidazol-2-yl)pyridine. *Journal of the American Chemical Society*, 122(17):4237–4238, 2000.

[42] Y. Sun and Y. Xia. Shape-Controlled Synthesis of Gold and Silver Nanoparticles. *Science*, 298(5601):2176–2179, 2002.

[43] C. Stanglmair, S. P. Scheeler, and C. Pacholski. Seeding Growth Approach to Gold Nanoparticles with Diameters Ranging from 10 to 80 Nanometers in Organic Solvent. *European Journal of Inorganic Chemistry*, 2014(23):3633–3637, 2014.

[44] J. F. Ziegler, M. D. Ziegler, and J. P. Biersack. SRIM – The stopping and range of ions in matter (2010). *Nuclear Instruments and Methods in Physics Research B*, 268(11–12):1818–1823, 2010.

[45] C. Borschel and C. Ronning. Ion beam irradiation of nanostructures – A 3D Monte Carlo simulation code. *Nuclear Instruments and Methods in Physics Research Section B*, 269(19):2133–2138, 2011.

[46] W. Möller. TRI3DYN – Collisional computer simulation of the dynamic evolution of 3-dimensional nanostructures under ion irradiation. *Nuclear Instruments and Methods in Physics Research Section B: Beam Interactions with Materials and Atoms*, 322:23 – 33, 2014.

[47] C. Borschel. *Ion-Solid Interaction in Semiconductor Nanowires.* PhD thesis, Friedrich-Schiller-Universität Jena, 2012.

[48] K. Nordlund, M. Ghaly, R. S. Averback, M. Caturla, T. Diaz de la Rubia, and J. Tarus. Defect production in collision cascades in elemental semiconductors and fcc metals. *Physical Review B*, 57:7556 – 7570, 1998.

[49] M. Ghaly, K. Nordlund, and R. S. Averback. Molecular dynamics investigations of surface damage produced by kiloelectronvolt self-bombardment of solids. *Philosophical Magazine A*, 79(4):795 – 820, 1999.

[50] S. Ullrich, S. P. Scheeler, C. Pacholski, J. P. Spatz, and S. Kudera. Formation of Large 2D Arrays of Shape-Controlled Colloidal Nanoparticles at Variable Interparticle Distances. *Particle & Particle Systems Characterization*, 30(1):102–108, 2013.

[51] T. T. Järvi, J. A. Pakarinen, A. Kuronen, and K. Nordlund. Enhanced sputtering from nanoparticles and thin films: Size effects. *Europhysics Letters*, 82(2):26002, 2008.

[52] R. S. Weis and T. K. Gaylord. Lithium niobate: Summary of physical properties and crystal structure. *Applied Physics A*, 37(4):191–203, 1985.

[53] F. Schrempel, Th. Gischkat, H. Hartung, E. B. Kley, and W. Wesch. Ion beam enhanced etching of LiNbO3. *Nuclear Instruments and Methods in Physics Research Section B: Beam Interactions with Materials and Atoms*, 250(1–2):164–168, 2006.

[54] Sven Bauer. Nanostrukturierung von Lithiumniobat mittels selbstorganisierter Nanostrukturmasken und Ionenstrahlen. Master's thesis, Friedrich-Schiller-Universitä Jena, 2015.

[55] H. Bethe. Zur Theorie des Durchgangs schneller Korpuskularstrahlen durch Materie. *Annalen der Physik*, 397(3):325–400, 1930.

[56] J. F. Ziegler, J. P. Biersack, and U. Littmark. *The Stopping and Range of Ions in Solids.* Pergamon, 1985.

[57] G. Götz and K. Gärtner. *High energy ion beam analysis of solids.* Akademie-Verlag, 1988.

[58] P. Sigmund. *Stopping of Heavy Ions: A Theoretical Approach.* Springer Science & Business Media, 2004.

[59] Jens Lindhard, Morten Scharff, and Hans Schiøtt. Range concepts and heavy ion ranges. *Matematisk-Fysiske Meddelelser Konglige Danske Videnskabernes Selskab*, 33(14), 1963.

[60] W. Eckstein. *Computer Simulation of Ion-Solid Interactions*. Springer Science & Business Media, 2013.

[61] J. F. Gibbons, J. L. Moll, and N. I. Meyer. The doping of semiconductors by ion bombardment. *Nuclear Instruments and Methods*, 38:165–168, 1965.

[62] C. Ronning, C. Borschel, S. Geburt, and R. Niepelt. Ion beam doping of semiconductor nanowires. *Materials Science and Engineering*, 70:30–43, 2010.

[63] G. R. Piercy, F. Brown, J. A. Davies, and M. McCargo. Experimental evidence for the increase of heavy ion ranges by channeling in crystalline structure. *Physical Review Letters*, 10:399–400, 1963.

[64] P. Sigmund. Theory of Sputtering. I. Sputtering Yield of Amorphous and Polycrystalline Targets. *Physical Review*, 184(2):383–416, 1969.

[65] Y. Yamamura. Theory of sputtering and comparison to experimental data. *Nuclear Instruments and Methods in Physics Research*, 194(1):515 – 522, 1982.

[66] M. Szymonski. Sputtering mechanisms of compound solids. *Nuclear Instruments and Methods in Physics Research*, 194(1):523 – 531, 1982.

[67] N. Matsunami, Y. Yamamura, Y. Itikawa, N. Itoh, Y. Kazumata, S. Miyagawa, K. Morita, R. Shimizu, and H. Tawara. Energy dependence of the ion-induced sputtering yields of monatomic solids. *Atomic Data and Nuclear Data Tables*, 31(1):1 – 80, 1984.

[68] Y. Kudriavtsev, A. Villegas, A. Godines, and R. Asomoza. Calculation of the surface binding energy for ion sputtered particles. *Applied Surface Science*, 239(3–4):273–278, 2005.

[69] P. Sigmund and C. Claussen. Sputtering from elastic-collision spikes in heavy-ion-bombarded metals. *Journal of Applied Physics*, 52(2):990–993, 1981.

[70] T. Som. *Nanofabrication by Ion-Beam Sputtering: Fundamentals and Applications*. Pan Stanford Publishing Pte Ltd, 2012.

[71] C. Kittel. *Introduction to Solid State Physics*. John Wiley and Sons Ltd, 8 rev ed. edition, 2004.

[72] J. B. Malherbe, S. Hofmann, and J. M. Sanz. Preferential sputtering of oxides: A comparison of model predictions with experimental data. *Applied Surface Science*, 27(3):355–365, 1986.

[73] R. Behrisch (Ed.) P. Sigmund. *Sputtering by Particle Bombardment*. Springer, 1981.

[74] G. B. Arfken, H. J. Weber, and F. E. Harris. *Mathematical Methods for Physicists, Seventh Edition: A Comprehensive Guide*. Academic Press, 7th edition, 2012.

[75] M. L. Nietiadi and H. M. Urbassek. Influence of local curvature on sputtering. *Applied Physics Letters*, 103(11), 2013.

[76] H. M. Urbassek, R. M. Bradley, M. L. Nietiadi, and W. Möller. Sputter yield of curved surfaces. *Physical Review B*, 91(16):165418, 2015.

[77] D. H. Lehmer. Mathematical Methods in Large-scale Computing Units. *Proceedings of the Second Symposium on Large Scale Digital Computing Machinery*, pages 141–146, 1951.

[78] M. Matsumoto and T. Nishimura. Mersenne Twister: A 623-dimensionally Equidistributed Uniform Pseudo-random Number Generator. *ACM Transactions on Modeling and Computer Simulation*, 8(1):3–30, 1998.

[79] B. J. Alder and T. E. Wainwright. Studies in Molecular Dynamics. I. General Method. *The Journal of Chemical Physics*, 31(2):459–466, 1959.

[80] K. Nordlund. Molecular dynamics simulation of ion ranges in the 1–100 keV energy range. *Computational Materials Science*, 3(4):448 – 456, 1995.

[81] W. Möller and W. Eckstein. Tridyn – A TRIM simulation code including dynamic composition changes. *Nuclear Instruments and Methods in Physics Research Section B: Beam Interactions with Materials and Atoms*, 2(1):814 – 818, 1984.

[82] B.J. Alder and T.E. Wainwright. Phase transition for a hard sphere system. *The Journal of Chemical Physics*, 27(5):1208, 1957.

[83] J. M. Thijssen. *Computational Physics.* Cambridge University Press, 1999.

[84] C. Björkas and K. Nordlund. Comparative study of cascade damage in Fe simulated with recent potentials. *Nuclear Instruments and Methods in Physics Research Section B*, 259(2):853–860, 2007.

[85] K. Nordlund and S. L. Dudarev. Interatomic potentials for simulating radiation damage effects in metals. *Comptes Rendus Physique*, 9(3–4):343–352, 2008.

[86] K. Nordlund and F. Djurabekova. Multiscale modelling of irradiation in nanostructures. *Journal of Computational Electronics*, 13(1):122–141, 2014.

[87] M. S. Daw and M. I. Baskes. Embedded-atom method: Derivation and application to impurities, surfaces, and other defects in metals. *Physical Review B*, 29(12):6443–6453, 1984.

[88] D. L. Fedlheim and C. A. Foss. *Metal Nanoparticles: Synthesis, Characterization, and Applications.* CRC Press, 2001.

[89] R. J. Bandaranayake, G. W. Wen, J. Y. Lin, H. X. Jiang, and C. M. Sorensen. Structural phase behavior in II–VI semiconductor nanoparticles. *Applied Physics Letters*, 67(6):831–833, 1995.

[90] M. Moffitt, H. Vali, and A. Eisenberg. Spherical Assemblies of Semiconductor Nanoparticles in Water-Soluble Block Copolymer Aggregates. *Chemistry of Materials*, 10(4):1021–1028, 1998.

[91] R. S. Meltzer and K. S. Hong. Electron-phonon interactions in insulating nanoparticles: Eu_2O_3. *Physical Review B*, 61(5):3396–3403, 2000.

[92] R. Yan, D. Gargas, and P. Yang. Nanowire Photonics. *Nature Photonics*, 3(10):569–576, 2009.

[93] C. J. Murphy, T. K. Sau, A. M. Gole, C. J. Orendorff, J. Gao, L. Gou, S. E. Hunyadi, and T. Li. Anisotropic Metal Nanoparticles: Synthesis, Assembly, and Optical Applications. *The Journal of Physical Chemistry B*, 109(29):13857–13870, 2005.

[94] I. Matsui. Nanoparticles for Electronic Device Applications: A Brief Review. *Journal of Chemical Engineering of Japan*, 38(8):535–546, 2005.

[95] A. Vaseashta and D. Dimova-Malinovska. Nanostructured and nanoscale devices, sensors and detectors. *Science and Technology of Advanced Materials*, 6(3–4):312–318, 2005.

[96] A. B. Djurisic, A. M. C. Ng, and X. Y. Chen. ZnO nanostructures for optoelectronics: Material properties and device applications. *Progress in Quantum Electronics*, 34(4):191–259, 2010.

[97] X. Huang and M. A. El-Sayed. Gold nanoparticles: Optical properties and implementations in cancer diagnosis and photothermal therapy. *Journal of Advanced Research*, 1(1):13–28, 2010.

[98] P. Zijlstra and M. Orrit. Single metal nanoparticles: optical detection, spectroscopy and applications. *Reports on Progress in Physics*, 74(10):106401, 2011.

[99] Y. Tian and T. Tatsuma. Mechanisms and Applications of Plasmon-Induced Charge Separation at TiO2 Films Loaded with Gold Nanoparticles. *Journal of the American Chemical Society*, 127(20):7632–7637, 2005.

[100] I. H. El-Sayed, X. Huang, and M. A. El-Sayed. Surface Plasmon Resonance Scattering and Absorption of anti-EGFR Antibody Conjugated Gold Nanoparticles in Cancer Diagnostics: Applications in Oral Cancer. *Nano Letters*, 5(5):829–834, 2005.

[101] J.-H. Shim, S.-C. Lee, B.-J. Lee, J.-Y. Suh, and Y. Whan Cho. Molecular dynamics simulation of the crystallization of a liquid gold nanoparticle. *Journal of Crystal Growth*, 250(3–4):558–564, 2003.

[102] G. Grochola, S. P. Russo, and I. K. Snook. On morphologies of gold nanoparticles grown from molecular dynamics simulation. *The Journal of Chemical Physics*, 126(16):164707, 2007.

[103] M. Haruta and M. Daté. Advances in the catalysis of Au nanoparticles. *Applied Catalysis A*, 222(1textendash2):427–437, 2001.

[104] W. Rechberger, A. Hohenau, A. Leitner, J. R. Krenn, B. Lamprecht, and F. R. Aussenegg. Optical properties of two interacting gold nanoparticles. *Optics Communications*, 220(1–3):137–141, 2003.

[105] J. N. Anker, W. P. Hall, O. Lyandres, N. C. Shah, J. Zhao, and R. P. Van Duyne. Biosensing with plasmonic nanosensors. *Nature Materials*, 7(6):442–453, 2008.

[106] A. Klimmer, P. Ziemann, J. Biskupek, U. Kaiser, and M. Flesch. Size-dependent effect of ion bombardment on Au nanoparticles on top of various substrates: Thermodynamically dominated capillary forces versus sputtering. *Physical Review B*, 79(15):155427, 2009.

[107] J. Slocik, M. Stone, and R. Naik. Synthesis of Gold Nanoparticles Using Multifunctional Peptides. *Small*, 1(11):1048–1052, 2005.

[108] P. S. Chandran, R. Chaudhary, M.and Pasricha, A. Ahmad, and M. Sastry. Synthesis of Gold Nanotriangles and Silver Nanoparticles Using Aloevera Plant Extract. *Biotechnology Progress*, 22(2):577–583, 2006.

[109] J. Wagner and J. M. Köhler. Continuous Synthesis of Gold Nanoparticles in a Microreactor. *Nano Letters*, 5(4):685–691, 2005.

[110] R. S. Wagner and W. C. Ellis. Vaopr-liquid-solid mechanism of single crystal growth. *Applied Physics Letters*, 4(5):89–90, 1964.

[111] A. Räuber. Chemistry and Physics of Lithium Niobate. *Current Topics in Materials Science*, 1:481–601, 1978.

[112] T. Volk and M. Wöhlecke. *Lithium Niobate*, volume 115 of *Springer Series in Materials Science*. Springer Berlin Heidelberg, 2008.

[113] J. Melngailis. Focused ion beam technology and applications. *Journal of Vacuum Science & Technology B*, 5(2):469–495, 1987.

[114] L. A. Giannuzzi et al. *Introduction to focused ion beams: instrumentation, theory, techniques and practice.* Springer Science & Business Media, 2006.

[115] C. A Volkert, A. M Minor, et al. Focused ion beam microscopy and micromachining. *MRS Bulletin*, 32(5):389–399, 2007.

[116] S. Reyntjens and R. Puers. A review of focused ion beam applications in microsystem technology. *Journal of Micromechanics and Microengineering*, 11(4):287, 2001.

[117] M. Kawabe, M. Kubota, K. Masuda, and S. Namba. Microfabrication in $LiNbO_3$ by ion-bombardment-enhanced etching. *Journal of Vacuum Science & Technology*, 15(3):1096–1098, 1978.

[118] H. Hartung, E.-B. Kley, A. Tünnermann, T. Gischkat, F. Schrempel, and W. Wesch. Fabrication of ridge waveguides in zinc-substituted lithium niobate by means of ion-beam enhanced etching. *Optics Letters*, 33(20):2320–2322, 2008.

[119] T. Gischkat, H. Hartung, F. Schrempel, E.B. Kley, A. Tünnermann, and W. Wesch. Patterning of $LiNbO_3$ by means of ion irradiation using the electronic energy deposition and wet etching. *Microelectronic Engineering*, 86(4–6):910 – 912, 2009.

[120] H. Hartung, E.-B. Kley, T. Gischkat, F. Schrempel, W. Wesch, and A. Tünnermann. Ultra thin high index contrast photonic crystal slabs in lithium niobate. *Optical Materials*, 33(1):19 – 21, 2010.

[121] R. Geiss, S. Saravi, A.n Sergeyev, S. Diziain, F. Setzpfandt, F. Schrempel, R. Grange, E.-B. Kley, A. Tünnermann, and T. Pertsch. Fabrication of nanoscale lithium niobate waveguides for second-harmonic generation. *Optical Letters*, 40(12):2715–2718, 2015.

[122] Thomas Gischkat. *Ionenstrahlverstärktes Ätzen für die 3D-Strukturierung von Lithiumniobat.* PhD thesis, Friedrich-Schiller-Universität Jena, 2010.

[123] J. Reinisch, T. Schrempel, F.and Gischkat, and W. Wesch. Etching of ion irradiated $LiNbO_3$ in aqueous hydrofluoric solutions. *Journal of The Electrochemical Society*, 155(4):D298–D301, 2008.

[124] J. Goldstein, D.E. Newbury, D.C. Joy, C.E. Lyman, P. Echlin, E. Lifshin, L. Sawyer, and J.R. Michael. *Scanning Electron Microscopy and X-ray Microanalysis.* Springer, 2003.

[125] L. Reimer. *Image formation in low-voltage scanning electron microscopy*, volume 12. SPIE Press, 1993.

[126] B. Fultz and J. M. Howe. *Transmission electron microscopy and diffractometry of materials.* Springer Science & Business Media, 2012.

[127] L. Reimer. *Transmission electron microscopy: physics of image formation and microanalysis*, volume 36. Springer, 2013.

[128] L. Reimer. Scanning Electron Microscopy: Physics of Image Formation and Microanalysis, Second Edition. *Measurement Science and Technology*, 11(12):1826, 2000.

[129] D. Shindo and T. Oikawa. Energy Dispersive X-ray Spectroscopy. In *Analytical Electron Microscopy for Materials Science*, pages 81–102. Springer, 2002.

[130] E. Meyer. Atomic force microscopy. *Progress in Surface Science*, 41(1):3 – 49, 1992.

[131] R. W. Bowen and N. Hilal. *Atomic force microscopy in process engineering: an introduction to AFM for improved processes and products.* Butterworth-Heinemann, 2009.

[132] K. Gärtner. Modified master equation approach of axial dechanneling in perfect compound crystals. *Nuclear Instruments and Methods in Physics Research Section B: Beam Interactions with Materials and Atoms*, 227(4):522 – 530, 2005.

[133] G. Schatz, A. Weidinger, and M. Deicher. *Nukleare Festkörperphysik: kernphysikalische Messmethoden und ihre Anwendungen.* Springer, 2010.

[134] C. A. Schneider, W. S. Rasband, and K. W. Eliceiri. NIH Image to ImageJ: 25 years of image analysis. *Nature Methods*, 9:617–675, 2012.

[135] F. Schiettekatte. Fast Monte Carlo for ion beam analysis simulations. *Nuclear Instruments and Methods in Physics Research Section B: Beam Interactions with Materials and Atoms*, 266(8):1880–1885, 2008.

[136] C. Borschel. *iradina manual*, 2014. Available at `www.iradina.de` (accessed 19.07.2016).

[137] H. Holland-Moritz, S. Scheeler, C. Stanglmair, C. Pacholski, and C.n Ronning. Enhanced sputter yields of ion irradiated Au nano particles: energy and size dependence. *Nanotechnology*, 26(32):325301, 2015.

[138] W. K. Chu. Calculation of energy straggling for protons and helium ions. *Physical Review A*, 13:2057–2060, 1976.

[139] S. M. Foiles, M. I. Baskes, and M. S. Daw. Embedded-atom-method functions for the fcc metals Cu, Ag, Au, Ni, Pd, Pt, and their alloys. *Physical Review B*, 33:7983–7991, 1986.

[140] M. L. Nietiadi, L. Sandoval, H. M. Urbassek, and W. Möller. Sputtering of Si nanospheres. *Physical Review B*, 90:045417, 2014.

[141] K. Nordlund, J. Tarus, J. Keinonen, S.E. Donnelly, and R.C. Birtcher. Atomic fingers, bridges and slingshots: formation of exotic surface structures during ion irradiation of heavy metals. *Nuclear Instruments and Methods in Physics Research Section B: Beam Interactions with Materials and Atoms*, 206:189 – 193, 2003.

[142] A. V. Krasheninnikov and K. Nordlund. Ion and electron irradiation-induced effects in nanostructured materials. *Journal of Applied Physics*, 107(7), 2010.

[143] X. Hu, D. G. Cahill, and R. S. Averback. Burrowing of Pt nanoparticles into SiO_2 during ion-beam irradiation. *Journal of Applied Physics*, 92(7):3995–4000, 2002.

[144] J.W. Mayer, B.Y. Tsaur, S.S. Lau, and L-S. Hung. Ion-beam-induced reactions in metal-semiconductor and metal-metal thin film structures. *Nuclear Instruments and Methods*, 182–183, Part 1:1 – 13, 1981.

[145] T.M. Nenadovic, Z.B. Fotiric, and T.S. Dimitrijevic. Sputtering of gold bombarded by 20–50 keV Ar^+ and Xe^+ ions. *Surface Science*, 33(3):607 – 616, 1972.

[146] A. Oliva-Florio, R. A. Baragiola, M. M. Jakas, E. V. Alonso, and J. Ferrón. Noble-gas ion sputtering yield of gold and copper: Dependence on the energy and angle of incidence of the projectiles. *Physical Review B*, 35:2198–2204, 1987.

[147] H. Hofsäss and K. Zhang. Surfactant sputtering. *Applied Physics A*, 92(3):517–524, 2008.

[148] H. Hofsäss and K. Zhang. Fundamentals of surfactant sputtering. *Nuclear Instruments and Methods in Physics Research Section B: Beam Interactions with Materials and Atoms*, 267(16):2731 – 2734, 2009.

[149] H. Holland-Moritz, A. Ilinov, F. Djurabekova, K. Nordlund, and C. Ronning. Sputtering and redeposition of ion irradiated Au nanoparticle arrays: direct comparison of simulations to experiments. *New Journal of Physics* (submitted), 2016.

[150] H. Hartung. *Mikro- und Nanostrukturierung von Lithiumniobat.* PhD thesis, Friedrich-Schiller-Universität Jena, 2010.

[151] F. Lu, F. X. Wang, W. Li, J. H. Zhang, and K. M. Wang. Annealing behavior of barriers in ion-implanted $LiNbO_3$ and $LiTaO_3$ planar waveguides. *Applied Optics*, 38(24):5122–5126, 1999.

[152] S. Wolf, J. Rensberg, H. Stöcker, B. Abendroth, W. Wesch, and C. Ronning. Utilizing dynamic annealing during ion implantation: synthesis of silver nanoparticles in crystalline lithium niobate. *Nanotechnology*, 25(13):135611, 2014.

[153] I. Szafraniak, I. Radu, R. Scholz, M. Alexe, and U. Gösele. Single-Crystalline Ferroelectric Thin Films by Ion Implantation and Direct Wafer Bonding. *Integrated Ferroelectrics*, 55(1):983–990, 2003.

[154] R. M. Roth, D. Djukic, Y. Seung Lee, R. M. Osgood, S. Bakhru, B. Laulicht, K. Dunn, H. Bakhru, L. Wu, and M. Huang. Compositional and structural changes in $LiNbO_3$ following deep He^+ ion implantation for film exfoliation. *Applied Physics Letters*, 89(11), 2006.

[155] T. Gischkat, F. Schrempel, T. Höche, and W. Wesch. Annealing behavior of lithium niobate irradiated with He-ions at 100 K. *Nuclear Instruments and Methods in Physics Research Section B: Beam Interactions with Materials and Atoms*, 267(8–9):1492 – 1495, 2009.

A Monte Carlo redeposition algorithm

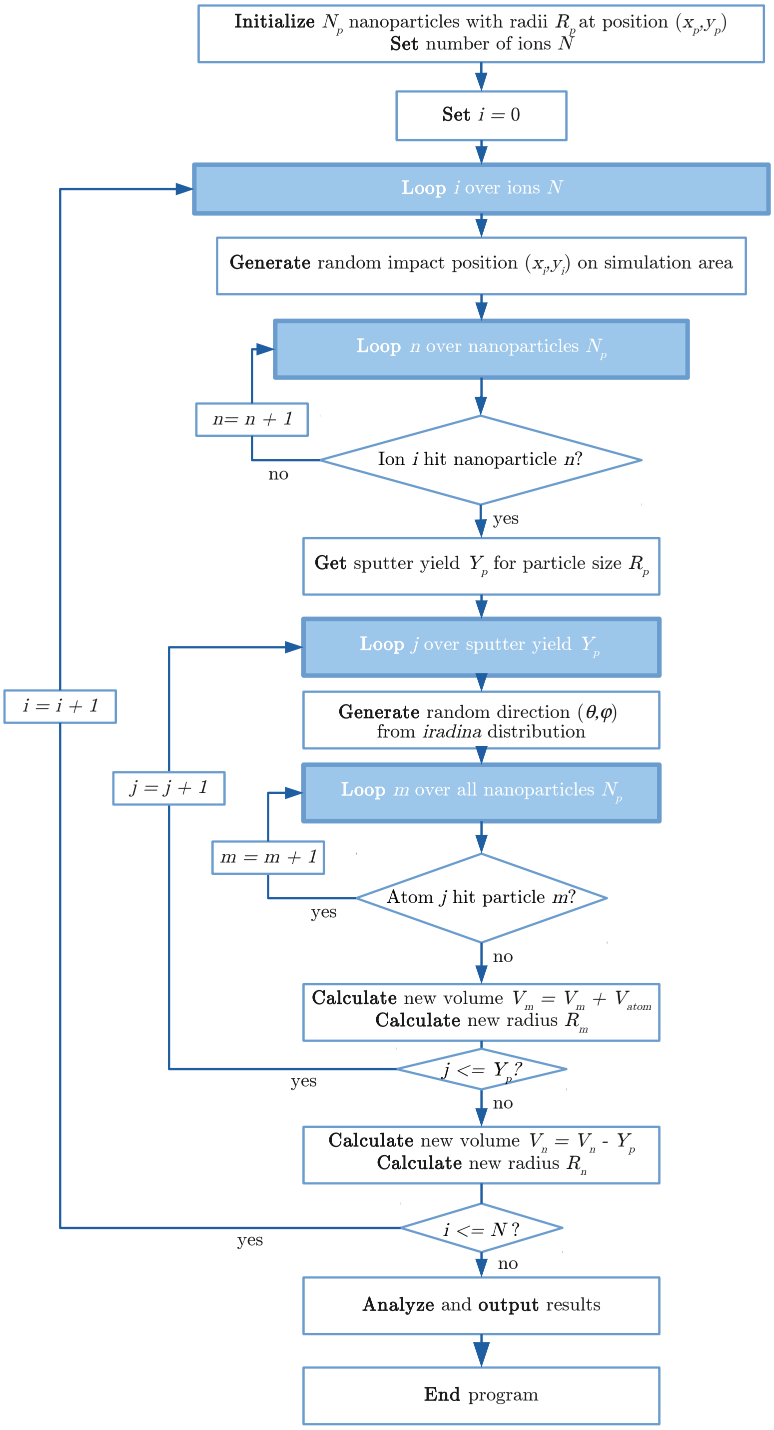

List of Publications

1. A. Johannes, **H. Holland-Moritz**, C.Ronning. *Ion beam irradiation of nanostructures: sputtering, dopant incorporation, and dynamic annealing*, Semiconductor Science and Technology. 30 (3):033001, 2015
2. **H. Holland-Moritz**, S. Scheeler, C. Stanglmair, C. Pacholski, C.Ronning. *Enhanced sputter yields of ion irradiated Au nano particles: energy and size dependence*, Nanotechnology. 26: 325301, 2015
3. **H.Holland-Moritz**, A. Ilinov, F. Djurabekova, K. Nordlund, C.Ronning. *Sputtering and redeposition of ion irradiated Au nanoparticle arrays: direct comparison of simulations to experiments*, New Journal of Physics (submitted)

List of oral and poster presentations

1. Talk: *Sputtering effects on ion irradiated Au nanoparticles*
   DPG Spring Meeting, Regensburg 2013
2. Talk: *Sputtering effects on ion irradiated Au nanoparticles*
   Workshop – Ionenstrahlen & Nanostrukturen, Leipzig 2013
3. Talk: *Enhanced sputtering effects on ion irradiated Au nanoparticles*
   SMMIB Meeting, Kusadasi 2013
4. Poster: *Enhanced Sputtering Effects on Ion Irradiated Au Nanoparticles*
   Workshop – TRNM, Levi 2014
5. Poster: *Enhanced Sputtering effects on ion irradiated Au nanoparticles*
   Workshop – Ionenstrahlen & Nanostrukturen, Paderborn 2014
6. Poster: *Simulation of Sputtering of Au Nanoparticles*
   IBMM Meeting, Leuven 2014
7. Poster: *Geometrical Sputtering Effects of Nanoparticles*
   Workshop – TRNM, Levi 2015
8. Poster: *In-Situ Study of Sputtering of Au Nanoparticles*
   MRS Fall Meeting, Boston 2015

B | Curriculum Vitae

Persönliche Daten

Name	Henry Holland-Moritz
Geburtsdatum	30.03.1985
Geburtsort	Suhl

Ausbildung und wissenschaftlicher Werdegang

1991 - 1995	Grundschule Benshausen
1995 - 2003	Heinrich-Ehrhardt Gymnasium Zella-Mehlis
Juni 2003	Abitur
2003 - 2004	Zivildienst im Kinder- und Jugendheim Benshausen e.V.
2004 - 2006	Studium Maschinenbau an der Fachhochschule Schmalkalden – Vordiplom
2006 - 2011	Studium Lehrmant an Gymnasien Physik–Mathematik an der Friedrich-Schiller-Universität Jena
Okt. 2011	1. Staatsexamen für das Lehramt an Gymnasien
2012 - 2016	Wissenschaftlicher Mitarbeiter an der Friedrich-Schiller-Universität Jena, AG Ronning

Beruflicher Werdegang

Seit April 2016	Lehrer für besondere Aufgaben für Physik an der Ernst-Abbe-Hochschule Jena

Jena, den 21.07.2016

(Henry Holland-Moritz)

Ehrenwörtliche Erklärung

Ich erkläre hiermit ehrenwörtlich, dass ich die vorliegende Arbeit selbstständig, ohne unzulässige Hilfe Dritter und ohne Benutzung anderer als der angegebenen Hilfsmittel und Literatur angefertigt habe. Die aus anderen Quellen direkt oder indirekt übernommenen Daten und Konzepte sind unter Angabe der Quelle gekennzeichnet.
Bei der Auswahl und Auswertung des gezeigten Materials haben mir die nachstehend aufgeführten Personen in der jeweils beschriebenen Weise entgeltlich/unentgeltlich geholfen:

1. Sämtliche Proben mit regulär angeordneten Gold-Nanopartikeln wurden von Sebastian Scheeler, Christoph Stanglmair und Claudia Pacholski nach dem in Kapitel 3.2.2 beschriebenen Verfahren hergestellt. Des weiteren wurden die $LiNbO_3$-Proben mit Au Nanopartikeln von ebendieser Gruppe hergestellt.

2. Das Sputter-Modell für definierte Ioneneinschlagspunkte, dargestellt in Kapitel 4.2, wurde in Zusammenarbeit mit Emanuel Schmidt erdacht.

3. Die *iradina*-Simulationen in Kapitel 4 wurden in Zusammenarbeit mit Andreas Johannes, Christian Borschel und Emanuel Schmidt durchgeführt und diskutiert.

4. Sämtliche MD Simulationen wurden in Zusammenarbeit mit Andrey Ilinov, Flyura Djurabekova und Kai Nordlund konzipiert und am Alcyone-Cluster in Helsinki durchgeführt.

5. Die *in situ* Experimente, welche in Kapitel 5.2 dargelegt wurden, wurden in Zusammenarbeit mit Julia Graupner im Rahmen ihrer Seminarfacharbeit durchgeführt.

6. Die RBS-Messungen, dargestellt in Kapitel 5.3, wurden in Zusammenarbeit mit Jura Rensberg durchgeführt und deren Ergebnisse mit ihm interpretiert.

7. Die TEM-Lamellenpräparationen der Gold-Nanopartikelproben, präsentiert in Kapitel 5.3, und der $LiNbO_3$-Proben, präsentiert in Kapitel 7.2, wurden von Carmen Voigt und Philipp Schöppe durchgeführt.

8. Der MC-Algorithmus zur Simulation von Redeposition von zerstäubten Atomen, präsentiert in Kapitel 6, wurde in Zusammenarbeit mit Andrey Ilinov, Flyura Djurabekova und Kai Nordlund entwickelt.

9. Die Experimente zur Strukturierung von $LiNbO_3$ wurden in Zusammenarbeit Sven Bauer im Rahmen seiner Masterarbeit durchgeführt.

10. Die Bestrahlungsexperimente an den Beschleunigern ROMEO und JULIA wurden mit Hilfe von Patrick Hofmann und Ulrich Barth durchgeführt.

11. Die jeweiligen Koautoren der in Anhang A aufgeführten Publikationen waren an der Erarbeitung und Interpretation der Ergebnisse und deren Darstellung beteiligt.

Weitere Personen waren an der inhaltlich–materiellen Erstellung der vorliegenden Arbeit nicht beteiligt. Insbesondere habe ich hierfür nicht die entgeltliche Hilfe von Vermittlungs- bzw. Beratungsdiensten (Promotionsberater und andere Personen) in Anspruch genommen. Niemand hat von mir unmittelbar oder mittelbar geldwerte Leistungen für Arbeiten erhalten, die im Zusammenhang mit dem Inhalt der vorgelegten Dissertation stehen.

Die Arbeit wurde bisher weder im In- noch im Ausland in gleicher oder ähnlicher Form einer anderen Prüfungsbehörde vorgelegt.

Die geltende Prüfungsordnung der Physikalisch-Astronomischen Fakultä ist mir bekannt.

Ich versichere ehrenwörtlich, dass ich nach bestem Wissen die reine Wahrheit gesagt und nichts verschwiegen habe.

Jena, den 21.07.2016 Henry Holland-Moritz

Danksagung

Eine Dissertation schreibt sich nicht von allein und auch die Arbeit, welche in diese Dissertation eingeflossen ist, wurde nicht allein bewältigt. Über die mehr als vier Jahre hinweg, in denen ich als Doktorand im Roten Haus gearbeitet habe, haben mich sehr viele Menschen unterstützt und begleitet, und diesen Menschen möchte ich an dieser Stelle danken.

Allen voran gilt natürlich Carsten Ronnig ein riesiges Dankeschön! Carsten, ich bin 2011 für meine Examensarbeit in deine Arbeitsgruppe gekommen und ich habe mich sofort wohl gefühlt. Du hattest von Anfang an ein offenes Ohr und deine Tür stand immer offen. Das hat sich über die Jahre nicht geändert und ich habe dich als Doktorvater sowohl als wissenschaftlicher Betreuer als auch als Mensch sehr zu schätzen gelernt. Ich konnte jederzeit zu dir kommen, wenn es ein fachliches Problem (Verzeihung, eine fachliche Herausforderung) gab, konnte dir meine Ideen vorstellen und sie offen diskutieren. Und du hast dir immer Zeit genommen, dich geduldig durch all meine nicht immer einfach zu lesenden englischen Texte zu arbeiten. Darüber hinaus danke ich dir für die vielen schönen Dienstreisen, die du mir ermöglicht hast. Ich weiss, dass so viele Konferenzbesuche und wochenlange Aufenthalte in Finnland keine Selbstverständlichkeit sind. Ebenfalls keine Selbstverständlichkeit ist, dass du mir auch ausserhalb der Physik immer wieder mit Rat und Tat zur Seite standest und dir Zeit genommen hast, dir das ewige hin- und her der Entscheidung, ob ich nun Dozent werde oder nicht, anzuhören. Abseits all der "ernsten" Dinge des Doktorandenalltags konnte man mit dir auch auf zahllosen Physikerbällen, Weihnachtsfeiern, Postersessions und Semesterabschlussfeiern ordentlich feiern (MRS). Ich habe viel von dir gelernt - über Physik und darüber hinaus. Tausend Dank für alles, Carsten!

Neben Carsten haben meinen wissenschaftlichen Werdegang am IFK vor allem Raphael und Christian beeinflusst. Raphael, du hast mich auf den wissenschaftlichen Weg gebracht. Von dir habe ich nicht nur die Aufgabe der Planung des Group Meetings übernommen (Spam is coming), sondern auch deine Art Dinge anzugehen. Christian, du hast mich nach der Examensarbeit "übernommen" und mir das neue Themengebiet der Ionenstrahlphysik und des Sputterns gezeigt. Danke für deine unendliche Geduld, wenn es um *iradina* und Linux Shell ging. Und Danke euch beiden für den unvergesslichen Besuch beim Scooter-Konzert!

Weiterhin möchte ich all den Menschen danken, mit denen ich außerhalb des IFK zusammengearbeitet habe. Da wären zum einen die Gruppe um Claudia Pacholski am MPI. Danke Sebastian, Christoph und Claudia für all die Proben und die Erfüllung der Sonderwünsche bei der Produktion dieser. Und Danke für die freundschaftliche Atmosphäre während unserer Zusammenarbeit. A lot of graditude goes to Helsinki to the groups at Acclab, especially Andrey, Flyura and Kai. Thank you so much for the opportunity to visit your lab and to work with you! Andrey, thanks a lot for your patience and your teaching of the basics of MD and MC. You were always there when Alcyone woun't run my scripts and the scripts did not do what they were supposed to. Thank you Flyura and Kai for your kind invitation and the fruitful discussions in your lab. I had a great time in Helsinki and Levi and I really enjoyed working with you. I also brought your Happy Friday to Germany. Thanks a lot for everything!

Die Zeit während der Promotion wäre aber nicht halb so schön gewesen ohne die anderen Kollegen im Roten Haus. Alle dort haben dafür gesorgt, dass ich jeden Tag gern auf Arbeit gekommen bin. Jeder war zu jeder Zeit hilfsbereit, die Atmosphäre war stets entspannt und die Frühstücksrunden waren stets lustig (wenn ich denn rechtzeitig da war). Ein besonderer Dank geht an das Team im Sekretariat:

Anja, Marie und Cindy waren immer zur Stelle, wenn die Reisekostenabrechnung zu kompliziert war, ein Antrag eingereicht werden musste und die Formalien des Uni-Alltags einen mal wieder überfordert haben. Dafür ein großes Danke! Ein ebenso großes Danke geht an die Techniker im Beschleunigerlabor. Patrick hat den ROMEO im Griff und hat immer alles und ein bisschen mehr gegeben, um auch die kleinste und größte Energie aus der Maschine zu locken. Kein Element war zu schwierig, keine Quelle zu instabil, keine Strahlzeit zu lang. Vielen Dank für deine Hilfe, Patrick! Auch Ulli gebührt ein großer Dank für die Hilfe bei den RBS Messungen. Auch er hat alles aus JULIA herausgeholt und stand stets mit hilfreichen Tipps zur Seite. Carmen gebührt ebenfalls ein großes Dankeschön für die Hilfe am FIB, die Präparation der Lamellen und die Connections zur Glaschemie. Ohne sie hätten wir unser $LiNbO_3$ im Detail nie zu Gesicht bekommen. Danke! Auch alle anderen Mitarbeiter, Diplomanden, Masteranden, Doktoranden und Praktikanten haben mir stets geholfen, wenn sie konnten und haben auch neben der Arbeit immer Zeit für ein Pläuschchen gehabt - oder Stickstoffeis, Grillen oder das Wirtshaus. Im diesem Sinne danke ich Frank, Udo, Claudia, Martin G., Davide, Heiß-Heißer-Heisler, Steffen, Stefanie, Philipp (du bist ne 9!), Jana, Sebastian, Alex, Max und Marcel. Meinen Masterstudenten Stefan und Sven gilt besonderer Dank: Stefan, Danke für die Messungen, auch wenn sie leider nicht den Weg in diese Arbeit gefunden haben. Und Danke Sven, der du in einem Kapitel hier verewigt bist. Danke für die Diskussion über Comics neben heißer Flusssäure in voller Schutzbekleidung. Ein großer Dank geht an Julia, die als Schülerin ans IFK kam und eine Seminarfacharbeite suchte. Du hast das alles super gemacht und sogar beim Bundeswettbewerb bei Jugend Forscht abgeräumt. Super, ich bin sehr stolz auf dich! Jura gilt besonderer Dank für die Hilfe bei den RBS-Experimenten. Danke für die lustigen Nachtschichten! Außerdem vielen Dank an Emanuel für die Hilfe beim Fitten von Schadensverteilungen und dem scharfen Blick für Gauss-Verteilungen.

Nun sei dem berühmt-berüchtigte Büro 203 besonders gedankt, dem Londen Gentlemen's Club des IFK, da ich die meiste Zeit meiner Promotion dort verbracht habe. Das Klima war immer hart, trotzdem besonders unfair, aber herzlich (frei nach dem Motto: 10 von 10 Büroangestellten finden Mobbing vollkommen in Ordnung). Es war aber vor allem eins: Immer lustig. Neben dem ganzen Unsinn, der dort verzapft wurde, gab es auch Lichtblicke wissenschaftlicher Diskussion und Debatten, die nicht selten sehr emotional geführt wurden. Wären da nicht Robert, Andreas und Yaser, sowie die Ehrenmitglieder Alex und Emanuel, gewesen, dann wäre diese Dissertation sicher etwas schneller entstanden. Da zu einer wissenschaftlichen Ausbildung heutzutage aber auch sog. Softskills gehören, danke ich 203 ganz besonders für diese Art der Weiterbildung. Wenn ich während meiner Zeit im Büro eins gelernt habe: Sperre immer deinen Monitor, wenn du den Raum verlässt und versuche die Zeit außerhalb des Büros möglichst kurz zu halten. Ich werde euch vermissen, 203. Einer Person danke ich an dieser Stelle jedoch noch einmal besonders: Robert. Danke für die schöne Zeit und sorry, dass ich so früh gehen musste. Aber wie du schon einmal gesagt hast: Unglaublich, dass wir beide in einem Büro gelandet sind. Die zwei Alten aus der Muppetshow.

Ohne Freunde, die einen aufmuntern, wenn es einmal nicht so gut läuft, die einen aufnehmen, wenn es gerade wirklich nicht gut läuft oder die einem einfach die Freizeit versüßen wäre die Dissertation sicher auch nicht fertig geworden. Deshalb ein ganz großes Cheers und Danke an Sören, Claudi, Marv, Christin, Robert, Tobi, Schma, Heller und Vincent. All these nights in bars somehow saved my soul.

Fürs Korrekturlesen bin ich Dr. John zu herzlichstem Dank verpflichtet. Er hat sich trotz heftiger Physik-Aversion durch den Großteil dieser Arbeit gekämpft und so manchen grammatikalischen Fauxpas verhindert. Danke dafür! Weiterhin danke ich meinen Korrekturlesern Andreas, Claudia, Robert, Jura und Emanuel für das Lesen der einzelnen Kapitel! Auch meinen neuen Kollegen an der EAH gilt großer Dank, da sie mir im ersten Semester dort viel Arbeit abgenommen haben, damit ich diese Arbeit fertig stellen konnte. Auch haben sie eine tolle Arbeitsatmosphäre geschaffen, in der ich mich gleich wieder

wohl gefühlt habe. Also, Danke Karsten, Stefan und Wolfram! Dass ich überhaupt den Schritt gewagt und Physik studiert habe, verdanke ich Klaus Wagner. Danke für die vielen interessanten Gespräche über Physik, als wir eigentlich Mathe lernen sollten!

Zum Schluss geht der wohl größte Dank an meine Familie. Liebe Mamó, lieber Paps, Brudi, Oma Renate und Opa Burki, Oma Ellen und Opa Herbert, tausend Dank für alles, was ihr bisher alles für mich gemacht habt und mit Sicherheit weiter für mich tun werdet. Danke für die jahrelange Unterstützung und Geduld während meiner scheinbar niemals enden wollenden Ausbildung. Aber nun ist es geschafft! Liebste Jenny, danke für die aufmunternden Essenspakete mit leckerem Gebäck, die mir immer wieder Kraft gegeben haben, wenn ich mal durchhing. Danke für die aufmunternden Worte, als das Zusammenschreiben mal wieder schwer war. Und Danke für all die entgegengebrachte Liebe.